TURUN
YLIOPISTO
UNIVERSITY
OF TURKU

MRI FINDINGS AFTER TRANSURETHRAL ULTRASOUND ABLATION OF PROSTATE

Pietari Mäkelä

TURUN YLIOPISTON JULKAISUJA – ANNALES UNIVERSITATIS TURKUENSIS
SARJA – SER. D OSA – TOM. 1814 | MEDICA – ODONTOLOGICA | TURKU 2024

TURUN
YLIOPISTO
UNIVERSITY
OF TURKU

MRI FINDINGS AFTER TRANSURETHRAL ULTRASOUND ABLATION OF PROSTATE

Pietari Mäkelä

TURUN YLIOPISTON JULKAISUJA – ANNALES UNIVERSITATIS TURKUENSIS
SARJA – SER. D OSA – TOM. 1814 | MEDICA – ODONTOLOGICA | TURKU 2024

University of Turku

Faculty of Medicine
Radiology
Doctoral Programme in Clinical Research
Department of Radiology, Turku University Hospital

Supervised by

Professor Roberto Blanco Sequeiros
Department of Diagnostic Radiology
Turku University Hospital
Turku, Finland

Associate Professor Peter J. Boström
Department of Urology
Turku University Hospital
Turku, Finland

Reviewed by

Associate Professor Harri Visapää
Comprehensive Cancer Center
HUS Helsinki University Hospital
Helsinki, Finland

Associate Professor Niko Sillanpää
Vascular Center
Tampere University Hospital
Tampere, Finland

Opponent

Professor Jurgen Fütterer
Department of Imaging
Radbound University Medical Center
Nijmegen, the Netherlands

ISBN 978-951-29-9861-6 (PRINT)
ISBN 978-951-29-9862-3 (PDF)
ISSN 0355-9483 (Print)
ISSN 2343-3213 (Online)
Painosalama, Turku, Finland 2024

It’s nice to be important, but it’s more important to be nice.

H.P. Baxxter *(in a Scooter song)*

UNIVERSITY OF TURKU
Faculty of Medicine
Department of Clinical Medicine
Radiology
PIETARI MÄKELÄ: MRI findings after transurethral ultrasound ablation of prostate
Doctoral Dissertation, 131 pp.
Doctoral Programme in Clinical Research
September 2024

ABSTRACT

Prostatectomy and radiation therapy have been the cornerstone of the treatment of prostate cancer (PCa) for several decades. While being effective treatment methods, the downside is the burden of substantial adverse effects.

Evolution of magnetic resonance imaging (MRI) of prostate has improved the PCa detection, localization and characterization, paving the way for less invasive ablative treatments. MRI-guided transurethral ultrasound ablation (TULSA) is a novel method in the field of prostate ablation. With TULSA, prostatic tissue is destroyed by thermal energy generated by high-intensity ultrasound. TULSA can be used for the treatment of both malignant (primary, salvage or palliative) and benign (hyperplasia) prostate conditions.

The purpose of this doctoral research was to investigate acute and subacute MRI findings related to TULSA treatment, and the evolution of post-treatment necrotic tissue up to one year. The results showed that the extent of tissue necrosis, measured by contrast-enhanced MRI as non-perfused volume (NPV), enlarged within the first few weeks after the procedure. With longer follow-up NPV gradually decreased, and after one year most of the necrotic tissue had disappered. The resolution of necrotic tissue after ablation was markedly slower for irradiated than treatment-naïve prostate tissue.

Fiducial markers implanted in prostate are widely used in the radiation therapy. Safety and efficacy of ultrasound ablation for radiorecurrent PCa in the presence of gold fiducial markers had not been previously studied. There was a reasonable doubt, that intraprostatic fiducial markers could hinder ablation-based salvage treatments by mechanically obstructing the ablative energy, and by causing MRI artifacts. Our results showed that patients with intraprostatic gold fiducial markers can successfully be treated with TULSA.

Overall, this work offers knowlegde on clinical routine, assessment of post-TULSA condition, and optimization of follow-up protocols.

KEYWORDS: prostate cancer, magnetic resonance imaging, thermal ablation, MRI-guided transurethral ultrasound ablation (TULSA), fiducial marker, non-perfused volume (NPV)

TURUN YLIOPISTO
Lääketieteellinen tiedekunta
Kliininen laitos
Radiologia
PIETARI MÄKELÄ: Eturauhasen transuretraalisen ultraääniablaation jälkeiset MRI-löydökset
Väitöskirja, 131 s.
Turun kliininen tohtoriohjelma
Syyskuu 2024

TIIVISTELMÄ

Leikkaus ja sädehoito ovat olleet eturauhassyövän hoidon kulmakiviä useiden vuosikymmenten ajan. Vaikka nämä hoitomenetelmät ovatkin tehokkaita, liittyy niihin merkittäviä haittavaikutuksia.

Eturauhasen magneettikuvauksen kehitys on parantanut eturauhassyövän havaitsemista, paikantamista ja luokittelua. Tämä on mahdollistanut vähemmän invasiivisten ablaatiohoitojen käyttöönoton. MRI-ohjattu transuretraalinen ultraääniablaatio (TULSA) on uusi menetelmä eturauhasen ablaatiohoitojen joukossa. TULSA-hoidossa eturauhaskudos tuhotaan korkeaintensiteettisen ultraäänen tuottamalla lämpöenergialla. Menetelmää voidaan käyttää sekä pahanlaatuisten (primaari, sädehoidon jälkeinen paikallisuusiutuma tai palliatiivinen) että hyvänlaatuisten (liikakasvu) eturauhassairauksien hoitoon.

Tämän väitöskirjatyön tarkoituksena oli tutkia TULSA-hoitoon liittyviä akuutteja ja subakuutteja MRI-löydöksiä sekä hoidon jälkeisen nekroottisen kudoksen muutosta vuoden seurannassa. Tulokset osoittivat, että varjoainetehosteisella MRI:llä mitattu kudosnekroosialue (NPV), kasvoi muutaman ensimmäisen viikon aikana toimenpiteen jälkeen. Pidemmässä seurannassa NPV pieneni vähitellen, ja vuoden kuluttua suurin osa nekroottisesta kudoksesta oli hävinnyt. Nekroottisen kudoksen häviäminen TULSA-hoidon jälkeen todettiin huomattavasti hitaammaksi aiemmin sädehoidetussa eturauhaskudoksessa.

Sädehoidon suunnittelussa käytetään eturauhaseen implantoitavia merkkijyviä. Ultraääniablaation turvallisuutta ja tehoa paikallisesti uusiutuneessa eturauhassyövässä merkkijyvä-potilailla ei ollut aiemmin tutkittu. Oli perusteltua epäillä, että merkkijyvät voisivat haitata ablaatiota estämällä mekaanisesti ultraäänienergian etenemistä, ja aiheuttamalla MRI-artefaktoja. Tuloksemme osoittivat, että merkkijyvä-potilaita voidaan hoitaa onnistuneesti TULSA:lla.

Yhteenvetona, tämä työ tarjoaa lisätietoa kliiniseen hoitotilanteeseen, TULSA:n jälkeisen tilan arviointiin ja seurantaprotokollien optimointiin.

AVAINSANAT: eturauhassyöpä, magneettikuvantaminen, termoablaatio, MRI-ohjattu transuretraalinen ultraääniablaatio (TULSA), merkkijyvä, perfusoitumaton alue (NPV)

Table of Contents

Abbreviations

ACR	American college of radiology
ADC	Apparent diffusion coefficient
ADT	Androgen deprivation therapy
AE	Adverse event
AFS	Anterior fibromuscular stroma
AS	Active surveillance
BCR	Biochemical recurrence
BPH	Benign prostatic hyperplasia
bpMRI	Biparametric magnetic resonance imaging
BS	Bone scan
CEM43	Cumulative equivalent minutes at 43 ℃
csPCa	Clinically significant prostate cancer
CT	Computed tomography
CZ	Central zone
DCE	Dynamic contrast-enhanced
DRE	Digital rectal examination
DWI	Diffusion-weighted imaging
EANM	The European association of nuclear medicine
EAU	European association of urology
EBRT	External beam radiation therapy
ECD	Endorectal cooling device
EPE	Extraprostatic extension
EPI	Echo planar imaging
EPIC	The expanded prostate cancer index composite
ESUR	European society of urogenital radiology
FLA	Focal laser ablation
FT	Focal therapy
GBCA	Gadolinium-based contrast agent
GG	Grade group
GI	Gastrointestinal
GRE	Gradient echo

GS	Gleason score
GU	Genitourinary
HIFU	High-intensity focused ultrasound
HoLEP	Holmium laser enucleation
IDC-P	Intraductal carcinoma of prostate
IIEF-5	International index of erectile function
IPSS	International prostate symptom score
IRE	Irreversible electroporation
ISUP	The international society of urological pathology
LUTS	Lower urinary tract symptoms
mpMRI	Multiparametric magnetic resonance imaging
MRI	Magnetic resonance imaging
NECP	Neuroendocrine carcinoma of prostate
NPV	Non-perfused volume
NVB	Neurovascular bundle
PCa	Prostate cancer
PD	Proton density
PDT	Photodynamic therapy
PET	Positron emission tomography
PI-FAB	Prostate imaging after focal ablation
PI-RADS	Prostate imaging-reporting and data system
PRFS	Proton resonance frequency shift
PI-RR	Prostate magnetic resonance imaging for local recurrence reporting
PS	Positioning system
PSA	Prostate-specific antigen
PSMA	Prostate-specific membrane antigen
PZ	Peripheral zone
QoL	Quality of life
RALP	Robotic-assisted laparoscopic prostatectomy
RCT	Randomized controlled trial
RF	Radiofrequency
RFA	Radiofrequency ablation
RFS	Recurrence-free survival
ROI	Region of interest
RP	Radical prostatectomy
RT	Radiation therapy
SE	Spin echo
SI	Signal intensity
SIR	Signal intensity ratio
sTULSA	Salvage transurethral ultrasound ablation of prostate

SUVmax	Maximum standard uptake value
T1W	T1-weighted
T2W	T2-weighted
TE	Time of echo
TNM	Tumor, node and metastasis
TR	Repetition time
TRUS	Transrectal ultrasound
TUIP	Transurethral incision of the prostate
TULSA	Transurethral ultrasound ablation of prostate
TURP	Transurethral resection of the prostate
TZ	Transition zone
UA	Ultrasound applicator
UTI	Urinary tract infection

List of Original Publications

This dissertation is based on the following three original publications, which are referred to in the text by their Roman numerals:

I Pietari Mäkelä, Mikael Anttinen, Visa Suomi, Aida Steiner, Jani Saunavaara, Teija Sainio, Antero Horte, Pekka Taimen, Peter J. Boström, Roberto Blanco Sequeiros. Acute and subacute prostate MRI findings after MRI-guided transurethral ultrasound ablation of prostate cancer. *Acta Radiologica*, 2021; 62: 1687–1695.

II Pietari Mäkelä, Cameron Wright, Mikael Anttinen, Peter J. Boström, Roberto Blanco Sequeiros. Safety and efficacy of MRI-guided transurethral ultrasound ablation for radiorecurrent prostate cancer in the presence of gold fiducial markers. *Acta Radiologica*, 2023; 64: 1228–1237.

III Pietari Mäkelä, Mikael Anttinen, Cameron Wright, Teija Sainio, Peter J. Boström, Roberto Blanco Sequeiros. Evolution of non-perfused volume after transurethral ultrasound ablation of prostate: A retrospective 12-month analysis. *European Journal of Radiology Open*, 2023; 11: 100506.

1 Introduction

Prostate cancer (PCa) stands as the second most common cancer and the fifth leading cause of cancer death among men worldwide. Despite its significant mortality rates, many men with diagnosed PCa have favourable prognosis and will not experience any clinically significant consequences of this disease during their lifetime.

PCa diagnosis typically involves clinical examination, prostate-specific antigen (PSA) testing, and ultrasound-guided biopsy. While there is ongoing debate regarding PSA screening, its use has grown among asymptomatic men.

Traditionally, the possible spread of the disease has been assessed using computed tomography (CT) and bone scan (BS), but these methods often lack the sensitivity needed for effective detection of metastasis. Recent advancements in PCa imaging, notably magnetic resonance imaging (MRI) and prostate-specific membrane antigen (PSMA) positron emission tomography-computed tomography (PET-CT), have enabled earlier detection and more precise localization of PCa, as well as more accurate exclusion of metastases. This progress, combined with PSA screening, has led to the diagnosis of PCa at earlier and more favourable stages of the disease.

In general, if the PCa is considered clinically significant, local treatment is recommended. Conventional first-line therapeutic options for PCa include radical prostatectomy (RP) and radiation therapy (RT). While they offer effective local cancer control, they can lead to substantial long-term complications affecting quality of life.

Despite efforts to eradicate the disease, recurrence can occur after conventional treatments, with up to half of RT patients experiencing biochemical recurrence (BCR) during their lifetime. Non-curative, systemic androgen deprivation therapy (ADT) is the standard treatment option for radiorecurrent PCa, but it carries significant long-term side effects. Consequently, there is an unmet need for locally effective primary and salvage PCa therapies with reduced morbidity.

To overcome the limitations of conventional therapies, alternative local treatment options like laser ablation (FLA), cryoablation and high-intensity focused ultrasound (HIFU) have emerged within the last few decades, aiming to offer comparable disease control with improved safety.

One of the newer alternatives is MRI-guided transurethral ultrasound ablation (TULSA), which has been utilized for different indications with encouraging initial outcomes. Fundamental difference with TULSA compared to other ablative treatment modalities is that it thermally coagulates the prostate via transurethral route ("inside-out") by delivering high-intensity, spatially directed ultrasound. MRI is used to both plan and monitor the treatment in real-time. While giving the benefit of accurate treatment delivery, MRI is unfortunately prone to artifacts, which may compromise the treatment success.

Following ablation treatments, there is typically residual untreated prostate tissue alongside the treated area, diminishing the utility of PSA in the follow-up. Therefore, imaging is even more important in the follow-up after ablation therapies.

In heat-based ablation therapies like TULSA, the main goal is to achieve necrosis on the dedicated area of the prostate. Tissue necrosis is measured by contrast-enhanced MRI as non-perfused volume (NPV). Even though NPV has traditionally served as a secondary marker for treatment outcome following heat-based ablation therapies, previous understanding regarding the evolution of NPV and the mechanism underlying NPV resolution remains limited. Additionally, subacute MRI findings after TULSA treatment correlated with histology, or the effect of radiotherapy fiducial markers on the outcome of ultrasound ablation have not previously been reported.

The present work aimed to offer insights into the use of TULSA as a salvage therapy for radiorecurrent PCa patients with intraprostatic fiducial markers, as well as the MRI findings following TULSA treatment.

2 Review of the Literature

2.1 Prostate anatomy and function

The prostate gland is an “inverted pyramid” -shaped organ, located in true pelvis between the urinary bladder and urogenital diaphragm. As a part of male reproductive system, the main purpose of prostate is to storage and secrete alkaline discharge to seminal fluid.

Having prostatic urethra as an anatomic reference point, the prostate gland is divided into four histologically distinct parts: peripheral zone (PZ), transition zone (TZ), central zone (CZ) and anterior fibromuscular stroma (AFS) (McNeal, 1981). Two thirds of PCa arise from the peripheral zone rich with glandular tissue, while transition zone is the primary site for BPH (McNeal, 1988; McNeal et al., 1988). The central zone surrounds the ejaculatory ducts, which join the seminal vesicles and ductus deferentes to the prostatic urethra. Non-glandular AFS covers the anterior aspects of the prostate (McNeal, 1981). The prostate gland is covered by a pseudocapsule, which is inseparable from prostatic stroma, and has defects in the apical region, bladder neck and at the site of ejaculatory duct entry (McNeal, 1988). Between the transition and peripheral zone there is also “surgical capsule” composed of a mesh of fibrous and muscular tissue (Rosenkrantz & Taneja, 2014; Semple, 1963).

Arterial blood supply to the prostate occurs via branches of the internal iliac arteries, and venous drainage by the prostate venous plexus joining the internal iliac veins. Branches of the inferior hypogastric plexus innervate the prostate. The small vessels and nerve fibers form a complex called the neurovascular bundle (NVB), which surround the posterolateral corners of the prostate (Rai et al., 2012). Lymphatic drainage of the prostate occurs primarily from the periprostatic area involving the deep branches of the internal iliac lymphatics, subsequently spreading to multiple pelvic nodal areas (Swanson & Hubbard, 2013).

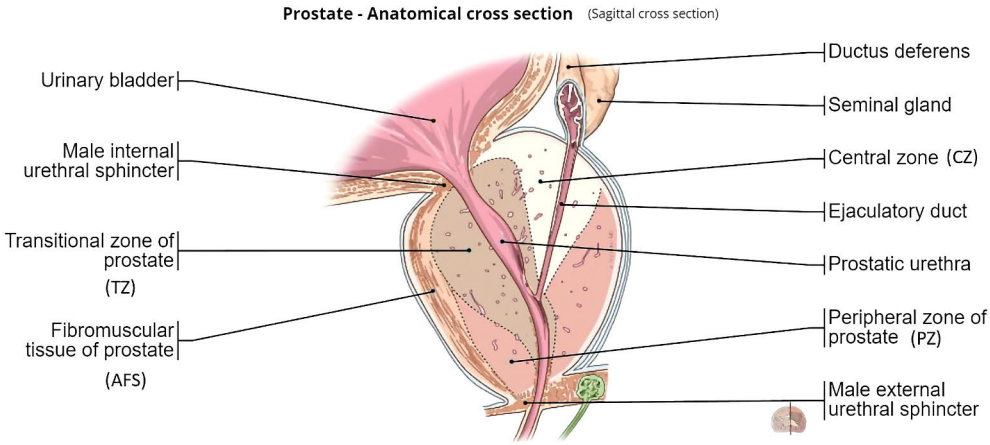

Figure 1. Sagittal view of prostate anatomy. (Modified illustration from IMAIOS, Courtesy of IMAIOS © "Micheau A, Hoa D, e-Anatomy, www.imaios.com, DOI: 10.37019/e-anatomy")

2.2 Benign prostatic hyperplasia (BPH)

The normal size of on adult prostate is considered 20 ± 6 g (Berry et al., 1984). Prostate size increases with age. BPH is rare in men under 30 but affects half of men over the age of 50 (Berry et al., 1984). For some men, BPH is asymptomatic, but it may also cause a variety of lower urinary tract symptoms (LUTS), differentiated into filling and voiding symptoms (Abrams, 1994). BPH-induced LUTS have a significant impact on patients' quality of life (QoL), and these symptoms can lead to complications such as urinary tract infections (UTI) and urinary retention (Devlin et al., 2021).

BPH can be defined as unregulated hyperplastic growth of the epithelial and fibromuscular tissues of the transition zone and periurethral area, leading to nodule formation and diffuse enlargement of transition zone (Devlin et al., 2021; McNeal, 1978). Development of BPH is a multifactorial process, but the definite pathology behind the disease remains still unclear (Devlin et al., 2021).

The diagnosis of BPH is usually based on typical symptoms, questionnaires such as the International Prostate Symptom Score (IPSS), uroflowmetry, and transrectal ultrasound (TRUS). Magnetic resonance imaging (MRI) provides additional value in BPH diagnostics, especially for treatment planning and follow-up. (Han et al., 2023).

Treatment of BPH

Watchful waiting along with lifestyle and dietary changes may be sufficient for men with mild to moderate BPH-related LUTS. However, when symptoms become

bothersome, medical interventions like α1-blockers and 5α-reductase inhibitors are typically needed (Gratzke et al., 2015). If the symptoms are not sufficiently alleviated by medical treatment, or the patient has inadequate tolerance for drug therapy, surgical approach is the subsequent option.

Surgical treatment for BPH consist of multiple techniques, which can be divided in five categories: 1. resection, 2. enucleation, 3. vaporisation, 4. alternative ablative techniques (such as aquablation and prostatic artery embolization) and 5. non-ablative techniques (mainly prostatic urethral lift). Based on the European Association of Urology (EAU) guidelines (Gratzke et al., 2015), the recommended methods with the strongest evidence are: transurethral incision (TUIP) for prostate volumes < 30 mL; transurethral resection (TURP) for prostate volumes of 30-80 mL; open prostatectomy, Holmium laser enucleation (HoLEP), or bipolar enucleation for prostate volumes > 80 mL; and laser vaporisation for high-risk patients.

Ultrasound-based ablation techniques, high-intensity focused ultrasound (HIFU) and transurethral ultrasound ablation (TULSA), are experimental treatment options for BPH. Few small cohort studies on both HIFU (Sciacqua et al., 2023) and TULSA (Elterman et al., 2021; Viitala et al., 2022) have shown encouraging short-term results in the management of LUTS, but strong evidence with larger cohorts and longer follow-up is lacking.

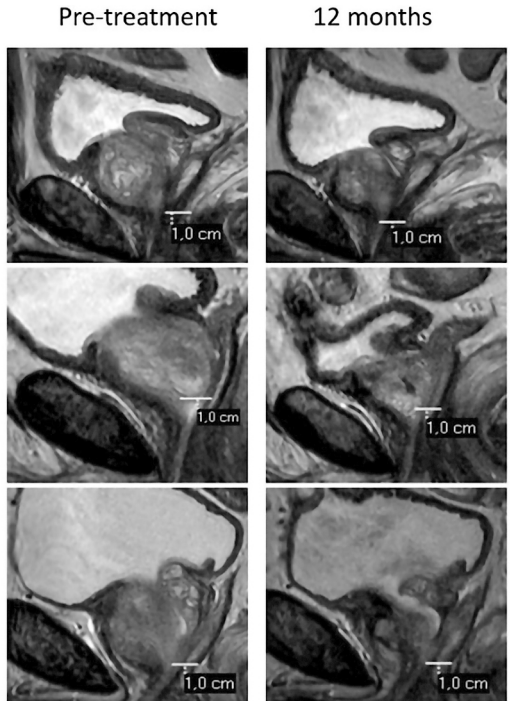

Figure 2. Patient examples on the effect of TULSA for BPH. (Modified from (Viitala et al., 2022)).

2.3 Prostate cancer (PCa)

Epidemiology, etiology, and risk factors

Prostate cancer (PCa) is the second most frequent cancer and the fifth leading cause of cancer death among men worldwide, with an estimation of 1.4 million new cases and 375 000 deaths in 2020 (Sung et al., 2021). PCa is uncommon for younger men, but its prevalence reaches almost 60% for men aged ≥ 80 years based on autopsy studies (Bell et al., 2015).

Increasing age, family history and ethnic background are well-established risk factors for PCa, but complete etiology of PCa remains largely unknown. Some dietary, exogenous and environmental factors have also been associated with the incidence and aggressiveness of PCa, but due to the lack of strong evidence, there are no specific preventive or dietary measures for reducing the risk of PCa (Mottet et al., 2022).

Histological grading

The vast majority of prostate tumors are adenocarcinomas, and their classification has historically relied on the Gleason grading system, initially introduced in 1966 (Gleason, 1966). Minor alterations have been made to this grading system over the past 50 years (Epstein et al., 2005). In 2014, the International Society of Urological Pathology (ISUP) consensus conference proposed a new grading system based on the original Gleason scoring system (Epstein et al., 2016), with an update in 2019 (van Leenders et al., 2020).

The original Gleason system assesses prostate tissue morphology on a scale of 1–5, with the Gleason score (GS) being calculated based on the sum of the two most common patterns observed in the prostate specimen. Consequently, the Gleason score theoretically ranges from 2 to 10, but patterns 1 and 2 are rarely reported. Therefore, Gleason scores typically fall between 6 and 10. The new ISUP grading system, categorizes prostate cancers into ISUP grade groups (GG) 1–5, aiming to provide a more accurate prognosis for current cancer cases.

Table 1. ISUP Gleason Grade Group system.

Gleason pattern	Gleason score	ISUP Grade Group
3+3	6	1
3+4	7	2
4+3	7	3
4+4, 3+5, 5+3	8	4
4+5, 5+4, 5+5	9 or 10	5

Intraductal carcinoma of the prostate (IDC-P) is a specific subtype of adenocarcinomas and is associated with a worse prognosis (Tsuzuki, 2015). The 2014 ISUP consensus conference determined that IDC-P without invasive carcinoma should not receive a Gleason grade.

Cribriform prostate cancer is a histological pattern primarily graded as a subtype of Gleason 3+3. However, its significance for prognosis has only become apparent in recent decades (Iczkowski et al., 2018). The cribriform pattern is associated with adverse prognostic features, independent of the underlying Gleason pattern. The 2014 ISUP consensus conference recommended assigning cribriform glands a Gleason score of 4, regardless of their morphology.

Neuroendocrine carcinoma (NECP) represents an aggressive subtype of prostate cancer, arising from neuroendocrine cells of the prostate. NECP can occur in pure form or coexist with adenocarcinoma. It has been suggested that NECP development may be linked to androgen resistance after long-term androgen deprivation therapy (ADT), with increasing neuroendocrine differentiation as adenocarcinoma progresses. NECP typically does not produce prostate-specific antigen (PSA) and is resistant to ADT (Parimi et al., 2014).

Other extremely rare types of PCa include mucinous carcinoma, lymphomas, and mesenchymal tumors such as sarcomas. Additionally, urothelial carcinoma may occur in the prostate without concurrent bladder involvement.

Staging

The primary aim of a tumor classification and staging system is to group individuals with similar clinical outcomes. This serves several important purposes, including facilitating discussions on prognosis with patients, enabling the design of clinical trials involving relatively uniform patient populations, facilitating comparisons of clinical and pathological data from different hospitals worldwide, and fostering the development of treatment recommendations for these specific patient cohorts. The EAU recommends using the Tumor, Node and Metastasis (TNM) classification (Brierley et al., 2017) for the staging of PCa.

T1-2 tumors are classified as organ-confined, and T3-4 tumors extend beyond prostatic capsule. The current practice for determining clinical T-stage relies on digital rectal examination. However, with advancements in prostate MRI and the increasing use of MRI-targeted biopsies, it is anticipated that radiological T-staging will likely find its way into future guidelines (Ploussard et al., 2020).

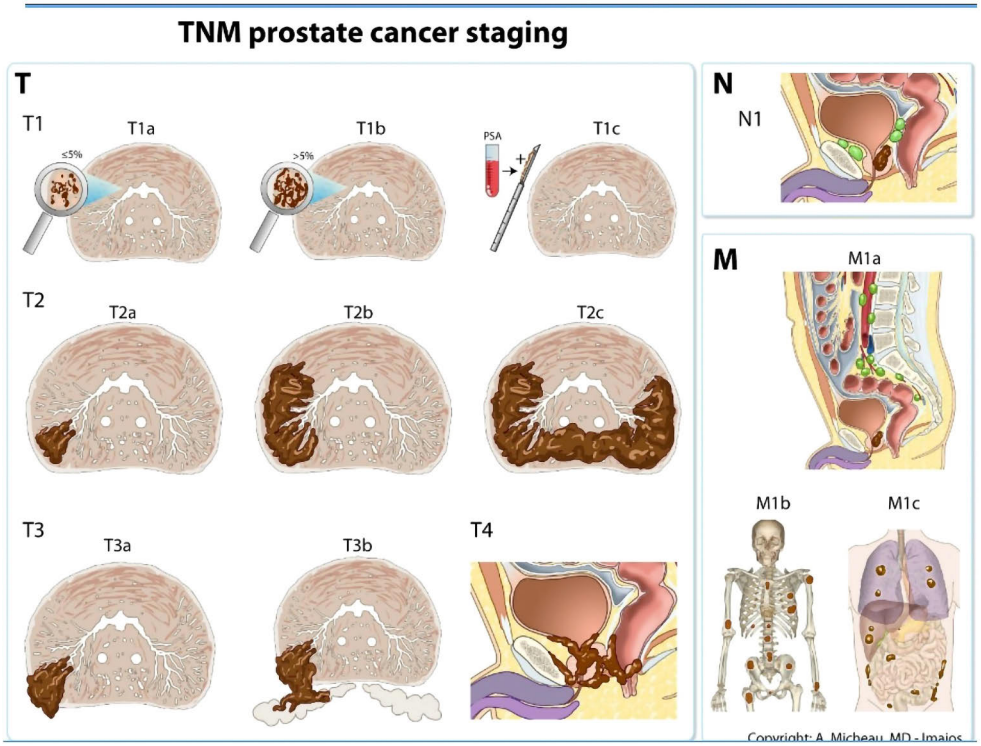

Figure 3. TNM classification AJCC 8th edition 2017. (Modified illustration from IMAIOS, Courtesy of IMAIOS © "Micheau A, Hoa D, e-Anatomy, www.imaios.com, DOI: 10.37019/e-anatomy")

The EAU has developed a risk group classification for prognostic subgrouping of PCa patients (Mottet et al., 2022); see **Table 2**. There is some professional disagreement on the definition of clinically significant prostate cancer (csPCa). Nearly all men classified in the EAU low-risk group have clinically indolent or insignificant cancer, whereas in the high-risk group, cancer is almost invariably clinically significant. A Gleason score of ≥ 7 is most commonly used as the threshold for csPCa.

Table 2. EAU risk group classification.

Low-risk	**Intermediate-risk**	**High-risk**	
PSA < 10 ng/mL	PSA 10-20 ng/mL	PSA > 20 ng/mL	any PSA
and GS < 7 (ISUP grade 1)	or GS 7 (ISUP grade 2/3)	or GS > 7 (ISUP grade 4/5)	any GS (any ISUP grade)
and T1-2a	or T2b	or T2c	T3-4 or N+
Localized			Locally advanced

2.3.1 Primary diagnosis

In its early stages, prostate cancer typically remains asymptomatic. Nevertheless, when PCa presents with symptoms, these manifestations frequently mimic those seen in BPH and other disorders associated with urinary issues, including prostatitis, urinary tract infections, bladder dysfunction, urethral stricture, and bladder tumors. Occasionally, the initial sign of PCa may manifest as bone pain or a pathological fracture resulting from metastases.

PCa is typically suspected either through digital rectal examination (DRE) of the prostate or when there is an elevated PSA level. Even though most of the tumors are located in the peripheral zone of the prostate, DRE identifies only every fifth cancer. Combining PSA testing with DRE substantially improves the detection rate (Richie et al., 1993). The definitive diagnosis relies on a histopathological examination of tissue biopsies.

PSA

PSA is the most frequently utilized biomarker in the diagnosis of prostate cancer. It is an androgen-regulated serine protease that is primarily synthesized by prostate luminal epithelial cells. PSA is secreted in high concentrations through prostatic ducts into semen, where it plays a crucial role in liquefying the seminal coagulum to facilitate the release of spermatozoa.

In men without prostate pathology, PSA is normally present in small amounts in the bloodstream. Elevated levels of serum PSA are believed to result from the disruption of the prostate gland's basement membrane and normal cellular structure, particularly in adenocarcinomas lacking basal cells. This disruption leads to increased leakage of PSA into the bloodstream (McDougal et al., 2015). It is important to note that while PSA is organ-specific, it is not cancer-specific, meaning that elevated PSA levels can also be seen in other non-malignant prostate conditions, for example BPH and prostatitis (McDougal et al., 2015).

The use of PSA as a serum biomarker has revolutionized the diagnosis of PCa by enabling earlier detection. Initially introduced in the 1980s for monitoring treatment response in patients who had undergone radical treatment for PCa (Kuriyama et al., 1981; Stamey et al., 1987), PSA measurement was subsequently adopted for cancer screening, which has led to significant increase in the diagnosis of PCa and the detection of more localized and less advanced forms of the disease (Mottet et al., 2022). However, it is worth noting that no significant improvement in cancer-specific or overall survival has been observed as a result of PSA-based screening (Mottet et al., 2022).

Imaging

The primary imaging method for the prostate is typically transrectal ultrasound (TRUS), which has been used since the 1970s and is usually performed by a urologist. However, TRUS is known to have limited sensitivity and specificity in detecting PCa (Onur et al., 2004). Hence, its primary role is usually to guide biopsies rather than serve as a diagnostic tool.

In the last two decades the technological advancements and increased accessibility of MRI have marked a significant breakthrough in the field of PCa diagnosis. It is not only used in the detection of csPCa, but also in local tumor staging, characterization, risk stratification, surveillance, assessment of suspected recurrence, image guidance for biopsy, and treatment planning. The creation of the standardized prostate imaging and reporting system (PI-RADS), developed in collaboration with the European Society of Urogenital Radiology (ESUR) and the American College of Radiology (ACR), has reduced variations in imaging techniques between different centers and in the image interpretation between individual readers. This development has paved way for worldwide adoption of prostate MRI. Currently, PI-RADS, with its latest version 2.1 introduced in 2019 (Turkbey et al., 2019), stands as the golden standard guideline for assessing prostate MRI. In the PI-RADS system, lesions are categorized using a 5-point scoring system. Lesions with a score of 1 are deemed highly improbable for csPCa, whereas those with a score of 5 are considered highly likely for csPCa (see **Figure 4)**. Typically, a threshold of ≥ 3 is used for suspicious lesions. It should be noted that PI-RADS is designed only for the assessment of treatment-naïve prostate glands.

The PI-RADS Steering Committee advises the use of multiparametric MRI (mpMRI), which includes dynamic contrast-enhanced sequence in addition to T1-, T2-, and diffusion-weighted sequences. However, there is increasing evidence suggesting that a more cost-effective and less time-consuming approach with biparametric MRI (bpMRI), without the use of contrast media, would be comparable in the detection of csPCa (Bass et al., 2021). When compared to prostatectomy or biopsy specimens, MRI has good sensitivity in the detection of csPCa (Bratan et al., 2013; Drost et al., 2019; Johnson et al., 2019), with less sensitivity detecting clinically insignificant cancer (Bratan et al., 2013). This has led to increased use of MRI-targeted prostate biopsies for both biopsy-naïve patients and patients with prior negative biopsies (Drost et al., 2019; Kasivisvanathan et al., 2018; Rouvière et al., 2019; van der Leest et al., 2019). There is growing interest on the possibility of not performing biopsies on patients with negative (PI-RADS score < 3) MRI results (Panebianco et al., 2018), but additional research is required to explore this concept further.

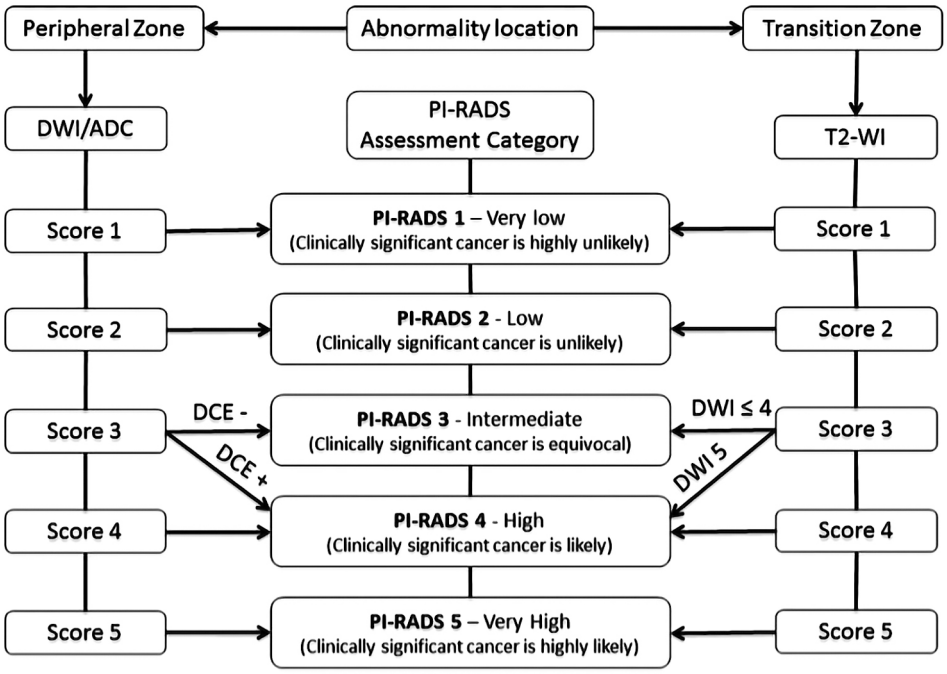

Figure 4. PI-RADS v 2.1 scoring for lesions in prostate MRI. (Purysko et al., 2016)

Compelling evidence supporting the utilization of prostate MRI has been incorporated into clinical guidelines. The EAU recommends using MRI before biopsies and combining MRI-targeted to systematic biopsies with positive MRI (Mottet et al., 2022). For patients with prior negative biopsies and negative MRI, but with ongoing clinical suspicion of PCa, systematic biopsies are recommended (Mottet et al., 2022).

While prostate MRI is a valuable tool for assessing the local stage of PCa (de Rooij et al., 2016), other imaging techniques are employed and remain essential for lymph node (N) and metastasis (M) staging. In accordance with the EAU guidelines (Mottet et al., 2022) additional imaging and staging are not needed for low-risk patients. Intermediate- and high-risk patients should undergo at least abdominopelvic computed tomography (CT) and/or magnetic resonance imaging (MRI), in addition to a bone scan (BS). However, positron emission tomography (PET) -based imaging with especially prostate-specific membrane antigen (PSMA) tracer and fusion to CT is rapidly evolving and widely interesting method in PCa staging (Hofman et al., 2020).

The European Association of Nuclear Medicine (EANM) has recently published updated practical guideline aiming to support physicians in recommending, acquiring, interpreting, and reporting the results of PSMA-ligand PET-CT for initial

diagnosis, staging, and restaging of PCa (Fendler et al., 2023). PSMA is an enzymatic transmembrane protein located on the cell membrane. It is expressed in approximately 98% of primary tumors and metastases in PCa, and its expression tends to increase as the disease becomes less differentiated (Mease et al., 2013; Silver et al., 1997; Su et al., 1995; Sweat et al., 1998; Uprimny et al., 2017). However, despite its name, PSMA is not exclusively specific to the prostate. It can also be found in ganglia, salivary glands, liver, spleen, small intestine, and kidney. Additionally, many other benign and malignant tumors have been observed to express PSMA (Sheikhbahaei et al., 2019).

N-staging is typically carried out using CT or abdominal/pelvic MRI, which exhibit sensitivities of approximately 40% (Hofman et al., 2020; Hövels et al., 2008). PSMA-PET-CT has emerged as a candidate for N-staging. Reported sensitivity and specificity values for 68Ga-PSMA PET, the most widely used PSMA tracer, are 77% and 97%, respectively (Perera et al., 2020). PSMA-PET-CT currently stands as the most effective modality for N-staging, although its relatively lower spatial resolution may still result in the oversight of smaller lymph node metastases (Mottet et al., 2022).

Bones and distant lymph nodes are the most common sites for metastasis in advanced PCa (Gandaglia et al., 2014). Bone scan has traditionally been the modality of choice in the assessment of bone metastasis. A meta-analysis conducted by Shen et al reported a pooled sensitivity of 79% and specificity of 82% when using a bone scan for the detection of bone metastases (Shen et al., 2014). More recently, whole-body MRI and PSMA-PET-CT have gained prominence (Hofman et al., 2020; Van Nieuwenhove et al., 2022), showing better results than bone scan. However, additional clinical evidence is required to firmly establish MRI and PSMA-PET-CT as the gold standards for N- and M-staging. As the field of imaging in PCa continues to evolve, these standards may change in the future (Mottet et al., 2022).

Prostate biopsies

Histopathological confirmation of PCa is achieved by prostate biopsies, usually with TRUS or MRI guidance. When deemed necessary, a physician may recommend a prostate biopsy to confirm abnormalities identified during a DRE, abnormal PSA levels, or findings from imaging studies. In accordance with current European guidelines (Mottet et al., 2022), prostate MRI is recommended before biopsies, and if the MRI yields a positive finding with a PI-RADS score of ≥ 3, it is recommended that all prostate biopsies encompass both systematic and targeted approaches.

Prostate biopsies can be conducted through either transrectal or transperineal route, with a preference for the transperineal approach outlined in the EAU guidelines (Mottet et al., 2022). No statistically significant difference has been found

in the detection rate of csPCa between cognitive and software-assisted fusion biopsy techniques (Pirola et al., 2023; Watts et al., 2020). For systematic biopsies, a minimum of eight cores should be obtained, and in the case of larger prostates, this number may increase to 10–12 cores. Should the physician opt for additional targeted biopsies, a minimum of 3–5 cores should be extracted from each suspicious area identified on the MRI (Mottet et al., 2022).

2.3.2 Treatment of localized PCa

Prostate cancer encompasses a broad and diverse range, spanning from indolent, asymptomatic, and clinically insignificant cases to aggressive and lethal disease. The earlier detection of PCa with more favourable disease characteristics can be attributed to the raised awareness of the condition, advancements in diagnostic techniques, and the screening of men with elevated PSA levels (Cooperberg et al., 2005; Fenton et al., 2018). When a significant portion of PCa patients is diagnosed with low-risk disease, there is genuine concern that overdiagnosis and overtreatment may cause more harm than the disease itself (Fenton et al., 2018; Klotz, 2022). Consequently, active surveillance (AS) emerges as a suitable option for many favourable-risk patients, as an alternative to immediate radical therapies (Thomsen et al., 2014; Tosoian et al., 2015). There is no unanimous consensus on the preferred protocol for active surveillance (AS), but the PRIAS (Prostate Cancer Research International: Active Surveillance) protocol (Bul et al., 2013) is commonly used in Finland. The inclusion criteria for this protocol include men who are fit for curative treatment, with a PSA at diagnosis of < 10 ng/mL, PSA density < 0.2, ≤ 2 biopsy cores with PCa involvement, ISUP GG 1, and T-stage T1c or T2. The PRIAS follow-up protocol involves regular PSA testing, DRE, MRI, and repeated prostate biopsies. AS has demonstrated outstanding outcomes for low-risk patients identified through screening, achieving a 10-year overall survival rate of 92% and a cancer-specific survival rate of 100% (Mottet et al., 2022).

For patients whose life expectancy is less than 10 years, and who are not suitable candidates for curative treatments, watchful waiting with personalized follow-up protocol may be adequate to minimize the potential toxicity associated with treatment (Mottet et al., 2022).

2.3.2.1 Conventional therapies

Radical prostatectomy (RP) is a surgical procedure aimed at removing the entire prostate and seminal vesicles. It is commonly performed using laparoscopic approach with or without robotic assistance (RALP). Depending on the specific characteristics of the disease and the patient's preferences, variations of the technique

may be employed, such as nerve-sparing (Moris et al., 2022; Walsh & Mostwin, 1984) or seminal vesicle -sparing surgery (Gilbert et al., 2017). The effectiveness of RP, especially for lower-risk PCa, remains a topic of debate. One long-term randomized controlled trial (RCT) (Bill-Axelson et al., 2018) reported benefits of RP compared to watchful waiting, with a mean of 2.9 years of life gained over a follow-up period of 23 years. Another long-term RCT, the PIVOT study (Wilt et al., 2020), with 12 years of follow-up, found no overall or cancer-specific survival benefit for RP when compared to observation. It is important to note that RP also carries a significant risk of adverse effects, with roughly 20% of patients being urinary incontinent and 70% having erectile dysfunction as chronic complications (Haglind et al., 2015), in addition to unplanned hospital visits for various perioperative complications (Mukkala et al., 2021).

Another curative-intent local treatment option for PCa is radiation therapy (RT), which employs ionizing radiation to target and eliminate cancerous tissue. RT can be administered to the prostate using either external beam therapy (EBRT) or brachytherapy. EBRT utilizes various techniques, including intensity-modulated, volumetric arc, or image-guided radiation therapy, to precisely deliver radiation doses to the prostate while minimizing exposure to surrounding healthy tissues. To enhance visualization during EBRT, fiducial markers are often implanted in the prostate prior to treatment (O'Neill et al., 2016). The recommended radiation dose for patients undergoing EBRT typically ranges from 74 to 80 Gray (Mottet et al., 2022). Especially for intermediate- and high-risk patients, androgen deprivation therapy (ADT) is usually combined with EBRT (Bolla et al., 2010; Jones et al., 2011). Brachytherapy is divided into low-dose-rate (LDR) and high-dose-rate (HDR) treatments. Based on the EAU guidelines, LDR brachytherapy may be offered to patients with good urinary function and low-risk or favourable intermediate-risk disease. The use of HDR has not yet established a well-defined position. Much like radical prostatectomy, radiation therapy is linked to a substantial risk of long-term side effects, including urinary incontinence, erectile dysfunction, and gastrointestinal toxicity (Resnick et al., 2013).

Choosing between AS, RP, or RT is a multifaceted decision influenced by factors such as the patient's risk group for PCa, life expectancy, and individual preferences. This decision-making process is further complicated by the relatively low risk of death from PCa. In the ProtecT trial (Hamdy et al., 2016), which consisted of low- and intermediate-risk patients, no statistically significant difference was observed between AS, RP and RT in mortality. However, lower rates of disease progression and metastases were observed in both RP and RT groups when compared to AS at the 10-year follow-up point. In general, the EAU guidelines recommend AS for low-risk patients, RP / EBRT / LDR brachytherapy for favourable intermediate-risk

patients, and either RP or EBRT for unfavourable intermediate-risk and high-risk disease in patients with a life expectancy exceeding 10 years (Mottet et al., 2022).

2.3.2.2 Ablative therapies

As traditional radical treatment approaches for PCa, including RP, RT, and brachytherapy, are associated with a substantial incidence of adverse effects (Haglind et al., 2015; Mukkala et al., 2021; Resnick et al., 2013), there has been a growing demand for alternative treatment modalities that offer a balance between effectiveness and reduced adverse effects. Since the 1990s, a variety of minimally invasive ablation techniques have been explored and researched as potential solutions to address this concern (Valerio et al., 2017). High-intensity focused ultrasound (HIFU) and cryotherapy are the most studied methods so far.

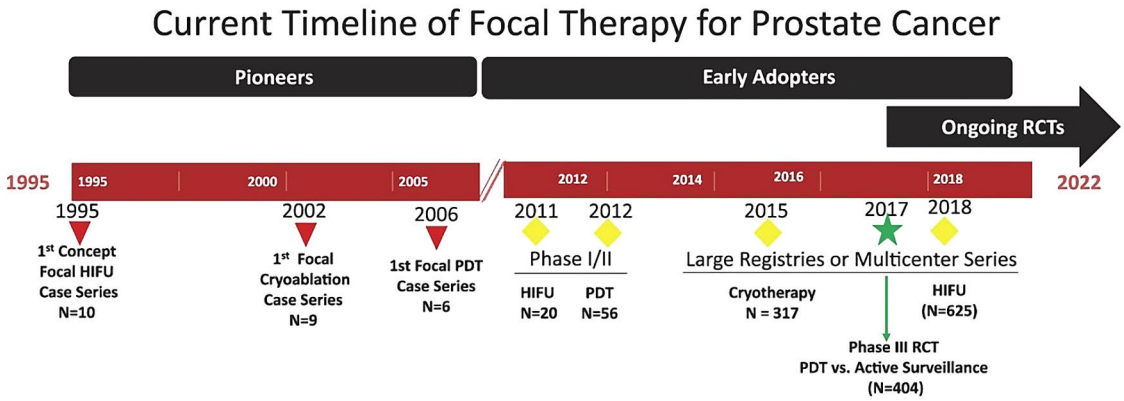

Figure 5. Evolution of focal PCa treatments. (Adapted from (Labbate et al., 2023))

Ablation therapies can be used to treat only part of the prostate (focal approach) or the whole gland. Due to exponentially grown PSA screening, nowadays PCa is detected earlier, and we are encountering an increasing number of localized lower risk cases (Hayes & Barry, 2014; Ilic et al., 2018; Polascik et al., 2008). Although PCa often presents as multifocal disease, research suggests that the clinical outcome of PCa is primarily determined by the index lesion (Ahmed et al., 2012; Algaba & Montironi, 2010; Karavitakis et al., 2011; Wise et al., 2002), while secondary low-grade lesions tend to exhibit an indolent behaviour. The introduction of prostate MRI has significantly enhanced disease characterization and tumor localization, leading to more precise risk assessment. Prostate MRI is highly accurate in the detection of the index lesion and ruling out clinically significant cancer (Fütterer et al., 2015). This has driven towards focal therapy (FT), in which usually only the index lesion is

treated with margins and rest of the prostate and surrounding tissues are left untreated. Focal ablation appears to be associated with fewer adverse effects, even though there is only a limited number of studies directly comparing focal and whole-gland ablation strategies (Borges et al., 2021; Lumiani et al., 2021; Mendez et al., 2015).

HIFU

The basic principle of prostate HIFU involves positioning an ultrasound transducer in the rectum, from which it emits focused high-intensity ultrasound waves directed at a specific location within the prostate. These intense ultrasound waves are absorbed and quickly elevate the temperature in the targeted prostate tissue to over 60 °C, leading to immediate coagulation necrosis primarily resulting from hyperthermia and acoustic cavitation (Madersbacher & Marberger, 2003; Zhou, 2011). The process involves repeated ablative sonications to ensure comprehensive coverage of the whole targeted area within the prostate. First commercial prostate HIFU devices used ultrasound in the real-time guidance of ablation, but newer devices rely on more accurate MRI-guidance (Sundaram et al., 2017). The transrectal approach in HIFU poses challenges in effectively targeting anterior tumors due to their distance from the ultrasound source and the prostate swelling during treatment (Huber et al., 2021).

HIFU has been widely used for whole-gland therapy with the following adverse effects: acute urinary retention (10%), erectile dysfunction (23%), urethral stricture (8%), rectal pain or bleeding (11%), recto-urethral fistula (0–5%) and urinary incontinence (10%) (Mottet et al., 2022; Ramsay et al., 2015). The absence of comprehensive, long-term, comparative data on cancer treatment outcomes, along with the inability to significantly reduce the side effects, hinders the consideration of whole-gland HIFU as a viable alternative to established curative treatment options (Mottet et al., 2022).

To reduce adverse effects faced in whole-gland HIFU, there has been an increasing trend towards focal treatment approach. In a recent systematic review on focal therapies (Hopstaken et al., 2022), it was found that there is substantial evidence indicating that focal HIFU is linked to minimal adverse events. Another study (Lovegrove et al., 2020) showed that possible re-treatment with HIFU does not substantially deteriorate the functional outcome. However, conclusive evidence regarding the oncological effectiveness of focal HIFU in comparison to the standard of care is still pending.

Cryotherapy

Cryotherapy employs freezing methods to induce cell death through dehydration, which leads to protein denaturation, the direct rupture of cellular membranes by ice crystals, and the induction of vascular stasis and microthrombi formation. This, in turn, causes a halt in microcirculation, resulting in subsequent ischemic apoptosis (Han & Belldegrun, 2004). The freezing of the prostate is achieved by inserting 17-gauge cryo-needles under the guidance of transrectal ultrasound, placing thermosensors at the level of the external sphincter and rectal wall, and introducing a urethral warmer. The process involves two freeze-thaw cycles, also guided by TRUS, resulting in a target temperature of -40 °C. Presently, third and fourth generation cryotherapy devices are predominantly used. Both whole-gland and focal ablation strategies have been employed.

The primary adverse effects associated with whole-gland cryosurgery include erectile dysfunction (18%), urinary incontinence (ranging from 2% to 20%), urethral sloughing (ranging from 0% to 38%), rectal pain and bleeding (3%), and the formation of recto-urethral fistulas (ranging from 0% to 6%) (Ramsay et al., 2015). There is a notable absence of prospective comparative data on the oncological outcomes of whole-gland cryosurgery as a curative treatment option for men with localized PCa. Most studies available are non-comparative, single-arm case series with limited follow-up periods (Ramsay et al., 2015).

Other ablative methods

In photodynamic therapy (PDT), focal laser ablation (FLA), radiofrequency ablation (RFA) and irreversible electroporation (IRE) prostate is approached with transperineally inserted fibers or needles.

PDT is a technology that accomplishes the destruction of targeted tissues by utilizing a light-sensitive agent (photosensitizer), which is administered intravenously, and it accumulates preferentially in the blood vessels of the tumor. Activation of the photosensitizer occurs through laser light of a specific wavelength, which is delivered transperineally into the prostate using optical fibers. The photosensitizer absorbs light and transfers this energy to nearby oxygen molecules, generating reactive oxygen species that initiate the destruction of cells (Ramsay et al., 2015).

FLA involves the use of a precisely directed laser beam guided by MRI to induce thermal destruction of prostatic tissue. Tissue destruction occurs by local coagulative necrosis, with temperatures ranging from 42 °C to more than 60 °C (Lindner, Lawrentschuk, & Trachtenberg, 2010; Ramsay et al., 2015).

RFA is a procedure that utilises low-level radiofrequency energy to heat and ablate tissue in a focused manner. Tissue destruction is achieved by coagulative necrosis resulting from heating tissues to 100 °C for 5 minutes (Shariat et al., 2005).

IRE is a method that involves the generation of high-frequency electric pulses between two or more electrodes. The resulting electric current disrupts the cell membrane, enabling molecules to pass into the cell through passive means, leading to cell death due to the inability to maintain cellular homeostasis (Scheltema et al., 2016).

These mentioned techniques have primarily been examined in small cohort studies with limited follow-up periods, and they have not been adequately compared to conventional PCa treatments. While they seem to result in minimal side effects, the effectiveness in treating PCa remains uncertain due to the absence of high-quality prospective comparative studies (Ramsay et al., 2015; Valerio et al., 2017).

2.3.2.3 Transurethral ultrasound ablation of prostate (TULSA)

Basics of ultrasound

The term "ultrasound" is fundamentally the propagation of mechanical longitudinal sound waves with a frequency higher than what the human ear can detect, i.e. frequencies exceeding 20 kHz. The frequency of an ultrasound wave consists of the number of cycles or pressure changes that occur in one second. The units are cycles per second or hertz. In clinical use frequencies ranging from 1 MHz to 10 MHz are typically utilized. The wavelength (λ) of a sound is the distance between adjacent identical parts of a wave, and it is inversely related to the frequency (Samei & Peck, 2019).

In medical imaging, ultrasound waves are created using transducers, comprising multiple interconnected piezoelectric crystals that vibrate when subjected to an electrical current. When these vibrating mechanical sound wave pulses travel through a spesific medium, the particles within the wave´s path deviate from their initial positions. These particles go through a sequence of compression and rarefaction (“decompression”). In the compression phase, the material encounters positive pressure, while in the rarefaction phase, the pressure becomes negative.

The mechanical energy loss of ultrasound waves is influenced by several factors, which encompass scattering, absorption, refraction, and reflection (Samei & Peck, 2019). The physical medium in which the ultrasound wave originates and propagates plays a crucial role in determining the extent of energy loss due to reflections. Two specific material properties, density, and the speed of ultrasound within the medium, combine to create the acoustic impedance. These values are unique for various materials like water, bone, metal, and air. Significant differences in acoustic

impedance result in substantial reflections. For instance, when ultrasound waves transition from prostate tissue to gold, approximately 90% of the energy is reflected.

Besides reflections, the ultrasound wave experiences energy dissipation as it traverses deeper into the same material. The degree of this energy loss (attenuation) is determined by the material's intrinsic properties, the frequency of the ultrasound wave, and the thickness of the material. Noticeable variations in attenuation are observed among air, water, prostate, muscle, bone, and metal.

Attenuation encompasses two primary elements: absorption and scattering. As the driving frequency of ultrasound source increases, the resulting attenuation also rises. The energy absorbed by the tissue is transformed into heat (Samei & Peck, 2019).

Basics of thermal ablation

Thermal ablation involves the exposure of tissue to either significantly elevated temperatures (hyperthermia) or reduced temperatures (hypothermia), with the aim of irreversible cell damage. For prostate ablation the most used hyperthermic methods are HIFU, laser ablation, and more recently TULSA, while cryotherapy relies on hypothermic tissue damage. The focus in this thesis is on hyperthermic ablation.

Hyperthermic ablation induces irreversible cellular injury, resulting in apoptosis and coagulative necrosis (Brace, 2011; Chu & Dupuy, 2014). Following rapid exposure to elevated temperatures, tissue response can be divided in three distinct regions: the central area of coagulative necrosis, the untreated zone, and a margin zone between (Boyes et al., 2007; Chu & Dupuy, 2014). In the coagulative necrosis zone, cells are obliterated, with no coherent structure. The outermost untreated zone remains unaffected but can display signs of oedema. The intermediate margin area is the most heterogeneous, where tissues may retain their glandular structures but may also undergo epithelial disorganization and delayed cellular necrosis. The width of the margin zone can extend up to 5 mm (Bomers et al., 2017; Boyes et al., 2007; Chopra et al., 2012).

The biological effect of temperature rise relies on both the temperature and the duration of the heating. The thermal dose associated with any temperature pattern can be computed using a method introduced in 1980s (Sapareto & Dewey, 1984). This approach employs numerical integration to determine cumulative equivalent minutes corresponding to the thermal dose at a reference temperature, typically set at 43 °C (CEM43). The correlation between thermal dose and temperature pattern is delineated as follows:

$$\textbf{Thermal Dose} = \int_0^t R_{CEM}^{(43-T(t))}\, dt \qquad (1)$$

where t is the exposure duration in minutes, T is the achieved temperature in °C, and R is a constant whose value is 0.25 for temperatures < 43 °C and 0.5 for temperatures > 43 °C.

The critical thermal dose for inducing tissue necrosis has been demonstrated to range from 30 to 250 CEM43, depending on the specific tissue type (Fan, 1995). Typically, a value of 240 CEM43 has been used as a universal threshold for the thermal dose that leads to complete necrosis in most tissue types (Burtnyk et al., 2015; Fan, 1995; Hazle et al., 2002; McDannold et al., 2000; Venkatesan et al., 2012), including the prostate (Hazle et al., 2002).

TULSA

Similar to HIFU, TULSA uses high-intensity ultrasound energy to target and destroy prostatic tissue. The primary divergence lies in their delivery methods: TULSA administers ultrasound energy transurethrally (inside-out) in a direct linear manner, whereas HIFU utilizes a transrectal route (outside-in) with a focused approach. TULSA has been applied to treat various prostate conditions, including whole-gland (Klotz et al., 2021) and focal (Anttinen et al., 2019; Lumiani et al., 2021) primary PCa treatments, palliative (Anttinen, Mäkelä, Nurminen, et al., 2020) and salvage (Anttinen, Mäkelä, Viitala, et al., 2020) approaches, as well as BPH (Viitala et al., 2022). The TULSA procedure is performed entirely in the MRI suite, with the patient under general anaesthesia and in a supine position.

The TULSA system comprises a transurethrally-inserted ultrasound applicator (UA), a rigid 22 French catheter with a coude-tip and a central channel for guidewire insertion to facilitate instrumentation. The UA features an acoustic window, which includes a linear array of ten individual transducer elements (5 mm x 4.5 mm), enabling the ablation of prostate tissue up to 5 cm in the craniocaudal direction. These elements emit directional, unfocused high-intensity ultrasound energy directly from within the prostatic urethra into the adjacent prostatic tissue, reaching distances of up to 3 cm from the centre of the urethra. Each transducer element is independently controlled and operates at either of the two frequencies, 4 or 13 MHz, using acoustic power up to 4 W. The rotational movement of the ultrasound elements provides 360-degree coverage of the prostate in the axial plane.

A specifically designed fluid circuit of degassed water running through the UA and the endorectal cooling device (ECD) is used to cool the urethra and rectum during treatment, mitigating the risk of thermal injury. The proximal end of the UA is connected to a MR-compatible positioning system (PS), affixed to the patient table in the MRI suite. The robotically driven and automated PS securely holds the UA in place, facilitating rotational motion to direct energy to user-specified regions of the prostate.

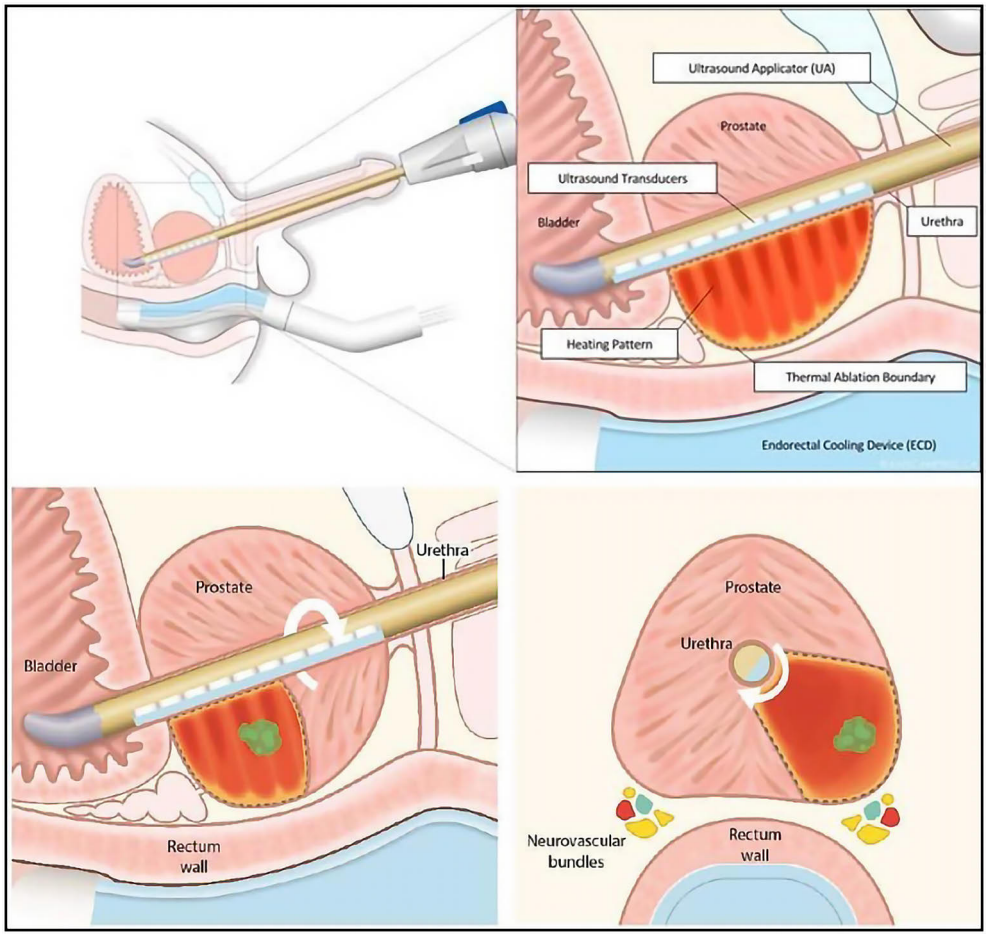

Figure 6. Illustration of the ultrasound applicator and endorectal cooling device inserted into the patient (upper row), and lesion-targeted tumor ablation (lower row). (Courtesy of Profound Medical Inc).

A user-controlled treatment delivery console is incorporated into the TULSA system for shaping the target prostate boundary during therapy planning, monitoring real-time thermal delivery, and implementing a proprietary temperature feedback control algorithm. The specific goal of TULSA treatment is to ensure that all prostate tissue located two millimetres inside the physician's target boundary gains a temperature increase of 57 °C. To achieve this, TULSA utilizes a closed-loop controller that actively monitors the temperature distribution within the target boundary. The software regulates therapy by adjusting acoustic power, rotation rate, and ultrasound frequencies to precisely confine thermal therapy delivery to the preplanned target region. The feedback control algorithm incorporates information from MR-thermometry images acquired every six seconds to control the therapy.

The TULSA system has demonstrated a thermal linear targeting accuracy of less than 2 mm (Anttinen et al., 2019; Siddiqui et al., 2010). Typically, the evaluation of treatment outcome involves visual assessment of thermal maps, encompassing maximum temperature and thermal dose, along with the non-perfused volume (NPV) obtained from gadolinium-enhanced MRI.

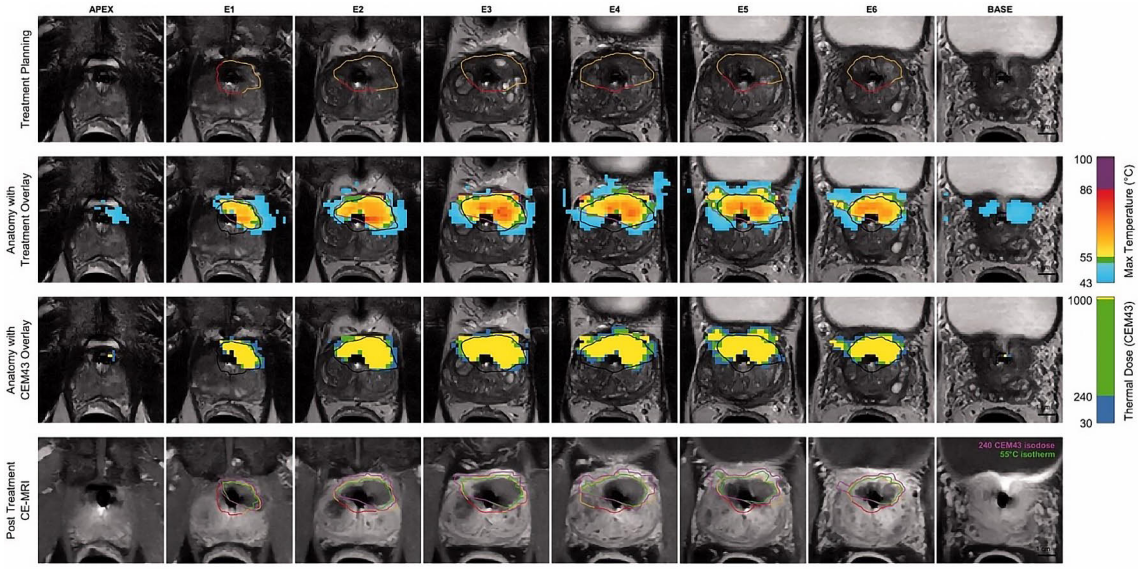

Figure 7. An illustrative case of focal PCa treatment, involving treatment planning, thermal maps, and the non-perfused volume immediately after the procedure. (Adapted from (Anttinen et al., 2019))

2.3.3 Follow-up

The purpose of patient follow-up is to evaluate both short-term and long-term oncological outcomes, ensure treatment compliance, and initiate additional therapy as necessary. Moreover, follow-up serves to monitor the occurrence of treatment-related side effects and complications, assess functional outcomes, and provide psychological support. (Mottet et al., 2022)

Follow-up after conventional therapies

Measurement of PSA is the cornerstone of follow-up after RP and RT. Nevertheless, PSA values alone are not adequate to determine the clinical significance of biochemical recurrence (BCR) on prognosis and survival. Therefore, it is essential to assess other risk factors, such as a rapid PSA doubling time and a high post-RP Gleason score, as well as a brief interval to biochemical failure and an elevated

biopsy Gleason score after RT (Van den Broeck et al., 2019). Following RP, the PSA level is expected to be undetectable, and BCR can be considered as any rising PSA value. The threshold that best predicts further metastasis is a PSA > 0.4 ng/mL (Toussi et al., 2016). Following RT, PSA levels drop more slowly. BCR after RT is commonly defined as a PSA increase of > 2 ng/mL from the nadir value (Roach et al., 2006).

PSA measurement after curative-intent therapies is commonly determined every six months until three years and yearly thereafter. Imaging is not typically utilized in the regular follow-up of localized PCa if there is no increase in PSA levels. Imaging is only warranted in patients for whom the results would impact treatment choices, either in cases of BCR or in those with symptoms (Mottet et al., 2022).

Imaging after BCR has traditionally relied on excluding metastases with CT and bone scan, even though BCR precedes clinical metastases by 7–8 years on average (Pound et al., 1999). In order to use local salvage treatment methods efficiently, a more precise evaluation on the nature of the recurrent disease is necessary. Newer imaging modalities, including prostate MRI and PSMA-PET-CT, have displayed promising results in the local staging of radiorecurrent disease and excluding metastases, which is crucial information in the planning of salvage therapies (Panebianco et al., 2021; Perera et al., 2020; Rasing et al., 2022; Rouvière et al., 2010). Since the PI-RADS classification is exclusively applicable to treatment-naïve prostates, a novel MRI reporting system known as PI-RR has been developed for the detection and staging of local recurrence after RP and RT (Panebianco et al., 2021).

Follow-up after ablation therapies

Given the experimental status of ablation therapies, which are not established as standard PCa treatments, there are currently no universal guidelines for patient follow-up. However, in 2015, a Delphi consensus project involving a panel of experts comprising urologists, radiologists, and biomedical engineers, generated a recommendation for a follow-up scheme (Muller et al., 2015). A surveillance plan of at least five years following focal therapy is recommended, involving repeated PSA testing, mpMRI and prostate biopsies. MRI follow-up scheme is shown in **Figure 8**.

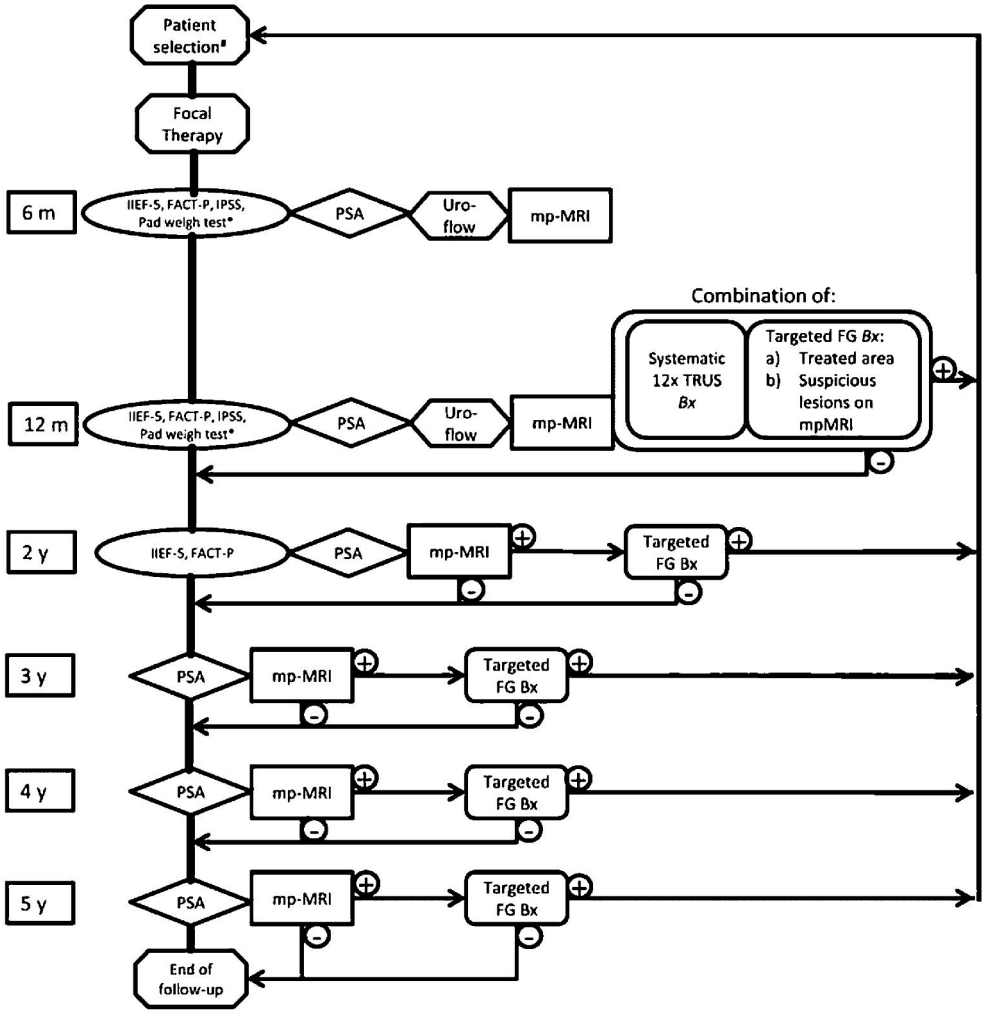

Figure 8. MRI follow-up scheme after focal therapy of prostate cancer. (Adapted from (Muller et al., 2015))

Another report from an expert consensus meeting, initially presented in 2015 (Donaldson et al., 2015) and later updated in 2019 (Tay et al., 2019), recommends performing mpMRI at 3–6 months, 12–24 months, and 5 years post-treatment. In contrast to the follow-up scheme proposed by Muller et al., an earlier targeted biopsy of the treatment zone is recommended at 3-6 months after the first MRI.

A frequently encountered challenge with ablation therapies is how to define treatment failure or recurrent disease. Following ablation, particularly in focal ablations, residual prostatic tissue often remains, diminishing the reliability of PSA in follow-up assessments. Consequently, identifying recurrent disease post-ablation

is more complex compared to after RP or RT. Detecting and defining recurrence after ablation therapy typically necessitates a combination of PSA, imaging findings (MRI, CT, bone scan and/or PSMA-PET), and biopsies. Abovementioned expert consensus panel (Tay et al., 2019) defined treatment failure as follows: 1. Significant volume (≥ 0.2 mL or ≥ 7 mm in diameter) of Gleason ≥ 3+4 (GG 2) within the treated zone, 2. Development of any foci of clinically significant cancer requiring further therapy in the untreated zone.

2.3.4 Salvage therapy for recurrent PCa

In general, salvage therapy refers to a treatment administered when cancer fails to respond to or relapses after standard treatment. In the context of PCa, it typically involves efforts to eliminate local recurrence following the initial curative-intent treatment, where local refers to recurrence in the prostate (or prostate bed), seminal vesicles or pelvic lymph nodes. This thesis focuses on the local salvage therapies, management of metastatic disease is not covered.

2.3.4.1 Salvage therapy after primary surgery

Following RP, PSA levels should ideally drop to undetectable levels. However, in 5–20% of patients, PSA remains detectable or persists (defined as PSA values ≥ 0.1 ng/mL) after RP. Numerous studies indicate that persistent PSA is linked to more advanced disease and a poorer prognosis. Imaging has no established position for patients with persistent PSA; CT and bone scan typically offer no value when PSA levels are below 2 ng/mL, but PSMA-PET-CT may detect residual cancer or metastasis even with low PSA values, and thus guide treatment decisions. Current data suggests that patients with persistent PSA after RP might benefit from early aggressive multi-modal treatments (post-operative RT and/or ADT). Nonetheless, strong evidence supporting this approach is lacking. (Mottet et al., 2022)

There is some controversy over the definition of biochemical recurrence after RP; while any increase in PSA can be considered as BCR, a PSA level > 0.4 ng/mL is often seen as the cut-off value indicative of future metastasis. PSA velocity and doubling time are also typically calculated. The EAU classifies patients with BCR into two risk groups: low risk (PSA doubling time > 1 year and ISUP GG < 4) and high risk (PSA doubling time < 1 year or ISUP GG 4-5) patients. While evidence for imaging BCR is limited, a PSMA-PET-CT is recommended for PSA levels > 0.2 ng/mL if the results would impact subsequent treatment decisions, particularly for high-risk patients. For treating local recurrence post-RP, there's a strong recommendation for early salvage radiation therapy, even with a negative PSMA-PET. Additionally, high-risk patients with local recurrence should be offered

enzalutamide with or without ADT. For EAU Low-Risk patients, those with a life expectancy of less than ten years, or those unwilling to undergo salvage treatment, active surveillance might be considered, although evidence supporting this approach is not robust. (Mottet et al., 2022)

2.3.4.2 Salvage therapy after radiotherapy (radiorecurrent disease)

Despite the technological advancements in radiation therapy, up to half of men who undergo RT still experience biochemical recurrence (Mottet et al., 2022). Even when the recurrence remains localized to the prostate, the majority of patients receive systemic ADT, which is not curative and can entail many side effects (Agarwal et al., 2008; Saylor & Smith, 2013). Hence, there is a distinct need for an efficient treatment for localized radiorecurrent PCa that offers the potential for complete disease control and the postponement or even avoidance of the adverse effects associated with systemic therapies (Tran et al., 2014).

Various local salvage treatment methods for radiorecurrent PCa have been researched, including salvage prostatectomy (Chade et al., 2012), HIFU (Crouzet et al., 2017), cryoablation (Siddiqui et al., 2016), and brachytherapy (Tisseverasinghe & Crook, 2018). Preliminary studies have also been conducted on stereotactic reirradiation (Corkum et al., 2020) and IRE (Blazevski et al., 2023). Despite these many treatment options there is no clear guidelines on when to use local salvage treatment, and for which patients (Mottet et al., 2022).

Salvage prostatectomy, a complex procedure available at specialized centers for carefully chosen patients, is associated with a high rate of complications and an increased probability of negative functional outcomes. In a recent meta-analysis (Valle et al., 2021), the incidence of severe genitourinary (GU) and gastrointestinal (GI) toxicity after salvage RP were approximately 20% and 2%, respectively. In contrast, of the less invasive approaches salvage HIFU and cryotherapy exhibited nearly identical toxicity rates, while radiotherapeutic alternatives (including stereotactic reirradiation, LDR and HDR brachytherapy) presented significantly lower GU toxicity rates, ranging from 4% to 8%. The adjusted 5-year recurrence-free survival (RFS) rates varied from 50% following cryotherapy to 60% after HDR brachytherapy and stereotactic body radiotherapy, with no statistically significant differences observed among any of these modalities and salvage RP.

2.3.4.3 Salvage therapy after ablative therapies

Since ablative therapies have no established position on the primary treatment of PCa, there are consequently no strong guidelines or recommendations for managing

failure after ablation therapies. Nonetheless, the utilization of ablative therapies in PCa treatment has increased.

In a review article on salvage therapy following focal and whole-gland-intended PCa ablation treatments (Marra et al., 2019), only four retrospective studies with small patient cohorts (total n = 67) were identified, covering primary focal PCa treatment methods such as PDT, cryotherapy, HIFU, and FLA. The salvage methods used for biopsy-confirmed recurrences included cryotherapy in one study (n = 12) and RP in the other three.

There is considerably more literature with larger patient cohorts on salvage treatments after whole-gland-intended ablation therapies, mostly cryotherapy and HIFU. Possible salvage methods after whole-gland ablation therapy included repeat ablation, salvage RT and salvage RP.

In these studies, overall complications and both oncological and functional outcomes seemed acceptable and not significantly worse than those observed with primary PCa treatment. However, key limitations include the low quality of evidence and the lack of standardized criteria for ablation therapy, salvage treatment, and ablation therapy failure. Additional research with prospective controlled studies is required to validate these initial results.

2.4 Magnetic resonance imaging (MRI) of prostate

The initial concept of MR imaging was reported by Paul C. Lauterbur in the 1970s (Lauterbur, 1973), and first commercial MRI scanners were built in 1980s. Within the last two decades the amount of both MRI scanners and scans has dramatically increased. The primary advantage over traditional imaging modalities lies in its exceptional soft tissue contrast and the absence of ionizing radiation exposure for patients.

In medical MR imaging, the signal from the nuclei of hydrogen atoms (^{1}H) is employed for image generation. A hydrogen atom is composed of a nucleus containing a single proton and a single electron orbiting the nucleus. Hydrogen atoms are prevalent in water (H_2O) and fat molecules, with most soft tissues exhibiting a high water content. In addition to its positive charge, proton (hydrogen nucleus) possesses spin, implying rotation about its axis. A proton with spin exhibits two significant characteristics: 1. As a rotating mass, the proton possesses angular momentum, behaving like a spinning top that strives to maintain the spatial orientation of its rotation axis. 2. As a rotating mass with an electrical charge, the proton also carries a magnetic moment (B), acting as a small magnet. Consequently, the proton is influenced by external magnetic fields and electromagnetic waves. (Weishaupt et al., 2006)

In MRI, three distinct magnetic fields are utilized: the primary static field of the scanner (B_0), spatial encoding gradients, and the oscillating magnetic field (B_1) generated by the radiofrequency (RF) pulses. When protons encounter an external magnetic field, B_0, their magnetic moments, or spins, align with the field either in parallel or anti-parallel directions. Slightly more protons are aligned in the direction of B_0 creating a net magnetization vector (M_0) parallel to the main magnetic field. Not only do the magnetic moments align with the field, but they also undergo precession. The precession of nuclei occurs at a characteristic speed, known as the Larmor (or precession) frequency, which is proportional to the strength of the applied magnetic field. The Larmor frequency is computed using the equation: $\gamma_0 \cdot B_0$, where γ_0 represents the gyromagnetic ratio constant of the proton (42.58 MHz/T), and B_0 is the strength of the main magnetic field.

To detect the MR signal, it is necessary to incline the net magnetization vector into the transverse plane (90°) using an RF pulse that matches the Larmor frequency. This facilitates the absorption of energy by proton spins, a phenomenon known as excitation. Following excitation, the net magnetization promptly begins returning to the stable state (aligned with the B_0 field) through two independent simultaneous processes: T1 relaxation (longitudinal relaxation) and T2 relaxation (transverse relaxation), respectively. T1 relaxation time represents the recovery of longitudinal magnetization, while T2 relaxation represents the decay of transverse magnetization. T2 relaxation (spin-spin interaction) involves spins exchanging energy with each other instead of dissipating energy to their surroundings like T1 relaxation (spin-lattice interaction). The decrease in the MR signal due to T2 relaxation occurs within the first 100–300 ms, well before the complete recovery of longitudinal magnetization due to T1 relaxation (0.5–5 seconds). During transverse magnetization, the precession of protons acts like an electrical generator, inducing an alternating voltage matching the Larmor frequency in a receiver coil, which constitutes the MR signal. Subsequently, this signal is acquired and processed using sensitive receivers and computers to generate the MR image. (Weishaupt et al., 2006)

Different tissues have distinct T1 and T2 relaxation times, creating contrast in MR images. The interval at which the proton spins are excited is referred to as the repetition time (TR). The time at which the signal is sampled is referred to the echo time (TE). The interplay between the TR and TE times impacts which type of tissue contrast is being measured, known as image weighting. In T1-weighted (T1W) images, bright areas correspond to tissues with short T1 relaxation times, while dark areas represent tissues with long T1 relaxation times. T2-weighted (T2W) images show bright areas for tissues with long T2 relaxation times and dark areas for tissues with short T2 relaxation times. Proton density (PD) images derive contrast from the proton density of imaged tissues. TE defines the T2-weighting, with a higher TE leading to increased T2-weighting. TR influences T1-weighting, with T1-weighting

decreasing as TR increases. PD-weighting is achieved by minimizing T1 and T2 weightings, i.e. making TE short and TR long. MR images typically incorporate all these weightings, with primary weighting dictated by specific imaging parameters.

MR image formation relies on imaging sequences, involving specific applications of radiofrequency pulses and gradients for excitation, phase encoding, echo formation (i.e., MR signal), and signal collection. The commonly used sequences are spin-echo (SE) and gradient echo (GRE). By adjusting parameters like TE, TR, and flip angle, desired image contrast can be achieved in these MRI sequences. In the SE sequence, a 90° RF pulse followed by a 180° RF pulse generates an echo. The 180° refocusing pulse eliminates static magnetic field inhomogeneities. In contrast, the GRE sequence involves an RF pulse (typically below 90°), and the echo is formed with dephasing and rephrasing gradients in the frequency encoding direction. (Weishaupt et al., 2006)

2.4.1 T1- and T2-weighted (T1W- and T2W) imaging

The fundamentals on the formation of T1- and T2-weighted MR images are discussed above. PI-RADS steering committee recommends including both sequences in prostate MRI (Turkbey et al., 2019). T1W images should be acquired in axial plane, and they can be obtained with or without fat suppression using either SE or GRE sequences. T2W images should always be obtained in the axial plane and a minimum of one additional orthogonal plane (i.e., sagittal and/or coronal). T2W images are usually obtained with 2D fast spin (FSE) or turbo spin echo (TSE) sequences.

T1W sequence is included in prostate MRI protocols mainly due to the detection of hemorrhage and mucinous or high-protein content in prostate and seminal vesicles. Prior studies on brain hematomas have shown that the appearance of hemorrhage in MR imaging primarily depends on the age of hematoma. As the hematoma ages, hemoglobin undergoes various forms before red cell lysis and breakdown into ferritin and hemosiderin. Hemorrhage have been categorized into five stages: hyperacute (intracellular oxyhemoglobin, long T1 and T2), acute (intracellular deoxyhemoglobin, long T1, short T2), early subacute (intracellular methemoglobin, short T1 and T2), late subacute (extracellular methemoglobin, short T1, long T2), and chronic (ferritin and hemosiderin, signal loss, short T2) (Bradley, 1993). Due to strong paramagnetic effect of methemoglobin, in subacute phase hemorrhage is usually seen bright in T1W images. As the blood products dissolve and are absorbed in chronic phases, the T1 signal intensity gradually diminishes. However, in the case of the prostate, the stages of hemorrhage may present differently. This is attributed to the knowledge that prostate tissue produces citrate, serving both as a preservative in semen and an anticoagulant (Barrett et al., 2012; Rosenkrantz & Taneja, 2014). The anticoagulative effect of citrate can extend the

period of T1 brightness in prostate hemorrhage, observable even several months after prostate biopsies (White et al., 1995). Notably, cancerous tissue lacks citrate production, resulting in a phenomenon known as the "hemorrhage exclusion sign" (see **Figure 9)**. This sign manifests as the area of prostate cancer not appearing bright on T1 images, unlike the adjacent tissue with post-biopsy haemorrhage (Barrett et al., 2012). Consequently, according to PI-RADS guidelines it is not necessary to postpone MRI after biopsies (Turkbey et al., 2019).

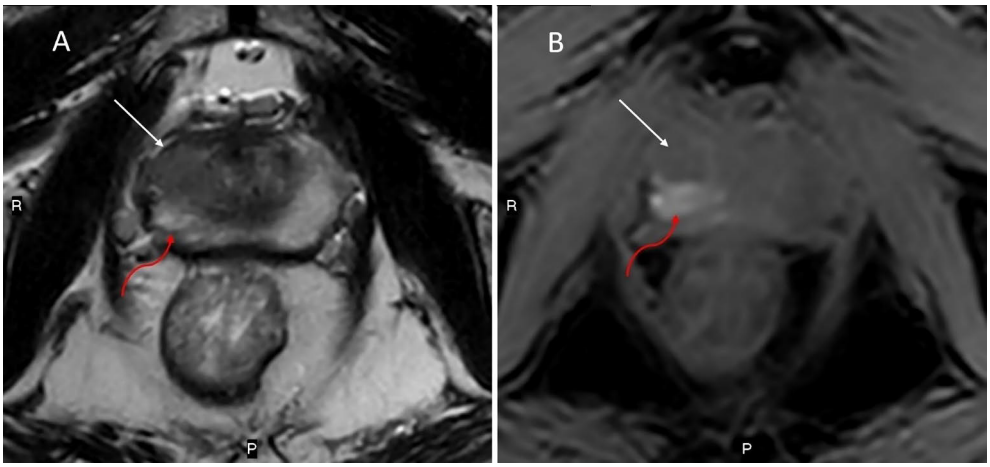

Figure 9. Patient example of the “hemorrhage exclusion sign”. T2W axial image (**A**) represents an anterior PI-RADS 5 lesion on the right PZ with marked T2 hypointensity (white arrow), with no signs of post-biopsy hemorrhage on the tumor area in T1W fat-saturated axial image (**B**). In contrast, posterior right PZ with no tumor (curved red arrow on image **A**), exhibits marked T1 hyperintensity indicating the presence of hemorrhage (curved red arrow on image **B**). (Images retrieved without identifiers from the PACS of Turku University Hospital)

T2W images serve multiple purposes, including the identification of prostatic zonal anatomy, assessment of gland abnormalities, and the evaluation of seminal vesicle invasion, extraprostatic extension (EPE), and nodal involvement. In the peripheral zone (PZ), clinically significant cancers on T2W images often manifest as round or ill-defined hypointense focal lesions. However, this appearance lacks specificity and can be observed in various conditions such as prostatitis, hemorrhage, glandular atrophy, benign hyperplasia, and biopsy-related scars. Transition zone (TZ) tumors on T2W images exhibit non-circumscribed homogeneous, moderately hypointense lesions with spiculated margins and lenticular shape. The presence of these features increases the likelihood of clinically significant TZ cancer. Identifying TZ cancers on T2W images can be challenging due to the composition of variable amounts of glandular (T2-hyperintense) and stromal (T2-hypointense) tissue, resulting in heterogeneous signal intensity. In areas where benign stromal elements predominate, clinically significant cancer may be either mimicked or obscured. (Turkbey et al., 2019)

2.4.2 Diffusion-weighted imaging (DWI)

Diffusion-weighted imaging captures the random movement of water molecules. DWI provides both qualitative and quantitative insights at the cellular level, offering information on tissue cellularity, cell membrane integrity, and microcirculation. Diffusion is inversely correlated with cellularity and cell membrane integrity. Tissues with high cellularity, such as tumors, abscesses, and cytotoxic edema, exhibit restricted diffusion. Conversely, tissues with low cellularity or disrupted cell membranes, like cysts and necrotic tissues, show relatively free diffusion. Intravascular water molecules, with a larger diffusion distance, contribute more to the DWI signal than water molecules in extracellular and intracellular spaces. Consequently, tumors with high vascularity exhibit higher DWI signal. (Feuerlein et al., 2009; Morani et al., 2013)

DWI relies on T2-weighted imaging, employing a pair of bipolar gradients around the 180° refocusing pulse in a standard T2-weighted sequence. In static tissue, the induced phase shift by the first diffusion gradient is counteracted by the second, resulting in minimal signal intensity change. However, moving water molecules, un-rephased due to motion, experience signal loss, enabling the detection of water motion as reduced signal intensity. (Koh & Collins, 2007)

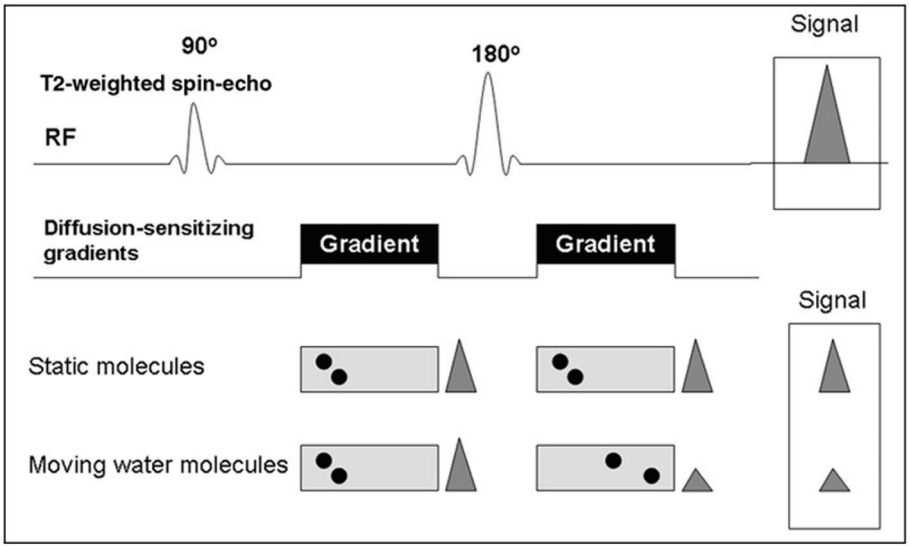

Figure 10. Basic concept of DWI. Utilizing symmetric diffusion-sensitizing gradients around the 180° refocusing pulse, stationary molecules remain unaffected, preserving the measured signal intensity (restricted diffusion). On the contrary, moving water molecules capture phase information from the first gradient, which is incompletely rephased by the second gradient, resulting in signal loss (free diffusion). (Koh & Collins, 2007)

The sensitivity of DWI to water motion is determined by different diffusion weightings also known as the b values (s/mm^2), altered by gradient parameters. For meaningful interpretation, DWI should use at least two b values: b = 0 s/mm^2 and b = 100 to 1000 s/mm^2. The apparent diffusion coefficient (ADC) map is a quantitative representation of the diffusion characteristics of tissues observed in DWI with different b values. By plotting the logarithm of the relative signal intensity of the tissue on the y-axis against the b values on the x-axis, a line can be fitted through the plots. The slope of the line describes the ADC. Notably, incorporating more b values enhances the fitting, reducing the error in ADC calculation. On the ADC map, tissues exhibiting restricted diffusion appear dark, while tissues with free diffusion appear bright. (Koh & Collins, 2007; Morani et al., 2013)

DWI is an essential part of prostate MRI, especially in the assessment of peripheral zone lesions. The recommended technical aspect of DWI, include free-breathing SE echo planar imaging (EPI) sequence combined with fat saturation. Because higher b values are more sensitive to diffusion effects and optimal for background signal suppression, the PI-RADS committee recommends incorporating a b value of at least 1400 s/mm² to enhance resolution between benign and malignant prostate tissue. Numerical ADC values for lesions can be readily measured using the region of interest (ROI) tool on workstations. However, since ADC calculations are influenced by choice of b-values and have been inconsistent across vendors, the visual assessment of ADC maps is often used as primary method. (Turkbey et al., 2019)

2.4.3 Contrast-enhanced imaging

In cases where endogenous contrast differences are insufficient to highlight specific pathologies or features of interest, exogenous contrast agents may be necessary to enhance signal intensity. While various MRI contrast agents are available, the most common are gadolinium-based contrast agents (GBCA). Administered through injection into the veins, GBCA swiftly perfuse the entire body, diffusing rapidly into the extracellular space, and is eventually filtered out by the kidneys. GBCA function by shortening the T1 relaxation time of hydrogen protons in their proximity, making the use most effective when combined with T1-weighted imaging. (Lin & Brown, 2007)

In prostate MRI, contrast-enhanced imaging is secondary to more crucial T2- and diffusion-weighted sequences. Dynamic contrast-enhanced (DCE) rapid T1W gradient echo scans with fat saturation should be obtained before, during and after intravenous administration of GBCA. Recommended temporal resolution should be ≤ 15 s, and total observation time ≥ 2 min. (Turkbey et al., 2019)

Similar to various malignancies, PCa often exhibit early enhancement compared to normal tissue following the bolus injection of GBCA. However, the kinetics of PCa enhancement are markedly diverse and can display considerable heterogeneity, with the possibility of benign conditions also showing early enhancement. Thus, it is important to note that enhancement alone is not conclusive evidence of clinically significant PCa, and the absence of early enhancement does not rule out cancer. The value of positive DCE is upgrading a peripheral zone lesion from PI-RADS 3 to PI-RADS 4 category. DCE is considered positive when enhancement is focal and occurs earlier or simultaneously with the enhancement of adjacent normal prostatic tissues, typically corresponding to a suspicious finding on T2W- and/or DW imaging. While DCE can be quantitatively measured using various commercial software programs, the enhancement characteristics of PCa exhibit significant heterogeneity. Currently, there is limited evidence in the literature supporting the use of specific curve types or pharmacokinetic values. Therefore, the PI-RADS steering committee considers visual assessment of DCE sufficient. (Turkbey et al., 2019)

2.4.4 Thermometry

Real-time monitoring of the heating pattern in TULSA is based on MR thermometry, which offers non-invasive temperature measurement in the treatment area. While various approaches have been proposed, the most common is the proton resonance frequency shift (PRFS) technique (Ishihara et al., 1995). When tissues abundant in water molecules undergo heating or cooling, the consequent temperature change influences the hydrogen bonds. With an increase in temperature, the hydrogen bonds between water molecules stretch, bend, and eventually break, resulting in a lower local magnetic field and a lower proton resonance frequency (Muller & Reiter, 1965; Rieke & Butts Pauly, 2008). The chemical shift change due to temperature changes is linear across a wide range of temperatures, varying by α, which has been experimentally determined to be -0.01 parts per million (ppm)/°C (Rieke & Butts Pauly, 2008). The temperature change is calculated by measuring the difference in phase between two images and is expressed below:

$$\Delta T = \frac{\varphi(T) - \varphi(T_0)}{\gamma \alpha B_0 TE} \qquad (2)$$

where $\boldsymbol{\varphi(T)}$ is the phase in the current image, $\boldsymbol{\varphi(T_0)}$ is the phase of a baseline image at a known temperature, $\boldsymbol{\gamma}$ is the gyromagnetic ratio, $\boldsymbol{\alpha}$ is the PRF change coefficient, $\mathbf{B_0}$ is the magnetic field strength, and **TE** is the echo time (Rieke & Butts Pauly, 2008).

To conduct PRFS thermometry, a baseline phase image is obtained before the heating process at each voxel within the imaging volume. As the ablation begins, the

temperature alteration is assessed by gauging the phase change at all voxel locations in the image. Due to this approach, PRFS thermometry does not provide absolute temperature measurements, but exclusively computes relative temperature changes (Rieke & Butts Pauly, 2008). The initial body temperature is usually measured just before the onset of heating using an MR-compatible temperature probe. To achieve nearly real-time monitoring, thermometry is commonly performed using an EPI sequence, known for its ability to quickly capture extensive scan volumes (Stafford et al., 2004; Weidensteiner et al., 2003).

PRFS thermometry can achieve a temperature accuracy of less than ± 1 °C under optimal conditions (Quesson et al., 2000). However, it is compromised by various limitations. Firstly, it is sensitive to patient motion since it relies on a reference image. Additionally, susceptibility to magnetic drift is a concern, especially during extended scan times. While α has been shown to be largely tissue-independent, this does not apply to fatty tissue, which lacks the same hydrogen bonds as water-rich tissue. This leads to difficulties in assessing temperature changes in fatty tissue. Also, partial volume effects may arise when a voxel contains both fatty and regular biological tissue, leading to the common use of fat suppression during thermometry. Lastly, being a reference-based temperature technique, thermometry outcomes can be influenced by errors in the baseline temperature. (Rieke & Butts Pauly, 2008)

In addition to thermometry-specific limitations, there can be challenges related to well-known MRI artifacts, with susceptibility artifacts being particularly notable. Magnetic susceptibility, a property of matter indicating its behaviour in a magnetic field, can be diamagnetic (weakens the field) or paramagnetic (strengthens the field). Nearly all biological tissues exhibit weak diamagnetism, whereas ferrous materials like nickel and iron display high paramagnetism. Gold is slightly diamagnetic, and air has a magnetic susceptibility close to zero. Local variations in magnetic field strength result in susceptibility changes, causing two main image artifacts: geometric distortion and overall signal loss. This occurs because local susceptibility changes disrupt the linearity of the frequency encoding magnet (Taber et al., 1998). The most pronounced effects come from ferrous objects; however, susceptibility differences between neighbouring tissues, such as air interfaces, can also lead to dropout areas. Regarding radiorecurrent PCa, susceptibility effects caused by fiducial markers can impede the clear visualization of prostate tissue around the markers (Jonsson et al., 2012; Osman et al., 2019).

2.4.5 MRI after thermal ablation

Multiparametric MRI is recommended in the assessment of prostate after thermal ablation (Giganti et al., 2023; Light et al., 2024; Muller et al., 2015; Tay et al., 2019).

The primary aim in the MRI surveillance is to detect the residual tumor tissue on the treatment area and local recurrence outside the treatment area. Secondary, MRI provides information on the possible treatment complications, such as rectal or symphysis joint fistulas, abscess formation and osteitis.

In addition to complications, prior studies on HIFU, laser ablation and cryotherapy have reported various natural, uncomplicated changes in the prostate and surrounding tissues after thermal ablation, with the most notable finding being non-perfused area representing the desired necrotic tissue. Expected acute findings include edema in the prostatic and surrounding tissues resulting in increased prostate volume, heterogeneous T2 signal, bright T1 signal areas likely representing hemorrhage, obscuring of prostatic zonal anatomy, and a non-perfused area with a surrounding rim of enhancement. Within six months post-ablation, there is a reduction in prostate volume and non-perfused volumes, gradual disappearance of the rim of enhancement, development of T2 hypointense scar tissue in the prostatic and periprostatic tissues, and the appearance of a TURP-like cavity or cyst formation. At 12 months, a significant decrease in both prostate and non-perfused volumes have been reported. **Figure 11** represents a patient example of MRI changes after focal HIFU. (Bonekamp et al., 2019; Ghafoor et al., 2020; Hötker et al., 2019; Kirkham et al., 2008; Patel et al., 2018; Rouvière et al., 2001).

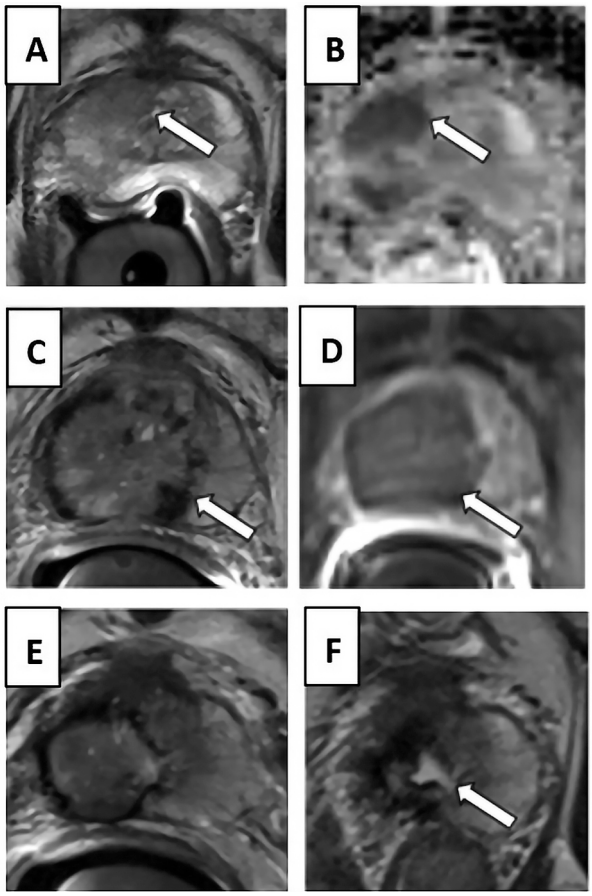

Figure 11. A patient example of post-HIFU MRI changes. In upper row baseline MRI images with a tumor focus with T2 hypointensity (**A**) and diffusion restriction on ADC map (**B**). In middle row a one-week post-HIFU MRI with heterogenous signal and edema of the ablation zone on T2W image (**C**) with low-signal peripheral hemosiderin deposition, and T1 fs contrast-enhanced image (**D**) showing non-perfused treatment area with surrounding rim of enhancement. In lower row T2W images at 6 months (**E**) and 18 months (**F**) post-HIFU showing gradual disappearance of the prostatic tissue from the treatment zone, T2 dark fibrosis, and TURP-like cavity formation (**F**). (Modified from (Ghafoor et al., 2020))

There is no widely adopted MRI reporting system for assessing tumor residual or recurrence after ablation treatments. However, in 2023 Giganti et al. proposed a new 3-grade scoring system called PI-FAB, the Prostate Imaging after Focal Ablation (Giganti et al., 2023). Since fibrosis with low T2 signal is often present after ablation therapies, the dominant sequences in the tumor recurrence assessment are dynamic contrast-enhanced and diffusion-weighted sequences. PI-FAB score 1 likely represents fibrosis, score 2 is equivocal, and score 3 is highly suspicious for residual or recurrent disease. The scoring system offers clinical management guidance based on the PI-FAB score. **Figure 12** outlines the concept of PI-FAB.

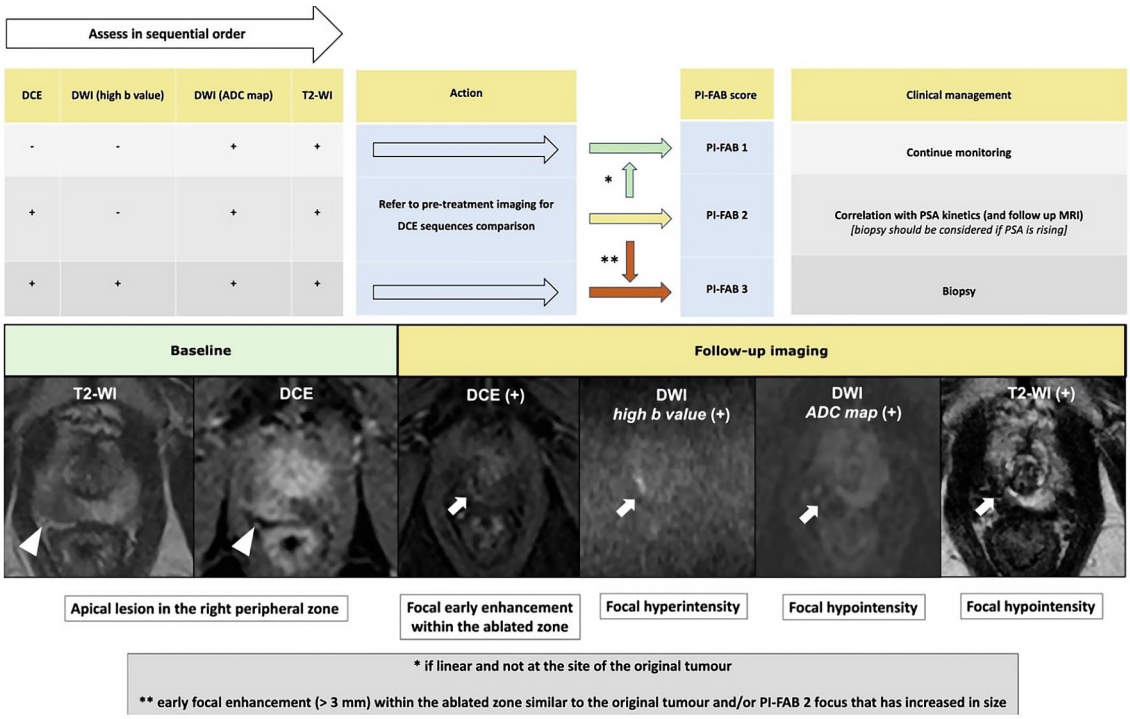

Figure 12. PI-FAB scoring system. (Adapted from (Giganti et al., 2023))

Most recently, another classification system for MRI acquisition, interpretation, and reporting after focal therapy, called TARGET, was introduced as a set of consensus recommendations from an international expert panel (Light et al., 2024). In the TARGET system, prostate tissue outside the ablation area is assessed and reported according to the PI-RADS classification, while the TARGET criteria are specifically used to evaluate the ablation area and its surroundings. The TARGET classification utilizes a 5-point scoring system that incorporates a major DCE sequence and joint minor diffusion-weighted imaging and T2-weighted sequences. Among the findings, focal nodular strong early enhancement on the DCE sequence was identified as the most suspicious imaging feature.

The PI-FAB and TARGET classification systems are specifically designed for post-treatment assessment following primary focal treatment of the prostate and are not suitable for use after whole-gland or salvage treatments.

3 Aims

Following ablation treatments, there is residual untreated prostate tissue alongside the treated area, diminishing the utility of PSA in the follow-up. Therefore, imaging is even more important in the follow-up after ablation therapies. Previous knowledge on MRI findings after TULSA treatment, and factors affecting the treatment outcome is limited. Subacute MRI findings after TULSA treatment correlated with histology, or the effect of radiotherapy fiducial markers on the outcome of ultrasound ablation have not previously been reported. There is also limited prior knowledge on the evolution of necrotic tissue after prostate ablation treatments, none for the radiorecurrent PCa patients. The specific aims of this doctoral thesis were:

I. To evaluate acute and subacute MRI findings after TULSA treatment in a treat-and-resect study setting.

II. To evaluate safety, functional, and early-stage oncological outcomes for patients with gold fiducial markers undergoing salvage MRI-guided TULSA for radiorecurrent PCa.

III. To characterize the NPV evolution for three treatment groups undergoing TULSA ablation, including benign prostatic hyperplasia, primary PCa, and radiorecurrent PCa.

4 Materials and Methods

4.1 Study population

The study cohorts for the three sub-studies of this doctoral thesis were assembled from two prospective registered studies, HIFU-PRO (NCT03350529) and PRO-TULSA-PC (NCT03814252). All TULSA treatments and data acquisition within the studies occurred at Turku University Hospital between 2017 and 2021. In each of the sub-studies (I, II, and III), all participants provided written informed consent, local ethics approval was obtained, and the studies were conducted in accordance with the principles outlined in the Declaration of Helsinki.

Study I was a prospective clinical phase 1 trial with a treat-and-resect study setting (HIFU-PRO, treat-and-resect arm). Between August 2017 and May 2018, six men with newly diagnosed MRI-visible and biopsy-proven csPCa were enrolled and completed the study. A total of eight PI-RADS 3-5 lesions were identified and targeted with TULSA.

In Study II data were originally acquired as part of a phase 1 study (HIFU-PRO, salvage arm). We retrospectively identified eight patients with gold intraprostatic fiducial markers who received salvage TULSA (sTULSA) for radiorecurrent PCa between November 2017 and November 2020. Among these eight patients, a total of 18 markers within the planned treatment volume were identified. The safety control cohort included 13 sTULSA patients without markers in the treatment zone.

In Study III all imaging data were acquired as part of phase 1–2 study of TULSA therapy for BPH and radiorecurrent PCa patients (HIFU-PRO, BPH and salvage arms), and phase 2 study for primary PCa patients (PRO-TULSA-PC). We retrospectively identified 97 consecutive patients who received TULSA between April 2018 and November 2021. A total of 89 patients (21 BPH, 28 radiorecurrent PCa, and 40 primary PCa) were eventually included in the study.

4.2 Study design

HIFU-PRO study consisted of four separate arms as shown in **Table 3**. In this doctoral thesis patient data from palliation arm were not used.

Table 3. Details of HIFU-PRO study.

Study arm	n	Study description	Essential inclusion criteria	Essential exclusion criteria
Treat-and-resect	6	lesion-targeted TULSA for all MRI-visible PI-RADS 3-5 lesions; MRI follow-up immediately, and at 1 and 3 weeks post-TULSA; prostatectomy 3 weeks post-TULSA; histopathological analysis of prostatectomy specimen	patients with newly-diagnosed MRI-visible biopsy-concordant localized csPCa scheduled for RALP	metastatic disease; contraindications for MRI
Palliation*	10	TULSA targeted to main prostatic malignant tumor squeezing and/or invading the prostatic urethra and/or bladder neck; MRI follow-up immediately, and at 1 week and 12 months post-TULSA	patients in need of palliative surgical intervention due to local symptoms/complications caused by advanced PCa	life-expectancy less than 3 months; contraindications for MRI
Salvage	40	either lesion-targeted TULSA for MRI-visible, biopsy-proven radiorecurrent lesions or whole-gland TULSA in case of extensive organ-confined recurrence; MRI follow-up at 3 and 12 months post-TULSA; biopsies and PSMA-PET-CT at 12 months post-TULSA	patients with biopsy-proven localized PCa recurrence after radiotherapy	evidence of extraprostatic disease on restaging including seminal vesicle invasion; contraindications for MRI
BPH	30	TULSA targeted to adenomas of the prostate, encompassing transition zone between bladder neck and verumontanum	patients planned for surgical procedure due to benign prostatic hyperplasia	suspicion of cancer on baseline MRI; contraindications for MRI

* not included in this doctoral thesis

PRO-TULSA-PC was a phase 2 study, in which patients with MRI-visible biopsy-concordant localized csPCa were treated with TULSA.

Following treatment, in addition to clinical and safety assessments, MRI follow-up was conducted immediately after, as well as at 6 and 12 months post-TULSA. Prostate biopsies were performed at 12 months. Essential exclusion criteria included contraindications for MRI, and tumor location further than 30 mm or within 3 mm of the prostatic urethra.

The primary emphasis of this doctoral thesis was on imaging findings. Nevertheless, in Study II, clinical outcomes and safety measures were also assessed.

4.3 Therapeutic device and treatment strategy

In each of the three sub-studies in this doctoral thesis, the therapeutic device utilized was TULSA (TULSA-PRO, Profound Medical Inc., Mississauga, Canada), which was integrated into a 3T MR machine (Philips, Ingenia, Best, Netherlands). Detailed description of the TULSA method is available in the Review of the Literature -section.

In the treat-and-resect Study I, the treatment plan targeted ablation of all MRI-visible biopsy-concordant PCa lesions. The ablation strategy aimed to cover the lesions with a 5 mm overlap, reaching the prostate capsule whenever feasible, achieved through a single sonication sweep. In this treat-and-resect study, it was essential to mitigate any potential adverse effects on genitourinary function associated with the study intervention before nerve-sparing RALP. Consequently, safety margins of up to 3 mm were employed around the neurovascular bundles (NVB), irrespective of the tumor's size. A patient example of lesion-targeted treatment planning is provided in **Figure 13**.

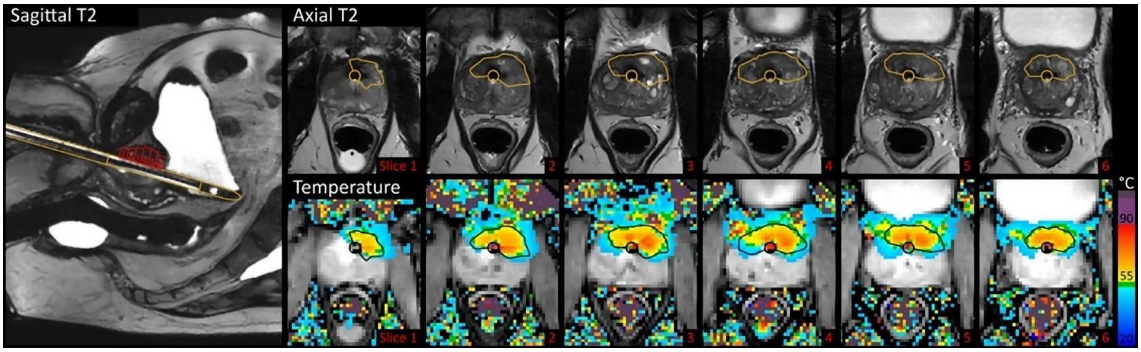

Figure 13. Illustrative patient example of treatment planning and the maximum temperature map post-treatment. Patient had an anterior PI-RADS 5 lesion. (Anttinen et al., 2019)

Treatment strategy for the radiorecurrent PCa patients in Study II was customized depending on patient characteristics. Two patients in the marker cohort underwent partial ablation, while six underwent whole-gland ablation. In the safety control cohort, seven patients underwent partial ablation and six underwent whole-gland ablation. At least two sonication sweeps of the targeted area were performed to ensure complete thermal coagulation.

In Study III, radiorecurrent PCa patients were treated as mentioned above, including both partial (n = 9) and whole-gland (n = 19) treatments. BPH patients, depending on prostate size, received transition zone ablation, from either apex or midgland to the base. Primary PCa cohort included both partial (n = 31) and whole-gland (n = 9) treatments. At least two heating sweeps of the targeted area were performed for all patient groups to ensure complete thermal coagulation. The only exception was the last 11 BPH study patients receiving only one heating sweep.

4.4 Imaging protocols

Most patients in each sub-study underwent imaging with a 3T MRI scanner (Philips, Ingenia, Best, Netherlands), and the specifics of the TULSA MRI protocols can be found in **Table 4**. A small portion of patients had their baseline and follow-up MRIs conducted outside our center, utilizing either bi- or multiparametric sequences. At Turku University Hospital, biparametric prostate MRI is the preferred standard protocol (Jambor et al., 2019), and it was also accepted as the baseline MRI for TULSA patients. The intravenous contrast media used in mpMRI protocols was gadoterate meglumine (Dotarem, Guerbet, Villepinte, France).

Table 4. TULSA MRI sequence specifics.

Joint sequences for pre- and post-TULSA	TR, ms	TE, ms	Flip angle	FOV, mm	Slice thickness, mm	TSE/TFE/EPI factor	SENSE (phase, slice)	Sequence details	Scan time (min:s)
T2w TSE ax	4375	95	90	220 x 220	3	17	1,5		3:04
T2w TSE cor	3772	90	90	220 x 220	3	19	1,5		3:02
T2w TSE sag	4844	95	90	240 x 240	3	28	2		3:09
3D T1w fs TFE ax	5,9	2,9	7	255 x 450	1	80	2; 1	Thrive, SPAIR	2:56
3D T1w fs TFE ax dyn + C	2,9	1,31	10	270 x 347	3	19	2,5; 1,3	Thrive, SPAIR	4:51
3D T1w fs TFE ax +C	5,9	2,9	7	255 x 450	1	80	2; 1	Thrive, SPAIR	2:56

DWI and ADC mapping (see below)

Specific sequences for pre-TULSA	TR, ms	TE, ms	Flip angle	FOV, mm	Slice thickness, mm	TSE/TFE/EPI factor	SENSE (phase, slice)	Sequence details	Scan time (min:s)
Thermometry EPI ax	109	5	12	256 x 256	4,6	11	1	T1, SPAIR	1:03
T2 relaxation time mapping	2800	12-192	90	230 x 182	5	16			3:05
Specific sequences for post-TULSA	**TR, ms**	**TE, ms**	**Flip angle**	**FOV, mm**	**Slice thickness, mm**	**TSE/TFE/EPI factor**	**SENSE (phase, slice)**	**Sequence details**	**Scan time (min:s)**
T2w fs TSE ax	4269	80	90	300 x 300	4	19	1,5	SPAIR	2:59
T1w fs TSE ax + C	496	8	90	180 x 180	3	5	0	SPIR	2:31
Sequences immediately after TULSA treatment	**TR, ms**	**TE, ms**	**Flip angle**	**FOV, mm**	**Slice thickness, mm**	**TSE/TFE/EPI factor**	**SENSE (phase, slice)**	**Sequence details**	**Scan time (min:s)**
T2w TSE ax	2732	110	90	256 x 256	3	17	0		3:28
3D T1w fs TFE ax	5,9	2,9	7	255 x 450	1	80	2; 1	Thrive, SPAIR	2:56
3D T1w fs TFE ax dyn + C	3	1,36	10	270 x 347	3	19	2,5; 1,3	SPAIR	4:55
3D T1w fs TFE ax +C	5,9	2,9	7	255 x 450	1	80	2; 1	Thrive, SPAIR	2:56
T1w fs TSE ax + C	496	8	90	180 x 180	3	5	0	SPIR	2:31

DWI and ADC mapping (see below)

Diffusion weighted sequence parameters

Sequence	TR, ms	TE, ms	Flip angle	FOV, mm	Slice thickness, mm	EPI factor	SENSE (phase)	Sequence details	Scan time (min:s)
DWI 500 ax	4894	45	90	250 x 250	3	75	2	b-factors 0, 100, 200, 350, 500; SPAIR	4:19
DWI 1000 trace ax	4195	78	90	375 x 290	5	47	2	b-factors 0, 100, 1000; SPIR	1:37
DWI 1500 ax	3180	56	90	250 x 250	5	75	2	b-factors 0, 1500; SPAIR	1:07
DWI 2000 ax	3420	58	90	250 x 250	5	75	2	b-factors 0, 2000; SPAIR	1:12
DWI 2500 ax	4206	62	90	250 x 250	5	75	2	b-factors 0, 2500; SPAIR	1:28

In Study II, radiorecurrent PCa patients had also 18^{F}-PSMA-PET-CT at baseline and 12 months post-TULSA. Images were obtained and analysed at Turku University Hospital. **Table 5** provides the details of the PSMA-PET-CT.

Table 5. Specifics of the 18^{F}-PSMA-PET-CT scan.

Tracer	Injection	PET-CT scanner	CT specifics	PET spesifics	Image reconstruction	Final spatial resolution
^{18}F-PSMA-1007	263±27 MBq (range 205-355); scan acquired 60 min post-injection	Discovery MI	128-slice CT; noise index 30, automatic 3D current modulation, 10-120 mAs and 120 kVp	3D PET device; FOV 70 cm in diameter and 20 cm in axial length; from vertex to mid-thigh (6 bed positions, 2 min/bed)	sinogram correction for deadtime, decay and photon attenuation; 256x256 matrix; Bayesian penalized likelihood reconstruction with β 500	< 5 mm

4.5 Image analysis

Study I

Several parameters were measured from MR images, including prostate volume, NPV, ADC values, hemorrhage volumes, T1- and T2 signal intensity ratios (SIR).

- Prostate volumes were measured by manually contouring prostate boundaries on T2W axial images (3 mm slice thickness), and calculated by AW Server volume rendering tool (AW Server 3.2, GE Healthcare, Chicago, Illinois, United States). Baseline, as well as 1- and 3-week post-TULSA volumes were assessed.
- NPV was defined and manually contoured on 3D T1W fat-saturated contrast-enhanced images (slice thickness 1 mm) as the non-enhancing area within the surrounding rim of enhancement, and calculated by AW server volume rendering tool. NPVs immediately, 1- and 3 weeks post-TULSA were assessed. Patient example of NPV volume measurement can be seen in **Figure 14**.
- ADC values were measured from ADC maps obtained from high b-value DW imaging (b-value = 1500 s/mm^2). A region of interest (ROI) of 0.2 cm^2 was drawn in the lowest signal in the lesion area (Carestream PACS Version

12.1.5.5151., Carestream Health Inc., Rochester, New York, United States), with a total of eight lesions assessed. A reference ROI was drawn in a homogenous region in prostate outside the treatment area. Baseline, as well as 1- and 3-week post-TULSA ADC values were assessed.

- MRI signal of hemorrhage within the NPV was assessed. T1 signal intensity (SI) was measured using 3D T1W fat-saturated images (Carestream PACS). A ROI of 0.2 cm^2 was drawn covering the area of highest intensity within the NPV and a reference ROI was drawn on the same slice in a contralateral non-hemorrhagic area of the prostate. The T1 SIR was calculated by dividing the SI in the hemorrhagic area by the SI in a non-hemorrhagic area of the prostate. The T2 SIR was measured like the T1 SIR, except that the hemorrhagic area SI was measured in the most T2 hypointense area within the NPV. Hemorrhage volumes were measured using the AW Server volume rendering tool by manually contouring regions of T1 hyperintensity in the treatment area. Values were assessed at 1- and 3 weeks post-TULSA.

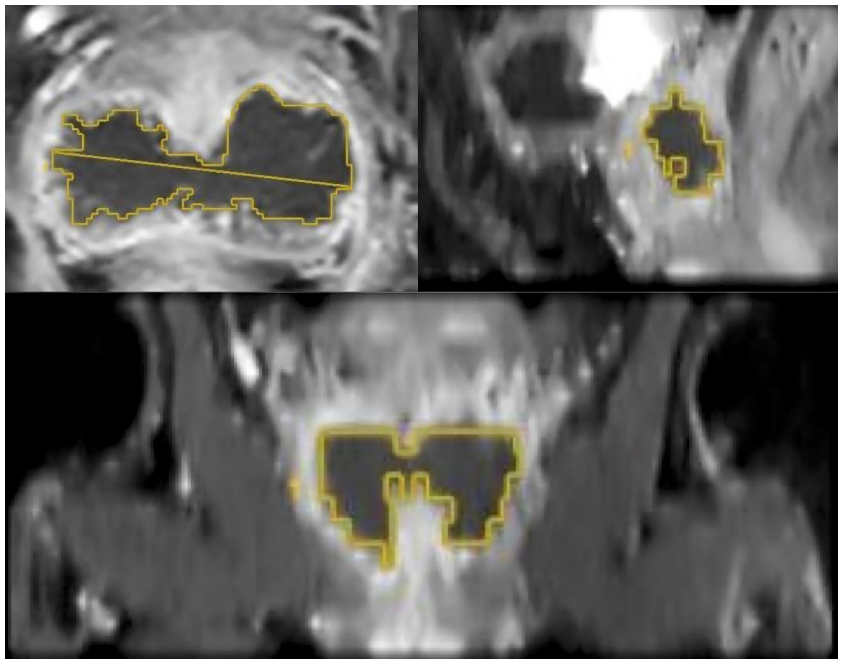

Figure 14. NPV measured using the AW Server volume rendering tool at 3 weeks post-TULSA. (Anttinen et al., 2019)

Study II

This sub-study included study cohort (n = 8) with fiducial markers, and a safety control cohort (n = 13) without fiducial markers. Following measurements were made for the study cohort:

- Thermal dose coverage was assessed by quantifying the linear targeting accuracy within prostate regions, with and without markers. To determine the linear targeting accuracy, the isodose boundary was initially calculated based on the final cumulative thermal dose map. This boundary was identified by determining the distance at which the thermal dose transitioned from above 240 cumulative equivalent minutes (CEM) to below 240 CEM. This computation was conducted with interpolated one-degree angular increments and a step size of 0.2 mm for all active ultrasound elements utilized during therapy. Subsequently, the isodose boundary was directly compared to the target boundary at each angular degree. Moreover, the linear targeting accuracy could be computed for any arbitrary angular region and slice. **Figure 15** illustrates the methodology used to measure targeting accuracy in a specific sub-region where marker was present.

- Prostate volumes and NPVs were measured using the AW Server volume rendering tool, employing the same methodology as outlined in study I. The only difference was the utilization of a 3 mm slice thickness for NPV contouring. Baseline prostate volumes were measured, along with assessments at 3 and 12 months following TULSA treatment, while NPVs were evaluated immediately after treatment, as well as at 3 and 12 months post-TULSA.

- Any remaining enhancing tissue situated behind the marker, suggesting marker-induced undertreatment, was measured. To ascertain the quantity of viable tissue, 3D T1W fat-saturated contrast-enhanced images were employed. A line was drawn originating from the centre of the urethra, extending outward through the marker, and reaching the border of the non-enhancing rim. The disparity between this line's termination point and the prostate capsule along the same line-of-sight was documented. Measurements were appraised immediately after, as well as at 3 and 12 months following TULSA treatment.

- At baseline, 18F-PSMA-PET-CT was conducted to identify local recurrence following radiation therapy and to rule out metastatic disease. A follow-up examination was performed at 12 months post-TULSA. Visual evaluation and

semi-quantitative analysis involved measuring the maximum standard uptake values (SUVmax) of any suspicious lesions.

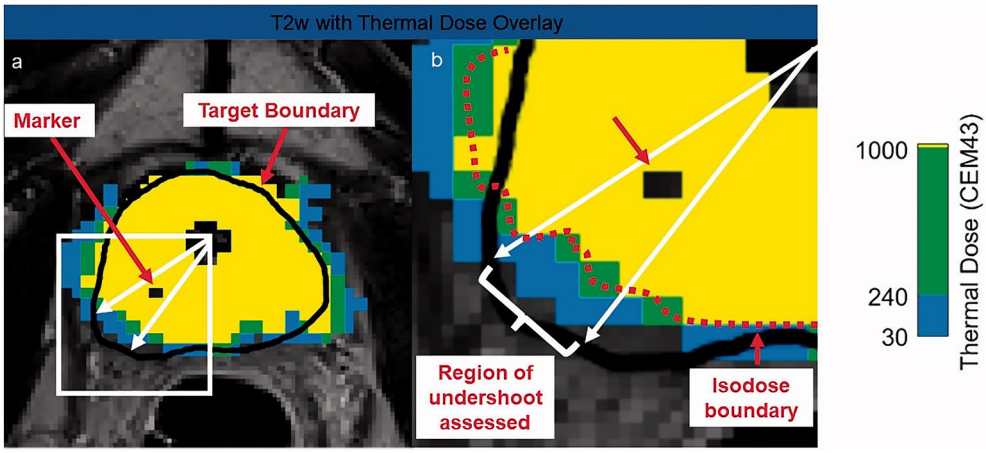

Figure 15. A patient example of thermal dose undershoot behind a fiducial marker. Thermal undershoot is defined as any angular region where isodose boundary (red dotted line) does not reach the target boundary (black line). (Wright et al., 2021)

Study III

This sub-study comprised three distinct patient cohorts: BPH, primary PCa, and radiorecurrent PCa. Prostate volumes and NPVs were measured using the same methodology described in previous studies (I and II). Each group underwent baseline and 12-month post-TULSA MRI examinations. Additionally, the BPH and radiorecurrent PCa cohorts received MRI evaluations at 3 months post-TULSA, while the primary PCa group was assessed at 6 months. Prostate volumes were measured at each of these time points, and NPVs were assessed immediately after treatment and at every subsequent MRI follow-up.

4.6 Treatment safety and efficacy assessment

Safety

Safety was monitored for all patients included in Study II, both in the fiducial marker patient cohort and control group (without fiducial markers). Patients were followed up to one year.

Adverse events (AE) were recorded according to the Clavien-Dindo Classification of Surgical Complications, which ranges from 1 to 5, with grades ≥ 3 regarded as severe AEs

Functional questionnaires included:

- Expanded Prostate Cancer Index (EPIC)-26: range 0–100 points, the higher the score the better the quality of health-related quality of life
- International Prostate Symptom Score (IPSS): 0–7 mild, 8–19 moderate, 20–35 severe symptoms
- IPSS Quality of life (QoL): range 0–6, with a higher score indicating a lower QoL
- International Index of Erectile Function (IIEF-5): 0–4 no sexual activity or extremely severe, 5–7 severe, 8–11 moderate, 12–16 mild to moderate, 17–21 mild, and 22–25 no erectile dysfunction

Questionnaire results were analysed at baseline and at 3 and 12 months post-TULSA.

Early-stage efficacy

To assess the early-stage efficacy of TULSA in the target group of Study II, PSA levels, imaging findings, and histopathology were employed. PSA measurements were analysed at baseline, and at 3 and 12 months post-TULSA. MR imaging was carried out immediately following treatment, with subsequent scans at 3 and 12 months post-TULSA. Furthermore, at 12 months, PSMA-PET-CT scans using the 18F-PSMA-1007-labeled tracer were conducted, where tumor uptake was evaluated by monitoring the SUVmax.

Once all imaging was completed at the 12-month follow-up, ultrasound-guided transrectal cognitive-targeted biopsies were obtained to confirm the histopathological extent of disease. The number of cores taken depended on the size of the gland and whether any regions in MR or PSMA-PET-CT imaging were deemed suspicious for local recurrence.

4.7 Statistical analysis

In all sub-studies JMP software (SAS Institute Inc., Cary, NC, USA) was used for statistical analysis. Normality assumptions were confirmed using a normal quantile plot, boxplot, kurtosis/skewness evaluation, and Shapiro–Wilk test.

In Study I, consisting of merely six patients, no complex statistical comparative analysis was conducted. Data conforming to normal distribution were presented as mean values.

In Study II, normally distributed data were reported as mean, and the skewed distribution data as median values. Significance testing was performed using a two-tailed t-test. P values of ≤ 0.05 were considered statistically significant.

In Study III, normally distributed data were reported as mean, and the skewed distribution data as median values. Significance testing between two variables was performed using a two-sample t-test for normally distributed variables and Wilcoxon rank sum test as a nonparametric test. Levene's test was used to evaluate the assumption of equality of variances. Kruskal-Wallis test was used for multiple comparisons between all groups for the relative change of NPV at 12 months. P values of ≤ 0.05 were considered statistically significant.

5 Results

5.1 Acute and subacute MRI findings after TULSA (Study I)

5.1.1 Evolution of prostate volume and NPV

Prostate volume measurements showed that the average volume increase was 29% between baseline and 1-week post-TULSA imaging. Between 1- and 3-week MRI controls volumes decreased, and by three weeks the mean volumes approached baseline levels (+5%).

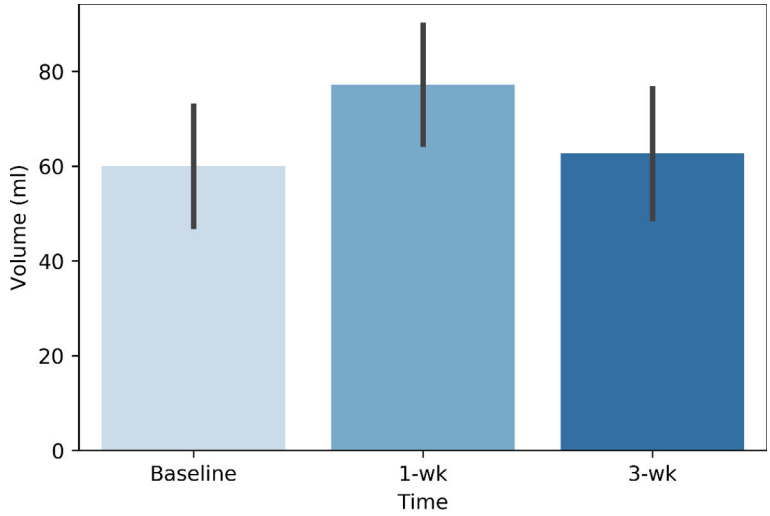

Figure 16. Average prostate volumes at different timepoints. (From original publication I).

Regarding the NPV, there was a gradual average volume increase of 23% between immediate and 1-week controls, and a subsequent increase of 24% between 1-week and 3-week controls. Overall mean increase from immediate to 3-week control was 41%.

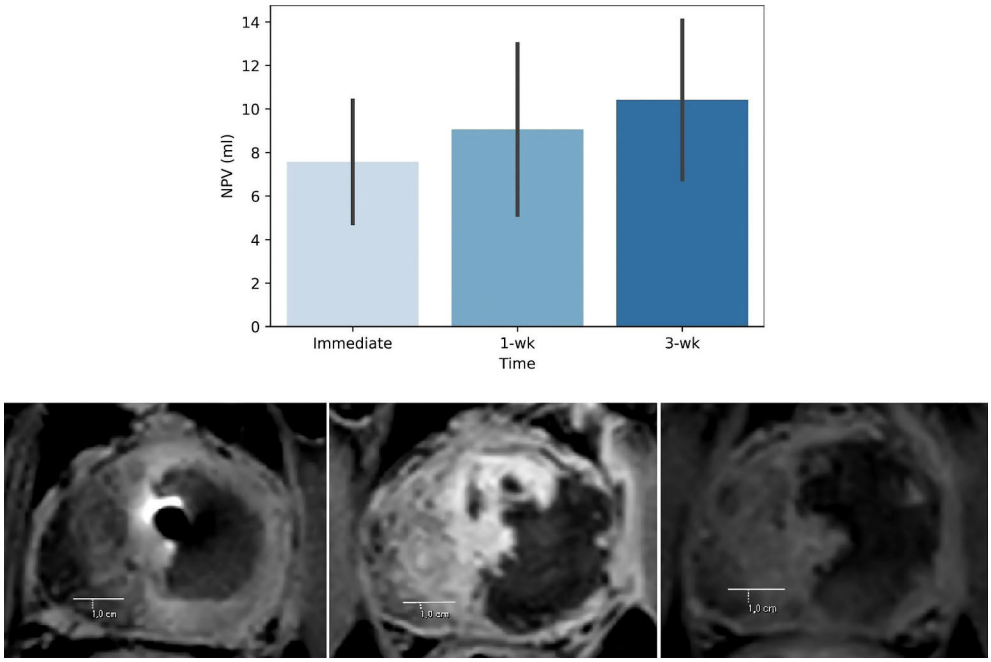

Figure 17. Average NPV volumes at different timepoints, and a patient example of NPV evolution. (Modified from original publication I).

5.1.2 Evolution of ADC values

The mean lesion (eight lesions altogether) ADC value in the baseline imaging was 819 (μm^2/sec). The corresponding average lesion ADC values in the 1- and 3-week MRI follow-ups were 970 and 769, respectively. Between the baseline and one-week follow-up MRIs, the ADC values increased in five out of six lesions (one patient with two lesions did not participate in the one-week MRI follow-up); the mean change was +15%. Between the 1- and 3-week MRI follow-ups, the ADC values decreased in every lesion with an average percentual change of –22%. The ADC values decreased between the baseline and three-week MRI follow-up, with a mean percentual change of –4%.

The reference ADC values showed negligible changes, with a mean percentual change in reference ADC values +0.2%, –0.2%, +0.4%, between baseline and 1-week, 1-week and 3-week, and baseline and 3-week MRI controls, respectively.

5.1.3 Detection and evolution of hemorrhage within NPV

In the histopathologic evaluation, signs of hemorrhagic necrosis were identified in the treatment region in all patients; see **Figure 18**. The presence of hemorrhage within NPV was analyzed as changes in T1W and T2W images with the SI being

compared to a non-hemorrhagic area of prostate. These changes were quantitatively defined as the T1 and T2 SIRs. Hemorrhage volumes were measured by manually contouring regions of T1 hyperintensity in the treatment area.

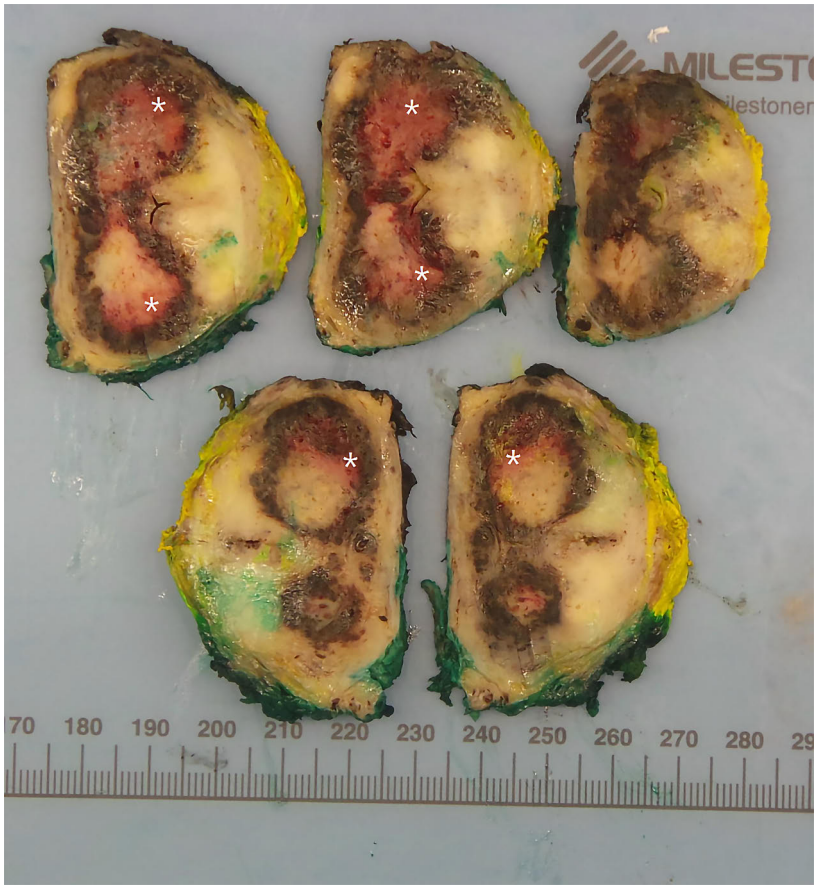

Figure 18. Macroscopic prostate specimen after RALP. Regions of hemorrhagic coagulation necrosis marked with asterisks. (From original publication I).

During the one-week follow-up, the average T1 SIR measured 1.21, which climbed to 1.26 by the three-week follow-up, reflecting a mean percentual increase of 7%. In contrast, the mean T2 SIR was 0.42 at the one-week assessment, declining to 0.31 at the three-week follow-up, indicating a mean percentual change of -29%.

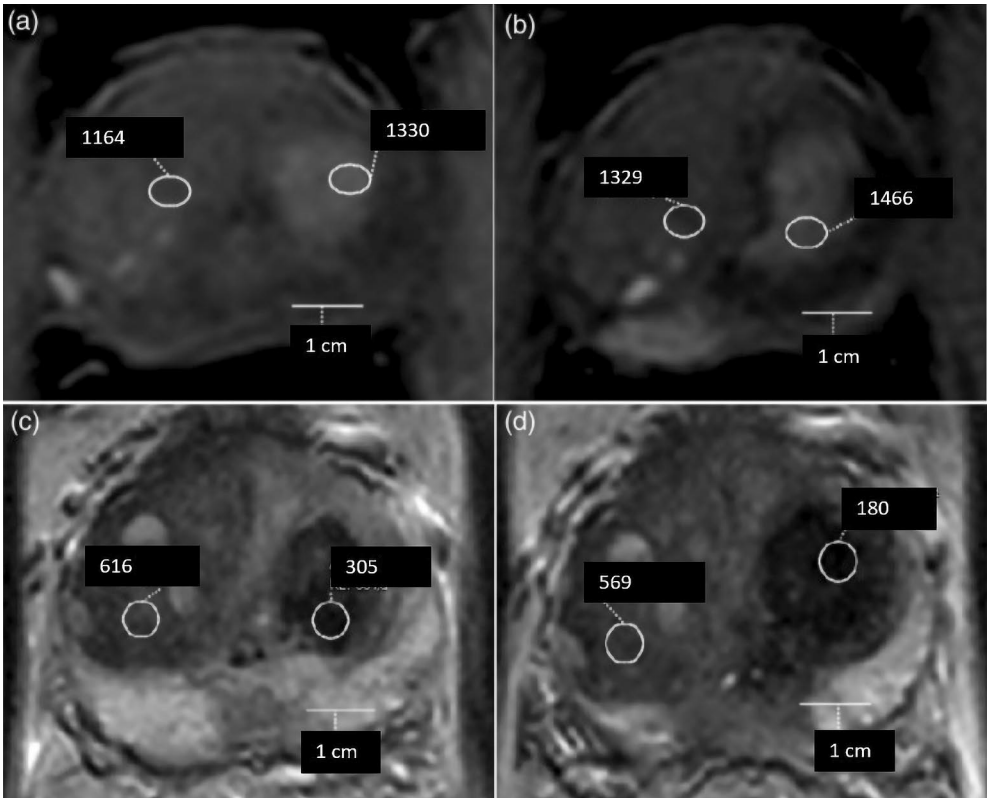

Figure 19. Example of T1 and T2 signal intensity measurements. The 1- and 3-week axial T1W fat-saturated non-contrast images (**a**, **b**), and the corresponding T2-weighted non-contrast images (**c**, **d**). (Modified from original publication I)

The average volumes of hemorrhage were 1.6 mL and 4.1 mL at 1 and 3 weeks post-TULSA, respectively. The mean percentual increase in hemorrhage volumes between 1- and 3-week follow-up studies was 110%.

5.2 Effect of gold fiducial markers on safety and early-stage efficacy (Study II)

5.2.1 Thermal dose coverage and residual enhancing tissue behind marker

Complete thermal dose accumulation behind markers and extending to the target boundary occurred in 16/18 (89%) fiducial markers. In one case, although 240 CEM was achieved to the prostate capsule, it did not reach the target boundary, which was drawn beyond the capsule to include the possibly diseased neurovascular bundle.

Viable enhancing prostate tissue was found for 13/18 (72%) markers immediately after treatment, 3/18 (17%) at three months, and 2/18 (11%) at 12 months (patient 4 with thermal undershoot). Refer to **Figure 20** for a patient example.

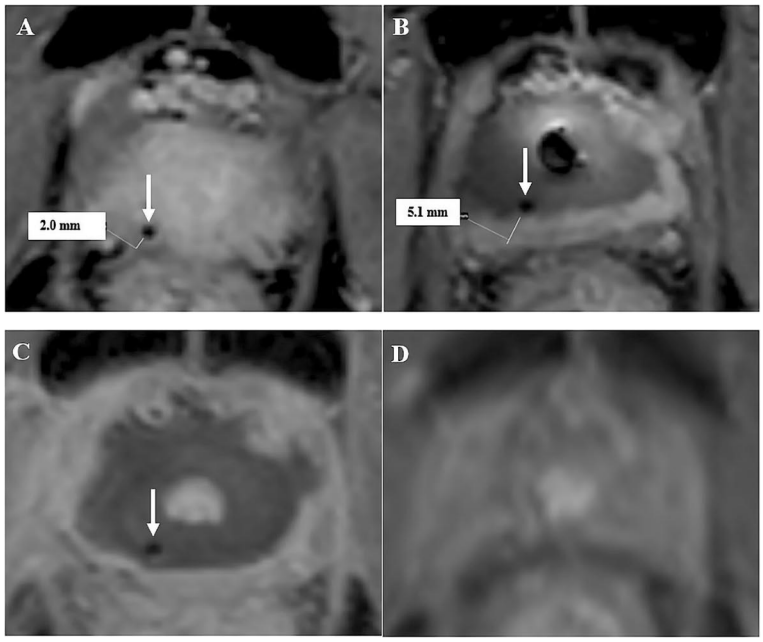

Figure 20. Example of a patient with a gold fiducial marker located on the right apical posterolateral corner (white arrow). The amount of enhancing tissue between marker and prostate capsule is shown (**A**) on baseline MRI scan and (**B**) immediately after treatment. At 3-month MRI (**C**), no enhancing prostatic tissue behind the marker was seen, only periprostatic enhancing fibrotic capsule. At 12-month MRI (**D**), both the non-perfused tissue and marker had disappeared. (From original publication II)

As an additional finding at 12-month MRI follow-up, 11/18 (61%) fiducial markers had disappeared, three were attached to the periprostatic scar tissue-like capsule, three were located within the NPV, and one remained within the vital-looking prostatic tissue. **Table 6** summarizes the findings on thermal dose and residual enhancing tissue.

Table 6. Treatment and fiducial marker characteristics. (Adapted from original publication II)

Patient	sTULSA treatment	Fiducial marker	markers within treatment zone	Thermal dose undershoot	Enhancing tissue between marker and capsule (baseline – immediate-3mo-12mo)	Markers remained at 12mo control
1	01/2019, right hemiablation	Gold marker, manufacturer unknown (1x3 mm based on CT scout)	R/apex/PL	6.2 mm (target boundary drawn outside capsule)	5.5 – 0 – 0 – 0 mm	disappeared
2	03/2019, extended left hemiablation	GoldLock 1x5 mm	L/mid/PL	0 mm	2.0 – 0 – 0 – 0 mm	disappeared
3	06/2019, whole-gland	GoldLock 1x3 mm	R/apex/PL R/mid/PL L/mid/PL	0 mm 0 mm 0 mm	4.5 – 3.4 - 0 – 0 mm 4.8 – 6.1 – 0 – 0 mm 4.0 – 5.0 – 0 – 0 mm	disappeared disappeared disappeared
4	11/2019, whole-gland	QLRAD Gold Fiducial Marker 1.2x3 mm	R/mid/PL R/base/PL L/apex/PL	3.5 mm 0 mm* 0 mm	7.5** – 5.0 – 3.6 – 3.1** mm 2.0** – 2.2 – 2.4 – 2.1** mm 3.0** – 2.1 – 0 – 0** mm	disappeared remained disappeared
5	03/2020, whole-gland	Gold marker, manufacturer unknown (2x4 mm based on CT scout)	R/mid/PL L/mid/ant	0 mm 0 mm	3.9 – 0 – 0 – 0 mm 7.2 – 0 – 0 – 0 mm	disappeared disappeared
6	09/2020, whole-gland	GoldLock 1x5 mm	R/apex/PL R/mid/PL L/mid/PL	0 mm 0 mm 0 mm	2.0 – 5.1 – 0 – 0 mm 3.0 – 2.0 – 0 – 0 mm 2.5 – 1.5 – 0 – 0 mm	disappeared remained*** remained***
7	09/2020, whole-gland	GoldLock 1x3 mm	L/mid/PL R/base/PL	0 mm 0 mm*	3.1 – 0 – 0 – 0 mm 1.5 – 1.7 – 1.6 – 0 mm	disappeared remained***
8	10/2020, whole-gland	GoldLock 1x3 mm	R/apex/PL R/mid/PL L/base/PL	0 mm 0 mm 0 mm	3.9 – 3.5 – 0 – 0 mm 5.1 – 3.8 – 0 – 0 mm 5.6 – 3.9 – 0 – 0 mm	remained**** remained**** remained****

* marker very close to target boundary, which might contaminate the thermal dose map; ** contrast-enhanced series not applicable, thickness of prostatic tissue between marker and capsule measured from T2W images; *** remained markers attached to periprostatic T2 dark fibrotic tissue; **** Patient 8 (unlike other patients) had still significant amount of non-enhancing prostate tissue left at 12-month MRI control, markers placed within non-perfused prostate tissue

5.2.2 PSA, imaging, and histopathology

Mean PSA decreased by 97% at 12 months, and trending downward in all but one patient. Patient 4 had rising PSA at 3 months post-TULSA (from 1.6 to 3.7 ng/mL). Mean prostate volume decreased by 22% at 3 months and by 78% at 12 months. Similarly, the average NPV was 20.7 mL immediately after treatment, and 15.9 mL at three months, a decrease of 23%. Only one patient had remaining NPV at 12 months.

MRI control suggested local recurrence for one patient, based on DWI sequence (patient 2). However, both PSMA-PET-CT and prostate biopsies were negative for the same patient.

PSMA-PET-CT control studies indicated no local recurrences inside the prostate for any of the patients. However, both patients 5 and 7 had small focal PSMA uptakes in the right seminal vesicle. Patient 4 with early rising PSA had positive PSMA-PET-CT already at 3 months post-TULSA showing PSMA uptakes on the right seminal vesicle, right parailiac lymph nodes, and bone metastasis. Refer to **Figure 21** for a patient example of a successful treatment.

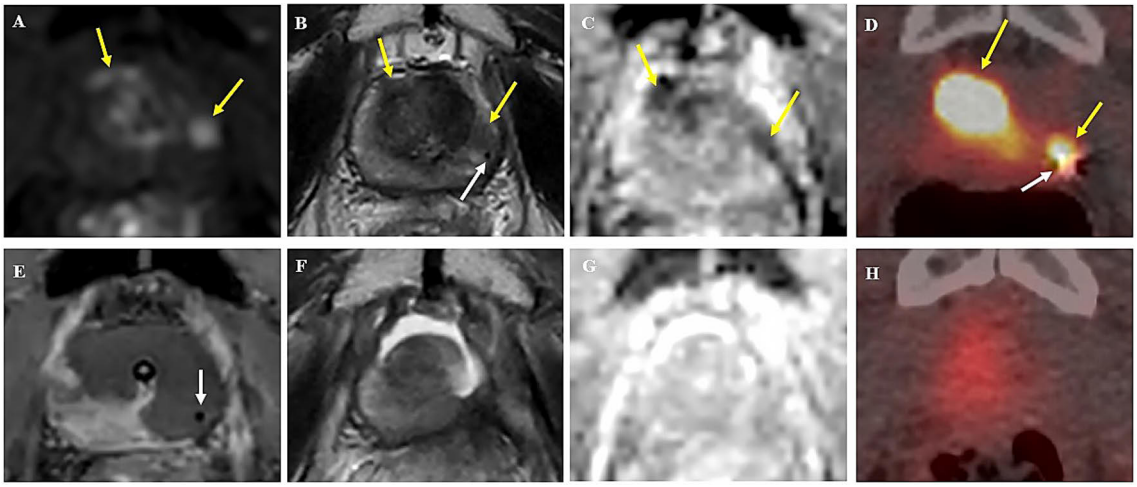

Figure 21. (**A**–**D**) Baseline imaging of a patient, with radiorecurrent right anterior and left lateral mid-gland tumor foci. (**A**) Yellow arrows indicate early enhancement, (**B**) T2 hypo-intensity, and (**C**) restricted diffusion on baseline MRI. (**D**) Baseline PSMA-PET-CT revealed significant uptake in regions concordant with MRI-visible PI-RR 5 lesions. (**B**, **D**, **E**) Fiducial marker is visible in the near vicinity of the left tumor (white arrow). (**E**) Immediately after treatment, the NPV reached to the capsule in both tumor locations. (**F**) At 12 months, MRI shows a fluid-filled cavity and (**G**) no diffusion restriction in the treatment area, and (**H**) PSMA-PET-CT shows no intensive focal uptake. The marker had also disappeared. (From original publication II)

Patient 5 did not receive biopsies due to fistula to the symphysis joint and osteitis of the pubic bone. Due to the early-onset, PSMA-PET-CT based metastatic disease for patient 4, no prostate biopsies were taken from this patient. Of the six patients that underwent prostate biopsies, all were negative. **Table 7** summarizes the findings.

Table 7. Baseline and follow-up findings. (From original publication II)

Patient	Prostate volume, baseline-3mo-12mo (mL)	NPV, immediate-3mo-12mo (mL)	PSA, baseline-3mo-12mo (ng/mL)	12mo MRI control	12mo PET-CT control (SUVmax)	12mo biopsy results
1	23.6 – 23.7 – 8.7	16.7 – 10.9 – 0	11 – 0.31 – 0.18	no suspicion of recurrence	no recurrence / metastasis	benign (4 cores)
2	37.2 – 36.3 – 12.6	17.1 – 16.8 – 0	4.7 – 0.38 – 0.24	small diffusion restriction focus R/mid/ant	no recurrence / metastasis	benign (6 cores)
3	23.5 – 3.5 – 2.9	20.8 – 0 – 0	0.08 – 0.04 – 0.22	no suspicion of recurrence	no recurrence / metastasis	benign (6 cores)
4	44.8 – 35.5 – 1.6	28.2 – 33.1 – NA (non-contrast MRI)	1.6 – 3.7 – 0.01	no suspicion of recurrence	3mo PET-CT: no recurrence in prostate, but metastatic disease*	not biopsied**
5	30.0 – 4.5 – 1.8	31.0 – 1.2 – 0	1.9 – <0.02 – 0.03	no suspicion of recurrence	20mo PET-CT: R seminal vesicle (11.1)	not biopsied***
6	23.1 – 21.0 – 1.1	12.9 – 15.0 – 0	13 – 0.10 – 0.06	no suspicion of recurrence	no recurrence / metastasis	benign (2 cores)
7	20.3 – 22.8 – 0.8	20.9 – 20.8 – 0	3.4 – 0.18 – 0.34	no suspicion of recurrence	doubtful small focus R seminal vesicle (4.4)	benign (4 cores)
8	32.9 – 37.0 – 21.9	17.9 – 29.0 – 15.9	2.7 – 0.01 – 0.01	no suspicion of recurrence	no recurrence / metastasis	benign (4 cores)

* PSMA-PET-CT carried out 3 months post-TULSA, based on significant PSA rise at 3-month control (from 1.6 to 3.7). PSMA-PET-CT showed metastasized disease: right seminal vesicle (SUVmax 14.9), three right parailiacal lymph nodes (SUVmax ad 10.2) and four bone lesions (SUVmax ad 14.2); ** Not biopsied, because PSMA-PET-CT 3 months post-TULSA showed metastasized disease.; *** Not biopsied, because of the urinary fistula to symphysis.

5.2.3 Safety

In the marker cohort, four grade 2 AEs (three whole-gland, one partial) and one grade 3 AE (whole-gland) occurred across eight patients. The most common events were urinary tract infections (UTI) which all resolved with oral antibiotics. The grade 3 AE included urinary retention and fistula formation to the symphysis joint with osteitis, requiring long-term peroral antibiotic treatment and suprapubic catheterization. In the control cohort, four grade 2 (three whole-gland, one partial) and two grade 3 events (both whole-gland) were recorded across 13 patients. Grade 2 events included two patients with UTI and two patients with both UTI and retention. Grade 3 events included J-stent insertion and a urethral stricture. No rectal fistulas were observed in either cohort.

For the marker cohort at 12 months, a noteworthy 45% and 116% deterioration from baseline was observed for EPIC-26 urinary incontinence and IPSS urinary

symptoms, respectively. A modest 14% decrease in EPIC-26 irritative/obstructive domain was also observed, but bowel and hormonal domain scores remained constant. In contrast, there were no significant decreases in any functional outcomes at 12 months for the control cohort.

Within the whole-gland subgrouping (both groups included 6 patients), no statistically significant difference between the two groups were found in the mean change between baseline and 12 months of EPIC-26 urinary incontinence domain ($p <= 0.884$), irritative domain ($p = 0.309$), IPSS ($p = 0.937$), or any other scores. See **Table 8** for functional status of salvage patients.

Table 8. Functional status before and after salvage TULSA treatment (first table including both whole-gland and partial treatments, while second table only whole-gland treatments). (Modified from original publication II)

Both whole-gland and partial treatments	**Non-marker patients (median score)** n=13			**Marker patients (median score)** n=8		
	Baseline	3 mo	12 mo	Baseline	3 mo	12 mo
EPIC-26 urinary incontinence	100	100	92	96	40	53
EPIC-26 irritative/obstructive	94	78	88	91	81	78
EPIC-26 bowel	90	94	94	100	96	100
EPIC-26 sexual	18	17	17	18	15	13
EPIC-26 hormonal	98	95	95	95	100	100
IPSS urinary symptom score	7	13	8	6	17	13
IPSS quality of life	2	4	2	1	4	3
IIEF-5 erectile function	0	0	0	2	0	2

Only whole-gland treatments	**Non-marker patients (median score)** n=6			**Marker patients (median score)** n=6		
	Baseline	3 mo	12 mo	Baseline	3 mo	12 mo
EPIC-26 urinary incontinence	100	71	59	89	34	53
EPIC-26 irritative/obstructive	94	72	75	85	81	78
EPIC-26 bowel	96	90	90	100	96	98
EPIC-26 sexual	24	17	15	18	15	8
EPIC-26 hormonal	98	95	93	95	95	100
IPSS urinary symptom score	12	24	14	6	17	13
IPSS quality of life	2	4	3	2	4	3
IIEF-5 erectile function	0	0	0	2	0	2

5.3 Evolution of non-perfused volume after TULSA (Study III)

5.3.1 NPV

Figure 22 shows the absolute NPV changes during the follow-up. Compared to the immediate post-treatment NPV, the median NPV decreased by 14.9 mL (77% decrease) in 3 months for the BPH cohort. For the same BPH cohort, there was virtually no NPV left at 12 months (99% decrease). For the radiorecurrent PCa cohort, the median NPV increased by 4% at 3 months, but by 12 months, most of the NPV had disappeared. For the primary PCa cohort, the NPV had almost entirely disappeared by six months, showing a 97% decrease compared to immediately post-treatment, and the same trend continued at 12 months. There was no statistically significant difference between groups in the relative NPV change at 12 months ($p = 0.132$, Kruskal-Wallis).

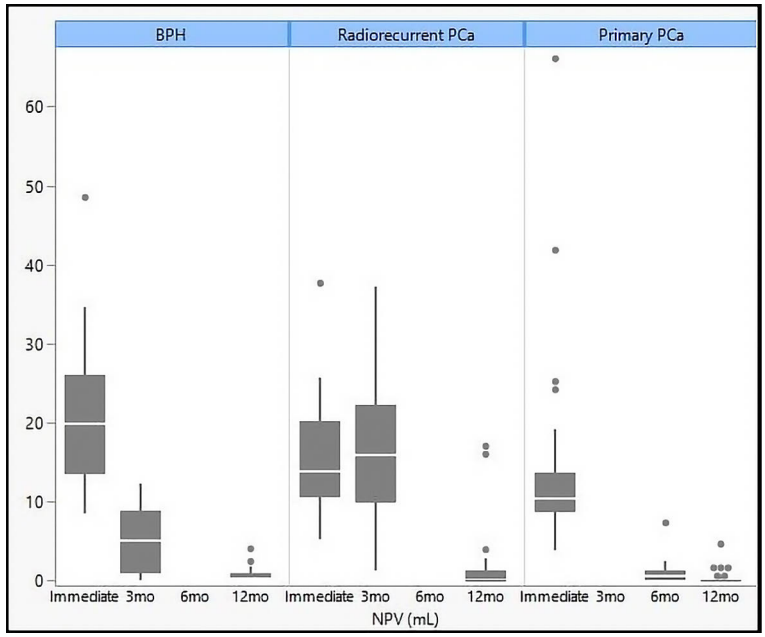

Figure 22. NPV values for each subgroup at different timepoints. (Adapted from original publication III)

At 12 months, measurable NPV remained in 12/21, 12/28 and 12/40 patients in the BPH, radiorecurrent and primary PCa groups, respectively. If NPV remained, the total amount was mainly small, typically less than 1 mL. There were, however, two notable outliers in the whole-gland radiorecurrent PCa cohort, whereby two patients

had residual NPV of 16 and 17 mL at 12 months, respectively. Refer to **Figure 23** for patient examples of NPV evolution.

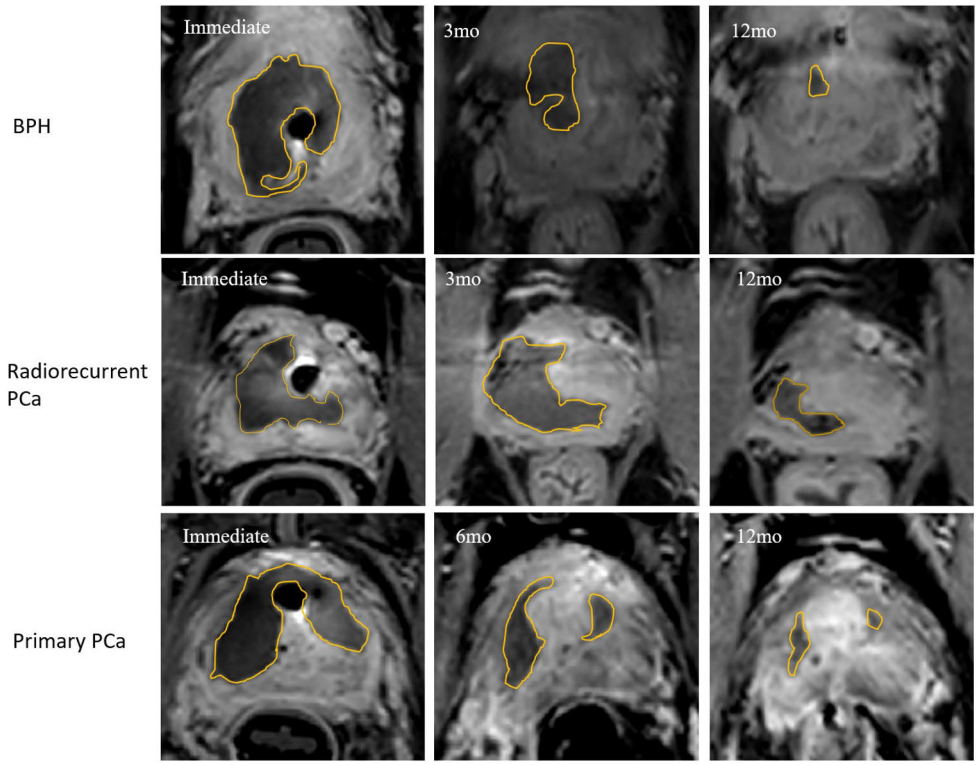

Figure 23. Examples of NPV evolution for a BPH (upper row), a radiorecurrent PCa (middle row) and a primary PCa (bottom row) patient. (From original publication III)

There was a significant difference in the median relative change of the NPV at 3 months between the BPH and radiorecurrent PCa cohorts ($p < 0.0001$, Wilcoxon rank sum test), with the latter harboring considerably more necrotic tissue based on NPV. In the radiorecurrent and primary PCa cohorts, subgroup analysis between partial and whole-gland treatment groups were made, and one significant difference was found at three months: radiorecurrent PCa patients undergoing partial salvage ablation had a median NPV change of -14%, while whole-gland salvage patients had a median NPV change of +13% ($p = 0.024$, Wilcoxon rank sum test).

In a BPH subgroup analysis, patients who received two sweeps ($n = 10$) of the transition zone and patients with only one sweep ($n = 11$), had no statistically significant difference on the immediate mean NPVs ($p = 0.606$, two-sample t-test), nor in the relative NPV change at 3 months ($p = 0.698$, Wilcoxon rank sum test) or at 12 months ($p = 0.435$, Wilcoxon rank sum test).

5.3.2 Prostate volume

For the BPH cohort, the median prostate volume decreased by 29% at 3 months compared to baseline and by 34% at 12 months. For the radiorecurrent PCa cohort, a slight median prostate volume increase of 1% was recorded at 3 months, followed by a noticeable 85% decrease at 12 months. Finally, for the primary PCa cohort, the median prostate volume decreased by 36% at 6 months and 41% at 12 months.

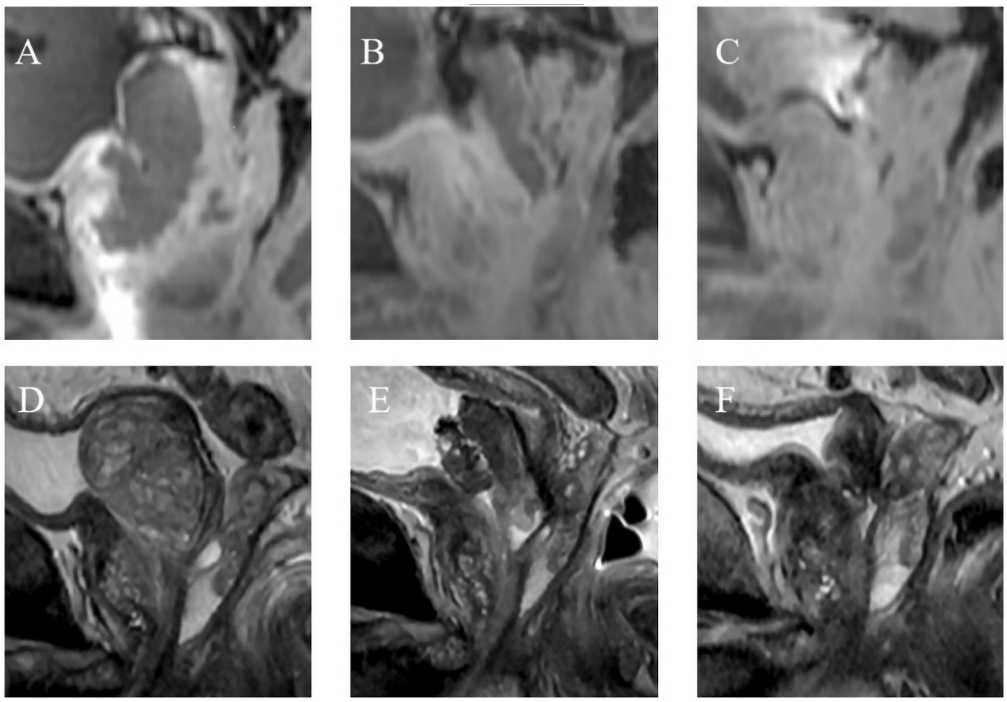

Figure 24. Gradual disappearance of NPV and prostatic tissue in a BPH group patient. In the upper row T1W fat-saturated contrast-enhanced sagittal images; immediately (**A**), 3 months (**B**) and 12 months (**C**) after treatment. Lower row shows T2W sagittal images; pre-treatment (**D**), 3 months (**E**) and 12 months (**F**) post-TULSA. At 3 months, NPV has clearly diminished compared to large immediate NPV, and disappeared at 12 months. (From original publication III)

6 Discussion

6.1 Early post-procedural MRI changes after TULSA

To my knowledge, Study I was the first one to evaluate such a broad range of short-term MRI changes after thermal ablation using therapeutic ultrasound. Repeated MRI scans over three weeks and their comparison to the histology of the removed prostates allowed accurate observations to be made regarding temporal changes in the whole gland and lesion area.

In a previous study of transrectal HIFU, it was reported that there was, on average, a 19% increase in prostate volume 2–5 days after treatment, a change likely attributed to post-procedural edema (Rouvière et al., 2001). Findings of our study are consistent with this, showing an increase in prostate volume in all patients during the 1-week follow-up (+29% on average). However, between the 1- and 3-week MRI follow-ups, prostate volumes decreased in every patient, presumably due to reduction in post-treatment edema. By 3 weeks, prostate volumes had returned close to the baseline values (+5% on average). These findings suggest that maximal post-procedural edema occurs one week after treatment, followed by a gradual decrease within a few weeks.

Previous research on heat-based prostate ablation has demonstrated that NPV, as assessed with contrast-enhanced MRI, corresponds with tissue necrosis observed on histopathology (Bomers et al., 2017; Boyes et al., 2007; Lindner, Lawrentschuk, Weersink, et al., 2010). Additionally, earlier pre-clinical studies on thermal ablation have indicated the presence of a transition zone characterized by sublethal damage, situated between the area of acute coagulation necrosis and preserved vital tissue (Bomers et al., 2017; Chu & Dupuy, 2014). In pre-clinical TULSA studies, this transition zone of potential delayed coagulation necrosis was observed to be few millimetres in radius (Boyes et al., 2007; Chopra et al., 2009; Siddiqui et al., 2010). However, in clinical study settings, the subacute evolution of NPV following TULSA has not been previously investigated. In Study I, we observed a significant increase in NPV between the immediate post-treatment and 3-week follow-up MRIs (averaging +41%). These findings confirm the pre-clinical observations that significant delayed necrosis occurs after TULSA treatment.

The MRI signal of hemorrhage is recognized to undergo changes based on the age of the hemorrhage, which involves various blood products such as oxyhemoglobin, deoxyhemoglobin, and methemoglobin (Bradley, 1993). Post-biopsy hemorrhage within the prostate is typically identified as an area of low T2 signal intensity corresponding to T1 hyperintensity, and it may require up to four months for the hemorrhage to resolve (Ahmed et al., 2009; White et al., 1995). The existing literature on MRI observations of subacute hemorrhage following HIFU or TULSA treatment is scarce. In their study on transrectal HIFU, Rouvière et al. observed slight hyperintense T1 foci and increased T2 hypointensity, likely indicating hemorrhage within the treatment area 2–5 days post-treatment (Rouvière et al., 2001). Based on this prior knowledge and histopathologic hemorrhagic findings in our study, we aimed to evaluate hemorrhage within NPV as changes in the T1 and T2 SI. In the T1 images, the visual hemorrhagic changes were rather subtle. The T2 hypointensity in hemorrhagic areas was more apparent. At the 3-week follow-up MRI, the hemorrhage within NPV was more clearly demarcated and larger when compared to 1-week images. T1 and T2 SIRs supported the visual observations, i.e. the T1 SI values in the hemorrhagic areas were mildly higher than those in the non-hemorrhagic area of prostate (average SIR values 1.26 and 1.21). Furthermore, T2 hypointensity in the hemorrhagic areas was more readily distinguishable (average SIR values 0.31 and 0.42). We did not find any published data considering the post-biopsy hemorrhage SIR, but according to our experience, the post-biopsy hemorrhage is more clearly visualized as T1 hyperintensity even a few months after biopsy. Most likely the relatively subtle T1 hyperintensity after TULSA is due to the thermal coagulation of hemorrhage.

DWI is integral for tumor characterization in prostate MRI. ADC values have an inverse relationship to Gleason grades (Hambrock et al., 2011). There is prior evidence that prostate post-biopsy hemorrhage affects ADC values (Lee et al., 2011). Following thermal ablation of the prostate over the long term, the treated areas demonstrate shrinkage, fibrosis, fluid-filled cavities, and architectural distortion. These post-treatment changes contribute to a gradual increase in ADC values within the targeted area in successful treatment scenarios (Gaur & Turkbey, 2018; Kim et al., 2008; Lotte et al., 2018; Patel et al., 2018). Previous studies have not investigated the impact of thermal ablation on DWI or its utility in assessing treatment outcomes in the subacute phase. In our study, the ADC values increased on average by 15% one week after treatment, which would indicate a favourable treatment outcome. However, at the 3-week MRI follow-up, the ADC values did not continue to increase, but, on the contrary, they markedly decreased (–22% on average). The 3-week ADC values were on average slightly decreased (–4%) when compared to baseline values. It is likely that the rise in ADC values observed at one week is primarily attributed to post-treatment edema. Subsequently, as the edema subsides

and post-treatment hemorrhage becomes more organized, the ADC values decreased by the 3-week MRI follow-up (Silvera et al., 2005). It could be argued that the persistently low ADC values might also indicate residual cancer. However, all measurements were taken within the non-perfused areas of the prostate. For instance, patient 2 in Study I, who showed no signs of residual cancer in histopathological evaluation, exhibited the aforementioned increase at one week and decrease at three weeks in ADC values. Hence, it appears evident that due to post-procedural changes, primarily edema and hemorrhage, DWI does not offer additional value in assessing the ablation zone in the subacute phase post-TULSA.

6.2 Effect of fiducial markers on treatment outcome

Study II was the first clinical investigation to evaluate the safety and efficacy of salvage TULSA for radiorecurrent PCa in the presence of intraprostatic gold fiducial markers.

There were valid concerns regarding the potential negative impact of fiducial markers on the efficacy of ablation within the prostate. Simulation studies on HIFU have suggested that the position of gold markers relative to the ultrasound focus can diminish the amount of thermal energy reaching the focus, potentially resulting in undertreatment (Bakaric et al., 2018; Georgiou et al., 2017). Similarly, another ultrasound simulation study examining calcifications, which share similar acoustic properties with fiducial markers, reached comparable conclusions (Suomi et al., 2018). However, a contrasting HIFU gel phantom study concluded that markers do not significantly affect the thermal dose when the ablation volume is extensive (Mougenot & Moonen, 2017). Another consideration in MRI-guided ablation therapies is the production of local magnetic susceptibility artifacts by fiducial markers (Jonsson et al., 2012; Schenck, 1996; Tatebe et al., 2016). The thermometry sequence employed in TULSA is notably sensitive to magnetic susceptibility changes (Tatebe et al., 2016), and a significant artifact on thermometry may compromise the accuracy of temperature measurements. In terms of safety, localized "hot spots" may also develop in front of the marker (Bakaric et al., 2018), potentially increasing the risk of complications and compromising functional outcomes.

The technical aspects, marked-induced artifacts and thermal dose assessments of this same study population are elaborated upon in greater detail in our separate publication beyond this thesis (Wright et al., 2021). Study II served as a clinical extension to that study.

In our study, there was no evidence of marker-induced undertreatment by 12 months for 16/18 (89%) markers based on contrast-enhanced MRI. The two exceptions both occurred in patient 4, where a small amount of residual vital-looking tissue was still apparent. One of those markers was positioned close to the prostatic

urethra (≤ 12 mm) but also far from target boundary (≥ 13 mm), and the resulting undertreatment can be explained by an ultrasound shadowing effect caused by the marker (Wright et al., 2021). The other marker, located in a similar posterolateral position slightly cranial to the first one, likely experienced the same shadowing effect. Fortunately, it appears the two markers were not in the vicinity of the cancer and therefore did not result in local recurrence based on imaging.

The MRI results were in line with the local oncological control findings among patients with fiducial markers. Only one individual exhibited any suspicion of local recurrence within the prostate on MRI scans, yet both PSMA-PET-CT and biopsy results turned out negative. Apart from this case, all imaging and histopathological evaluations within the prostate revealed negative findings. Furthermore, there was a notable decrease of 97% in PSA levels, and among the six patients who underwent whole-gland treatment, prostate volume decreased by 94%. All instances of recurrence were observed outside the prostate, either in the seminal vesicles alone or additionally in the lymph nodes and bone. In summary, these findings indicate that fiducial markers do not significantly affect early-stage oncological outcomes.

In a meta-analysis on local salvage therapies (Valle et al., 2021), severe genitourinary toxicity (Clavien–Dindo grade ≥ 3 event or an IPSS score ranging from 20 to 35) incidence rates were 23%, 21%, and 4.2% for salvage HIFU, prostatectomy, and stereotactic body radiotherapy, respectively. Gastrointestinal toxicity rates were generally low, with salvage prostatectomy showing the highest incidence of 1.9%. Under these criteria, our study found that one patient in the marker cohort (13%) and three patients in the control group (23%) experienced severe genitourinary toxicity. While these rates align with those of other treatment modalities, it's noteworthy that all instances of severe toxicity resulted from whole-gland rather than partial-gland treatments, and the presence of fiducial markers did not appear to influence the overall genitourinary safety profile. The most severe adverse event observed in our study, caused by anterior thermal overshoot, was a grade 3 urinary fistula from the prostate bed to the symphysis joint leading to pubic bone osteitis. The likely cause of this overshoot was the interplay between post-radiation tissue changes (such as a narrowed retropubic space and the absence of viable blood vessels providing a cooling effect) and the TULSA device's frequency transition, which shifts between low (4 MHz) and high (14 MHz), occurring at the 14 mm target boundary. Additionally, virtually no gastrointestinal toxicity was observed in any group.

In Study II, urinary symptom outcomes impaired in both the marker and non-marker groups at 12 months. Subgroup analysis, focusing on whole-gland and partial ablation approaches, indicated that the extent of ablation, rather than the presence of markers, primarily contributed to this deterioration in functional outcomes.

6.3 Resolution of necrotic tissue after TULSA

Study III measured the NPV at different time points after TULSA for different treatment cohorts, including BPH, radiorecurrent PCa, and primary PCa patients.

Even though NPV has traditionally served as a secondary marker for treatment outcome following heat-based ablation therapies, previous understanding regarding the evolution of NPV and the mechanism underlying NPV resolution remains limited. Furthermore, the potential impact of substantial residual necrotic tissue, manifesting as NPV, on lower urinary tract irritation and voiding symptoms, particularly in the months following treatment, has been overlooked. Moreover, salvage therapy for patients with radiorecurrent PCa tends to exhibit higher toxicity compared to treatment-naïve patients (Anttinen et al., 2022; Valle et al., 2021). The precise reasons for these differences are not well understood, but NPV and prostate volume alterations are likely contributing factors. A detailed comprehension of this phenomenon could assist physicians in anticipating and managing the related side effects more effectively, thus optimizing follow-up protocols.

Some researchers have documented changes in NPV following prostate ablation therapy. In a study by Rouvière et al. involving primary PCa patients undergoing ultrasound-guided transrectal HIFU (both whole-gland and lesion-targeted treatments), only 2 out of 11 patients (18%) exhibited measurable NPV at 3–5 months post-treatment (Rouvière et al., 2001). Another study (Kirkham et al., 2008) involved 14 patients undergoing ultrasound-guided HIFU for primary PCa, where roughly 60% of patients still had measurable NPV at 6 months. Any residual NPV, if present, was minimal. The findings from our current study align with these prior observations at 6 months. In the primary PCa group, 26 out of 40 patients (65%) exhibited residual NPV. In cases where residual NPV was detected, it tended to be very small, with a median value of 0.4 mL.

Despite the lack of NPV evolution studies for BPH patients, Mueller-Lisse et al. (Mueller-Lisse et al., 1996) conducted a study on treatment-induced lesion core volume changes following laser ablative therapy for BPH. In this study, only T2W imaging on a 1.0 T MRI scanner was employed to determine the lesion core size at subsequent time points by comparing it to a control scan shortly after treatment. This was achieved by delineating the T2 hypointense area surrounded by a hyperintense rim. The authors reported lesion core volumes for four patients at 2 months (with a mean decrease of 55%) and for only one patient at 6 months (with a 96% decrease). While these results cannot be directly compared to the findings of our study due to the absence of contrast-enhanced images, there is previous evidence suggesting that T2 assessment of lesion core volume correlates with T1W contrast-enhanced measurements (Staruch et al., 2017). In this context, the study by Mueller-Lisse et al. aligns with our results, where the median NPV decreased by 77% at 3 months.

At the 12-month mark, only one study (Bonekamp et al., 2019) reported NPV changes following prostate ablation. This study included 29 patients who underwent whole-gland TULSA. They reported median NPV values of 19 mL immediately after ablation and 9 mL at 12 months. In contrast, our study's results indicated that by the 12-month mark, only 12 out of 40 (30%) patients had any residual NPV, and if present, it tended to be negligible, with a median value of 0 mL (0–0.1). Discrepancies could have arisen due to differences in NPV measurement techniques. For instance, including fluid-filled cavities or cysts in NPV measurements might have inflated the post-ablation NPV. Additionally, variations in treatment strategies could have impacted the results. However, these differences persisted regardless of whether whole-gland or partial gland treatment was performed. In our primary PCa cohort, which included nine whole-gland treatments, the median NPV was 16 mL (13–24) immediately post-TULSA and 0 mL (0–1) at 12 months.

While some authors have documented NPV changes following prostate ablation in treatment-naïve prostate tissue, there is a lack of evidence regarding previously irradiated tissue. Radiation therapy induces various delayed tissue changes, including fibrosis, necrosis, atrophy, and vascular damage (Stone et al., 2003), which prolong the tissue recovery process. In our current study, a notable difference in NPV was observed at 3 months between the BPH and radiorecurrent PCa groups. In the BPH cohort, the median NPV change at 3 months was -77%. Conversely, in the radiorecurrent PCa cohort, NPV had not decreased but rather increased by 4%. Previous studies have indicated that patients undergoing salvage TULSA for radiorecurrent PCa often experience more severe and frequent urinary symptoms in the initial months post-treatment compared to those undergoing TULSA for treatment-naïve prostate diseases (Anttinen et al., 2022). However, based on our studies (Anttinen, Mäkelä, Viitala, et al., 2020; Study II), urinary symptoms in TULSA-treated radiorecurrent PCa patients tend to slightly improve within one year. The findings from our study, showing a slower disappearance of necrotic tissue after TULSA in radiorecurrent PCa patients, may partly explain this phenomenon.

One notable distinction emerged in the subgroup analysis comparing partial versus whole-gland salvage ablation for radiorecurrent PCa at 3 months: NPV decreased following partial ablation and increased following whole-gland ablation. These findings suggest that the clearance of necrotic tissue may take longer when more of it is present. Conversely, after 6 months for the primary PCa group, no statistically significant differences in residual NPV were observed between the partial and whole-gland ablation subgroups. However, it is possible that this timeframe might be insufficient to detect any potential disparities. By 12 months, there were no statistically significant differences noted for either treatment group.

The process by which necrotic prostate tissue disappears following coagulative therapies remains uncertain. Previous studies on thermal ablation have indicated that

tissue resorption mediated by macrophages and other inflammatory cells is one probable mechanism (Chu & Dupuy, 2014; Nikfarjam et al., 2005). However, findings from Study II suggest an additional pathway. In Study II we found that 11 out of 18 fiducial markers had vanished from the ablation zone by the 12-month mark. This disappearance suggests that sloughing of necrotic tissue via the prostatic urethra most likely contribute to tissue clearance, as this appears to be the only viable pathway for the markers to be eliminated.

6.4 Limitations

The sub-studies within this doctoral thesis faced several limitations. A common constraint across all sub-studies was the patient and disease heterogeneity, with variability in lesion sizes, prostate baseline volumes, and ablation volumes. Furthermore, post-procedural alterations in the prostate and surrounding tissues added complexity to the assessment of MRI, compounded by the fact that only one reader evaluated the MRI findings.

Specific limitations of each sub-study:

- Study I: Most notably the small study population.
- Study II: This was a retrospective study with small patient cohorts. Marker composition was variable with respect to size. Additionally, only gold markers were studied, limiting the generalizability of the study.
- Study III: The study was conducted retrospectively. Primary PCa patients had their interim follow-up at six months instead of three, which made inter-group comparison challenging.

6.5 Implications / Future considerations

PSA screening of asymptomatic patients has increased, leading to the diagnosis of more low-risk PCa. As the population ages and life expectancy increases, PCa is being detected in older and more frail patients, for whom traditional curative treatments may be too burdensome and compromising to their quality of life. On the other hand, PCa in older patients may be managed preferentially with hormonal therapy rather than with curative treatments, even if curative treatment would be possible. Additionally, most of the radiorecurrent PCa patients even with localized recurrence, are treated with systemic ADT, which isn't curative and may cause various side effects. Hence, there is a need for less invasive and safer, yet locally radical treatment options alongside conventional therapies for both primary and

radiorecurrent PCa patients. TULSA and other ablative therapies for the prostate could provide a solution to this issue.

Ablative therapies, particularly the focal approach targeting MRI-visible biopsy-concordant csPCa lesions, are increasingly employed in the treatment of PCa. However, after focal prostate ablations, residual untreated prostate tissue remains alongside the ablated area, compromising the utility of PSA monitoring for cancer surveillance. Therefore, imaging methods play an increasingly vital role in monitoring focal cancer treatments. Consequently, there is a need for a deeper understanding of post-ablation changes in prostate tissue and their manifestation in MRI. This thesis contributes novel insights into MRI findings following ultrasound ablation of the prostate, as well as clinical implications of ultrasound ablation in the presence of fiducial markers.

The assessment of TULSA treatment outcome typically involves immediate post-treatment monitoring with contrast-enhanced MRI. Studies I and III revealed that the maturation of NPV, indicating the final treatment outcome, takes few weeks for treatment-naïve patients and even few months for salvage patients. Moreover, based on clinical experience, major complications such as fistula formation and osteitis are not immediately apparent post-treatment. There is also previous evidence that thermal dose serves as a better predictor of treatment outcome than immediate NPV assessment. Therefore, immediate and few-month post-treatment MRI follow-ups may not be necessary if the thermal dose adequately covers the targeted prostate area and patient recovery progresses as expected. However, at the one-year follow-up, when NPV and other post-procedural changes have largely resolved, MRI becomes preferable to assess the final treatment outcome and establish a baseline for potential future recurrence monitoring. If there are concerns of undertreatment indicated by the thermal dose or if the patient experiences concerning symptoms, an earlier MRI follow-up (e.g., at 3 or 6 months post-treatment) may be warranted.

In terms of safety and functional outcomes following TULSA treatment, Study II revealed that whole-gland salvage TULSA patients experienced more severe urinary symptoms compared to those who underwent partial ablation. Additionally, Study III indicated a slower resolution of necrotic tissue in whole-gland salvage patients, potentially contributing to this disparity. Further research with larger patient cohorts is necessary to confirm these findings in both primary PCa and salvage TULSA patients. If partial ablations are indeed shown to be significantly safer than whole-gland treatments, it could lead to a more focal approach, provided that cancer control remains comparable between focal and whole-gland treatments. Another aspect requiring deeper investigation regarding treatment safety and functional preservation is the comparison between anterior and posterior ablations. Given that the neurovascular bundles are located on the posterolateral corners of the prostate, posterior treatments presumably present higher risks for patients. This understanding

could assist in refining the patient selection process, particularly in determining whether patients with anterior lesions are better candidates for TULSA treatment.

Study II demonstrated the successful implementation of salvage TULSA treatment in patients with gold fiducial markers. However, further investigation is warranted with respect to various marker compositions and sizes. Clinical experience and previous research suggest that for example nitinol markers produce notably stronger artifacts in thermometry images, which currently limit the eligibility of many patients for salvage TULSA treatment. Nevertheless, the issue with nitinol markers appears to stem from the artifacts they produce in MR thermometry, rather than from mechanically obstructing ultrasound heating energy. A software update for the TULSA device could address this issue by enabling users to mitigate these artifacts in baseline thermometry imaging, and thus ensuring adequate thermal dose to areas previously impacted by MRI artifacts.

One research topic that emerged from the sub-studies related to this dissertation and clinical experience is the impact of ADT on the prostate and its MRI findings before TULSA, as well as its effect on treatment success. Our research group has already recruited patients for this study (NeoADT-TULSA, NCT05917860). An observed challenge in TULSA procedures is the risk of incomplete ablation of lesions in the posterolateral regions, most likely due to increased distance and tissue inhomogeneity between the urethra and the lesion, as well as the cooling effect of the neurovascular bundle. The hypothesis of this study is that pre-TULSA ADT will lead to prostate size reduction, decreased vascularity, and tissue homogeneity, thus presumably allowing better heat propagation in the tissue and thereby avoiding under-treatment. Regarding MRI findings, it is noteworthy to observe how pre-TULSA ADT treatment affects the size of both the prostate and tumor lesions, as well as their diffusion and perfusion. Furthermore, monitoring the evolution of NPV in pre-ADT prostate tissue after TULSA is also of interest.

7 Summary/Conclusions

The findings from the studies presented in this thesis led to the following conclusions:

I. Hemorrhage occurs in the prostate after TULSA treatment, with more pronounced demarcation and increased size observed at three weeks following the procedure. The optimal timing for MRI follow-up appears to be at the earliest at three weeks after treatment, when the post-procedural edema has decreased and the NPV has matured. Diffusion-weighted imaging provides little or no added diagnostic value in the subacute setting.

II. Radiorecurrent PCa patients with intraprostatic gold fiducial markers can be successfully treated with TULSA. However, markers located close to the prostatic urethra and far from target boundary may cause undertreatment; hence, patients with lesions in the direct line-of-sight of these markers should be thoroughly screened. The early-stage efficacy of salvage TULSA for patients with intraprostatic gold markers is encouraging and the safety profile seems unaffected by marker presence.

III. The resolution of necrotic tissue following TULSA was significantly slower in previously irradiated prostate tissue compared to treatment-naïve tissue. Additionally, salvage patients undergoing whole-gland ablation tended to retain more residual NPV compared to those undergoing partial ablation. These findings may contribute to the increased toxicity observed after salvage therapy for radiorecurrent cases, as well as for those undergoing whole-gland therapy. By 12 months, most of the necrotic tissue had resolved in all patient cohorts, including those with BPH, primary PCa, and radiorecurrent PCa treated with TULSA.

Acknowledgements

During my years at Turku University medical school, I never planned to get involved in scientific research. However, many years after graduating, I reconnected with my classmate, urology resident Mikael Anttinen. He lured me, a blue-eyed radiology resident, into a mystical project involving some kind of ultrasound waves, magnets and prostates. Seven years later, we find ourselves with completed theses on this new treatment. Mikael is the one to thank (or curse) for my scientific career. This thesis wouldn't have been possible without your tremendous effort in driving the entire TULSA project forward.

The godfathers behind this project were Professors Roberto Blanco Sequeiros and Peter Boström. Without your enthusiasm for science and curiosity for new waves in medicine, these kinds of projects would never happen. I am deeply grateful for your trust in me and guiding me in the world of science.

Special thanks to Aida Steiner, a fellow radiologist, for sharing the learning curve with me during the first year of TULSA treatments, and to radiologist Heikki Pärssinen who later stepped into the shoes of a co-burner of the prostate. My thanks also go to urologist Pertti Nurminen, a crucial member of TULSA team, with extraordinary skills in the management of air bubbles. It has been a priviledge to work alongside all of you and to share the ups and downs of this new treatment method.

I would also like to express my gratitude to the entire TULSA team at TYKS, including the physicists, radiographers, anaesthesia team, and research nurses in the urology department. Special thanks to the pathology department and the team at the Turku PET Centre for their invaluable diagnostic support. Additionally, I am grateful to all my co-authors, with particular appreciation to Teija Sainio for her expertise in the complex field of physics, Pekka Taimen for his thorough histological analysis and assistance with the writing process of the first article, and Cameron Wright for his invaluable contributions to the final two articles.

To my radiology colleagues at TYKS, especially those in the abdominal imaging sector: thank you for the numerous creative 10:30 a.m. lunches, your unwavering support, and covering for me during my research leaves. A special thanks to Jaana Keihäs, secretary of the radiology department, for her invaluable assistance with any

problem and the annoying bureaucratic details of daily work. I am also deeply grateful to the people in the Radiological Department at Seinäjoki Central Hospital for their mentorship during my residency.

I am grateful to Professor Jussi Hirvonen for serving on my doctoral training follow-up committee and offering wisdom when needed. I also want to express my gratitude to Associate Professors Harri Visapää and Niko Sillanpää for their valuable time reviewing my thesis and providing constructive feedback.

A heartfelt thanks to all the organizations that financially supported my research: TYKS Foundation, government R&D Funding, the Finnish Radiological Society, the Finnish Medical Society Duodecim, and the Cancer Foundation Finland.

I am also grateful to the Finnish public library system for providing free access to knowledge, entertainment, and peaceful working environments.

My deepest appreciation goes to all my teachers at Jouppi Elementary School, Seinäjoen Lyseo Middle School, Seinäjoki Upper Secondary School, and Turku University. I'd also like to acknowledge my fantastic coaches at Sepsi, S-Kiekko, TP-Seinäjoki, and IK for teaching me invaluable lessons beyond the classroom.

To my incredible friends, thank you for offering much-needed breaks from work, whether through sports, festivals, or weekends at Jorma's cabin. After completing this thesis, I am also delighted to share the academic (and spiritual) leadership of Team North Stars with Ph.D. Hartsa.

To my parents-in-law, Pasi and Johanna, thank you for being superb grandparents, and offering your babysitting services, as well as delicious food and sauna experiences in Kurikka.

I would like to express my gratitude to my dear parents and brother. Naturally, none of this would have happened without my parents Jarkko and Tarja. I am truly grateful for your constant belief in me and your endless support over the past 38 years. Additionally, your dedication as grandparents and the help you have provided with our children have been irreplaceable. I also want to thank my big brother Eemeli for setting an example of how to navigate life as a boy in 1990s Seinäjoki. Today, I greatly value your technical expertise and your contacts on preserving the vitality of my 2005 Toyota Corolla.

I owe my deepest gratitude to my amazing wife, Roosa, for loving and supporting me all these years. You are my Seinäjoki! I am also grateful for our lovely children, Helka and Liinu. You have reminded me what is truly important in life. I appreciate you all for being my backbone at home and for sharing the joys and sorrows of everyday life. You make all this effort worthwhile.

September 2024
Pietari Mäkelä

References

Abrams, P. (1994). New words for old: lower urinary tract symptoms for "prostatism". *BMJ*, *308*(6934), 929-930. https://doi.org/10.1136/bmj.308.6934.929

Agarwal, P. K., Sadetsky, N., Konety, B. R., Resnick, M. I., & Carroll, P. R. (2008). Treatment failure after primary and salvage therapy for prostate cancer: likelihood, patterns of care, and outcomes. *Cancer*, *112*(2), 307-314. https://doi.org/10.1002/cncr.23161

Ahmed, H. U., Arya, M., Freeman, A., & Emberton, M. (2012). Do low-grade and low-volume prostate cancers bear the hallmarks of malignancy? *Lancet Oncol*, *13*(11), e509-517. https://doi.org/10.1016/S1470-2045(12)70388-1

Ahmed, H. U., Kirkham, A., Arya, M., Illing, R., Freeman, A., Allen, C., & Emberton, M. (2009). Is it time to consider a role for MRI before prostate biopsy? *Nat Rev Clin Oncol*, *6*(4), 197-206. https://doi.org/10.1038/nrclinonc.2009.18

Algaba, F., & Montironi, R. (2010). Impact of prostate cancer multifocality on its biology and treatment. *J Endourol*, *24*(5), 799-804. https://doi.org/10.1089/end.2009.0462

Anttinen, M., Blanco Sequeiros, R., Boström, P. J., & Taimen, P. (2022). Evolving imaging methods of prostate cancer and the emergence of magnetic resonance imaging guided ablation techniques. *Front Oncol*, *12*, 1043688. https://doi.org/10.3389/fonc.2022.1043688

Anttinen, M., Mäkelä, P., Nurminen, P., Yli-Pietilä, E., Suomi, V., Sainio, T., Taimen, P., Blanco Sequeiros R., & Boström, P. J. (2020). Palliative MRI-guided transurethral ultrasound ablation for symptomatic locally advanced prostate cancer. *Scand J Urol*, *54*(6), 481-486. https://doi.org/10.1080/21681805.2020.1814857

Anttinen, M., Mäkelä, P., Suomi, V., Kiviniemi, A., Saunavaara, J., Sainio, T., Horte A., Eklund L., Taimen P., Blanco Sequeiros R., & Boström, P. J. (2019). Feasibility of MRI-guided transurethral ultrasound for lesion-targeted ablation of prostate cancer. *Scand J Urol*, *53*(5), 295-302. https://doi.org/10.1080/21681805.2019.1660707

Anttinen, M., Mäkelä, P., Viitala, A., Nurminen, P., Suomi, V., Sainio, T., Saunavaara J., Taimen P., Blanco Sequeiros R., & Boström, P. J. (2020). Salvage Magnetic Resonance Imaging-guided Transurethral Ultrasound Ablation for Localized Radiorecurrent Prostate Cancer: 12-Month Functional and Oncological Results. *Eur Urol Open Sci*, *22*, 79-87. https://doi.org/10.1016/j.euros.2020.10.007

Bakaric, M., Martin, E., S Georgiou, P., T Cox, B., Payne, H., & E Treeby, B. (2018). Experimental study of beam distortion due to fiducial markers during salvage HIFU in the prostate. *J Ther Ultrasound*, *6*, 1. https://doi.org/10.1186/s40349-018-0109-3

Barrett, T., Vargas, H. A., Akin, O., Goldman, D. A., & Hricak, H. (2012). Value of the hemorrhage exclusion sign on T1-weighted prostate MR images for the detection of prostate cancer. *Radiology*, *263*(3), 751-757. https://doi.org/10.1148/radiol.12112100

Bass E. J., Pantovic A., Connor M., Gabe R., Padhani A. R., Rockall A., Sokhi H., Tam H., Winkler M., & Ahmed H. U. (2021). A systematic review and meta-analysis of the diagnostic accuracy of biparametric prostate MRI for prostate cancer in men at risk. *Prostate Cancer Prostatic Dis*, *24*(3), 596-611. https://doi.org/10.1038/s41391-020-00298-w

Bell, K. J., Del Mar, C., Wright, G., Dickinson, J., & Glasziou, P. (2015). Prevalence of incidental prostate cancer: A systematic review of autopsy studies. *Int J Cancer*, *137*(7), 1749-1757. https://doi.org/10.1002/ijc.29538

Berry, S. J., Coffey, D. S., Walsh, P. C., & Ewing, L. L. (1984). The development of human benign prostatic hyperplasia with age. *J Urol*, *132*(3), 474-479. https://doi.org/10.1016/s0022-5347(17)49698-4

Bill-Axelson A., Holmberg L., Garmo H., Taari K., Busch C., Nordling S., Häggman M., Andersson S. O., Andrén O., Steineck G., Adami H. O., & Johansson J. E. (2018). Radical Prostatectomy or Watchful Waiting in Prostate Cancer - 29-Year Follow-up. *N Engl J Med*, *379*(24), 2319-2329. https://doi.org/10.1056/NEJMoa1807801

Blazevski A., Geboers B., Scheltema M. J., Gondoputro W., Doan P., Katelaris A., Agrawal S., Baretto D., Matthews J., Haynes A. M., Delprado W., Shnier R., van den Bos W., Thompson J. E., Lawrentschuk N., & Stricker P.D. (2023). Salvage irreversible electroporation for radio-recurrent prostate cancer - the prospective FIRE trial. *BJU Int*, *131 Suppl 4*, 23-31. https://doi.org/10.1111/bju.15947

Bolla M., Van Tienhoven G., Warde P., Dubois J. B., Mirimanoff R.O., Storme G., Bernier J., Kuten A., Sternberg C., Billiet I., Torecilla J. L., Pfeffer R., Cutajar C. L., Van der Kwast T., & Collette L. (2010). External irradiation with or without long-term androgen suppression for prostate cancer with high metastatic risk: 10-year results of an EORTC randomised study. *Lancet Oncol*, *11*(11), 1066-1073. https://doi.org/10.1016/S1470-2045(10)70223-0

Bomers J. G. R., Cornel E. B., Fütterer J. J., Jenniskens S. F. M., Schaafsma H. E., Barentsz J. O., Sedelaar J. P. M., Hulsbergen-van de Kaa C. A., & Witjes J.A. (2017). MRI-guided focal laser ablation for prostate cancer followed by radical prostatectomy: correlation of treatment effects with imaging. *World J Urol*, *35*(5), 703-711. https://doi.org/10.1007/s00345-016-1924-1

Bonekamp D., Wolf M. B., Roethke M. C., Pahernik S., Hadaschik B. A., Hatiboglu G., Kuru T. H., Popeneciu I. V., Chin J. L., Billia M., Relle J., Hafron J., Nandalur K. R., Staruch R. M., Burtnyk M., Hohenfellner M., & Schlemmer H. P. (2019). Twelve-month prostate volume reduction after MRI-guided transurethral ultrasound ablation of the prostate. *Eur Radiol*, *29*(1), 299-308. https://doi.org/10.1007/s00330-018-5584-y

Borges, R. C., Tourinho-Barbosa, R. R., Glina, S., Macek, P., Mombet, A., Sanchez-Salas, R., & Cathelineau, X. (2021). Impact of Focal Versus Whole Gland Ablation for Prostate Cancer on Sexual Function and Urinary Continence. *J Urol*, *205*(1), 129-136. https://doi.org/10.1097/JU.0000000000001327

Boyes, A., Tang, K., Yaffe, M., Sugar, L., Chopra, R., & Bronskill, M. (2007). Prostate tissue analysis immediately following magnetic resonance imaging guided transurethral ultrasound thermal therapy. *J Urol*, *178*(3 Pt 1), 1080-1085. https://doi.org/10.1016/j.juro.2007.05.011

Brace, C. (2011). Thermal tumor ablation in clinical use. *IEEE Pulse*, *2*(5), 28-38. https://doi.org/10.1109/MPUL.2011.942603

Bradley, W. G. (1993). MR appearance of hemorrhage in the brain. *Radiology*, *189*(1), 15-26. https://doi.org/10.1148/radiology.189.1.8372185

Bratan, F., Niaf, E., Melodelima, C., Chesnais, A. L., Souchon, R., Mège-Lechevallier, F., Colombel, M., & Rouvière, O. (2013). Influence of imaging and histological factors on prostate cancer detection and localisation on multiparametric MRI: a prospective study. *Eur Radiol*, *23*(7), 2019-2029. https://doi.org/10.1007/s00330-013-2795-0

Brierley, J., Gospodarowicz, M. K., & Wittekind, C. (2017). *TNM Classification of Malignant Tumours eighth edition.* Wiley-Blackwell.

Bul M., Zhu X., Valdagni R., Pickles T., Kakehi Y., Rannikko A., Bjartell A., van der Schoot D. K., Cornel E. B., Conti G. N., Boevé E. R., Staerman F., Vis-Maters J. J., Vergunst H., Jaspars J. J., Strölin P., van Muilekom E., Schröder F. H., Bangma C. H., & Roobol M. J. (2013). Active surveillance for low-risk prostate cancer worldwide: the PRIAS study. *Eur Urol*, *63*(4), 597-603. https://doi.org/10.1016/j.eururo.2012.11.005

Burtnyk, M., Hill, T., Cadieux-Pitre, H., & Welch, I. (2015). Magnetic resonance image guided transurethral ultrasound prostate ablation: a preclinical safety and feasibility study with 28-day followup. *J Urol*, *193*(5), 1669-1675. https://doi.org/10.1016/j.juro.2014.11.089

Chade D. C,, Eastham J., Graefen M., Hu J. C., Karnes R. J., Klotz L., Montorsi F., van Poppel H., Scardino P. T., & Shariat S. F. (2012). Cancer control and functional outcomes of salvage radical prostatectomy for radiation-recurrent prostate cancer: a systematic review of the literature. *Eur Urol*, *61*(5), 961-971. https://doi.org/10.1016/j.eururo.2012.01.022

Chopra R., Colquhoun A., Burtnyk M., N'djin W. A., Kobelevskiy I., Boyes A., Siddiqui K., Foster H., Sugar L., Haider M. A., Bronskill M., & Klotz L. (2012). MR imaging-controlled transurethral ultrasound therapy for conformal treatment of prostate tissue: initial feasibility in humans. *Radiology*, *265*(1), 303-313. https://doi.org/10.1148/radiol.12112263

Chopra, R., Tang, K., Burtnyk, M., Boyes, A., Sugar, L., Appu, S., Klotz L., & Bronskill, M. (2009). Analysis of the spatial and temporal accuracy of heating in the prostate gland using transurethral ultrasound therapy and active MR temperature feedback. *Phys Med Biol*, *54*(9), 2615-2633. https://doi.org/10.1088/0031-9155/54/9/002

Chu, K. F., & Dupuy, D. E. (2014). Thermal ablation of tumours: biological mechanisms and advances in therapy. *Nat Rev Cancer*, *14*(3), 199-208. https://doi.org/10.1038/nrc3672

Cooperberg, M. R., Moul, J. W., & Carroll, P. R. (2005). The changing face of prostate cancer. *J Clin Oncol*, *23*(32), 8146-8151. https://doi.org/10.1200/JCO.2005.02.9751

Corkum, M. T., Mendez, L. C., Chin, J., D'Souza, D., Boldt, R. G., & Bauman, G. S. (2020). A Novel Salvage Option for Local Failure in Prostate Cancer, Reirradiation Using External Beam or Stereotactic Radiation Therapy: Systematic Review and Meta-Analysis. *Adv Radiat Oncol*, *5*(5), 965-977. https://doi.org/10.1016/j.adro.2020.04.022

Crouzet, S., Blana, A., Murat, F. J., Pasticier, G., Brown, S. C. W., Conti, G. N., Ganzer R., Chapet O., Gelet A., Chaussy C. G., Robertson C. N., Thuroff S., & Ward, J. F. (2017). Salvage high-intensity focused ultrasound (HIFU) for locally recurrent prostate cancer after failed radiation therapy: Multi-institutional analysis of 418 patients. *BJU Int*, *119*(6), 896-904. https://doi.org/10.1111/bju.13766

de Rooij, M., Hamoen, E. H., Witjes, J. A., Barentsz, J. O., & Rovers, M. M. (2016). Accuracy of Magnetic Resonance Imaging for Local Staging of Prostate Cancer: A Diagnostic Meta-analysis. *Eur Urol*, *70*(2), 233-245. https://doi.org/10.1016/j.eururo.2015.07.029

Devlin, C. M., Simms, M. S., & Maitland, N. J. (2021). Benign prostatic hyperplasia - what do we know? *BJU Int*, *127*(4), 389-399. https://doi.org/10.1111/bju.15229

Donaldson, I. A., Alonzi, R., Barratt, D., Barret, E., Berge, V., Bott, S., Bottomley D., Eggener S., Ehdaie B., Emberton M., Hindley R., Leslie T., Miners A., McCartan N., Moore C. M., Pinto P., Polascik T. J., Simmons L., van der Meulen J., Villers A., Willis S., & Ahmed, H. U. (2015). Focal therapy: patients, interventions, and outcomes--a report from a consensus meeting. *Eur Urol*, *67*(4), 771-777. https://doi.org/10.1016/j.eururo.2014.09.018

Drost, F. H., Osses, D. F., Nieboer, D., Steyerberg, E. W., Bangma, C. H., Roobol, M. J., & Schoots, I. G. (2019). Prostate MRI, with or without MRI-targeted biopsy, and systematic biopsy for detecting prostate cancer. *Cochrane Database Syst Rev*, *4*(4), CD012663. https://doi.org/10.1002/14651858.CD012663.pub2

Elterman, D., Li, W., Hatiboglu, G., Relle, J., Zorn, K. C., Bhojani, N., & Chin, J. (2021). Relief of Lower Urinary Tract Symptoms After MRI-Guided Transurethral Ultrasound Ablation for Localized Prostate Cancer: Subgroup Analyses in Patients with Concurrent Cancer and Benign Prostatic Hyperplasia. *J Endourol*, *35*(4), 497-505. https://doi.org/10.1089/end.2020.0511

Epstein, J. I., Allsbrook, W. C., Amin, M. B., Egevad, L. L., & Committee, I. G. (2005). The 2005 International Society of Urological Pathology (ISUP) Consensus Conference on Gleason Grading of Prostatic Carcinoma. *Am J Surg Pathol*, *29*(9), 1228-1242. https://doi.org/10.1097/01.pas.0000173646.99337.b1

Epstein, J. I., Egevad, L., Amin, M. B., Delahunt, B., Srigley, J. R., Humphrey, P. A., & Committee, G. (2016). The 2014 International Society of Urological Pathology (ISUP) Consensus Conference on Gleason Grading of Prostatic Carcinoma: Definition of Grading Patterns and Proposal for a New Grading System. *Am J Surg Pathol*, *40*(2), 244-252. https://doi.org/10.1097/PAS.0000000000000530

Fan, X. (1995). Evaluation of accuracy of a theoretical model for predicting the necrosed tissue volume during focused ultrasound surgery. *IEEE transactions on ultrasonics, ferroelectrics, and frequency control*, *42*(2), 182-187.

Fendler, W. P., Eiber, M., Beheshti, M., Bomanji, J., Calais, J., Ceci, F., Cho S. Y., Fanti S., Giesel F. L., Goffin K., Haberkorn U., Jacene H., Koo P. J., Kopka K., Krause B. J., Lindenberg L., Marcus C., Mottaghy F. M., Oprea-Lager D. E., Osborne J. R., Piert M., Rowe S. P., Schöder H., Wan S., Wester H. J., Hope T. A., & Herrmann, K. (2023). PSMA PET/CT: joint EANM procedure guideline/SNMMI procedure standard for prostate cancer imaging 2.0. *Eur J Nucl Med Mol Imaging*, *50*(5), 1466-1486. https://doi.org/10.1007/s00259-022-06089-w

Fenton, J. J., Weyrich, M. S., Durbin, S., Liu, Y., Bang, H., & Melnikow, J. (2018). Prostate-Specific Antigen-Based Screening for Prostate Cancer: Evidence Report and Systematic Review for the US Preventive Services Task Force. *JAMA*, *319*(18), 1914-1931. https://doi.org/10.1001/jama.2018.3712

Feuerlein, S., Pauls, S., Juchems, M. S., Stuber, T., Hoffmann, M. H., Brambs, H. J., & Ernst, A. S. (2009). Pitfalls in abdominal diffusion-weighted imaging: how predictive is restricted water diffusion for malignancy. *AJR Am J Roentgenol*, *193*(4), 1070-1076. https://doi.org/10.2214/AJR.08.2093

Fütterer, J. J., Briganti, A., De Visschere, P., Emberton, M., Giannarini, G., Kirkham, A., Taneja S. S., Thoeny H., & Villers, A. (2015). Can Clinically Significant Prostate Cancer Be Detected with Multiparametric Magnetic Resonance Imaging? A Systematic Review of the Literature. *Eur Urol*, *68*(6), 1045-1053. https://doi.org/10.1016/j.eururo.2015.01.013

Gandaglia, G., Abdollah, F., Schiffmann, J., Trudeau, V., Shariat, S. F., Kim, S. P., Perrotte P., Montorsi F., Briganti A., Trinh Q. D., Karakiewicz P. I., & Sun, M. (2014). Distribution of metastatic sites in patients with prostate cancer: A population-based analysis. *Prostate*, *74*(2), 210-216. https://doi.org/10.1002/pros.22742

Gaur, S., & Turkbey, B. (2018). Prostate MR Imaging for Posttreatment Evaluation and Recurrence. *Radiol Clin North Am*, *56*(2), 263-275. https://doi.org/10.1016/j.rcl.2017.10.008

Georgiou, P. S., Jaros, J., Payne, H., Allen, C., Shah, T. T., Ahmed, H. U., Gibson E., Barratt D., & Treeby, B. E. (2017). Beam distortion due to gold fiducial markers during salvage high-intensity focused ultrasound in the prostate. *Med Phys*, *44*(2), 679-693. https://doi.org/10.1002/mp.12044

Ghafoor, S., Becker, A. S., Stocker, D., Barth, B. K., Eberli, D., Donati, O. F., & Vargas, H. A. (2020). Magnetic resonance imaging of the prostate after focal therapy with high-intensity focused ultrasound. *Abdom Radiol (NY)*, *45*(11), 3882-3895. https://doi.org/10.1007/s00261-020-02577-5

Giganti, F., Dickinson, L., Orczyk, C., Haider, A., Freeman, A., Emberton, M., Allen C., & Moore, C. M. (2023). Prostate Imaging after Focal Ablation (PI-FAB): A Proposal for a Scoring System for Multiparametric MRI of the Prostate After Focal Therapy. *Eur Urol Oncol*, *6*(6), 629-634. https://doi.org/10.1016/j.euo.2023.04.007

Gilbert, S. M., Dunn, R. L., Miller, D. C., Montgomery, J. S., Skolarus, T. A., Weizer, A. Z., Wood D. P. Jr., & Hollenbeck, B. K. (2017). Functional Outcomes Following Nerve Sparing Prostatectomy Augmented with Seminal Vesicle Sparing Compared to Standard Nerve Sparing Prostatectomy: Results from a Randomized Controlled Trial. *J Urol*, *198*(3), 600-607. https://doi.org/10.1016/j.juro.2017.03.133

Gleason, D. F. (1966). Classification of prostatic carcinomas. *Cancer Chemother Rep*, *50*(3), 125-128.

Gratzke, C., Bachmann, A., Descazeaud, A., Drake, M. J., Madersbacher, S., Mamoulakis, C., Oelke M., Tikkinen K. A. O., & Gravas, S. (2015). EAU Guidelines on the Assessment of Non-

neurogenic Male Lower Urinary Tract Symptoms including Benign Prostatic Obstruction. *Eur Urol*, *67*(6), 1099-1109. https://doi.org/10.1016/j.eururo.2014.12.038

Haglind, E., Carlsson, S., Stranne, J., Wallerstedt, A., Wilderäng, U., Thorsteinsdottir, T., Lagerkvist M., Damber J. E., Bjartell A., Hugosson J., Wiklund P., & Steineck G. (2015). Urinary Incontinence and Erectile Dysfunction After Robotic Versus Open Radical Prostatectomy: A Prospective, Controlled, Nonrandomised Trial. *Eur Urol*, *68*(2), 216-225. https://doi.org/10.1016/j.eururo.2015.02.029

Hambrock, T., Somford, D. M., Huisman, H. J., van Oort, I. M., Witjes, J. A., Hulsbergen-van de Kaa, C. A., Scheenen T., & Barentsz, J. O. (2011). Relationship between apparent diffusion coefficients at 3.0-T MR imaging and Gleason grade in peripheral zone prostate cancer. *Radiology*, *259*(2), 453-461. https://doi.org/10.1148/radiol.11091409

Hamdy, F. C., Donovan, J. L., Lane, J. A., Mason, M., Metcalfe, C., Holding, P., Davis M., Peters T. J., Turner E. L., Martin R. M., Oxley J., Robinson M., Staffurth J., Walsh E., Bollina P., Catto J., Doble A., Doherty A., Gillatt D., Kockelbergh R., Kynaston H., Paul A., Powell P., Prescott S., Rosario D. J., Rowe E., & Neal D. E. (2016). 10-Year Outcomes after Monitoring, Surgery, or Radiotherapy for Localized Prostate Cancer. *N Engl J Med*, *375*(15), 1415-1424. https://doi.org/10.1056/NEJMoa1606220

Han, E. A., Nandalur, K. R., Morgan, M. A., Arora, S. S., Loening, A. M., Bivalacqua, T. J., & Sundaram, K. M. (2023). MRI of Benign Prostatic Hyperplasia: Important Pre- and Posttherapeutic Considerations. *Radiographics*, *43*(5), e220096. https://doi.org/10.1148/rg.220096

Han, K. R., & Belldegrun, A. S. (2004). Third-generation cryosurgery for primary and recurrent prostate cancer. *BJU Int*, *93*(1), 14-18. https://doi.org/10.1111/j.1464-410x.2004.04547.x

Hayes, J. H., & Barry, M. J. (2014). Screening for prostate cancer with the prostate-specific antigen test: a review of current evidence. *JAMA*, *311*(11), 1143-1149. https://doi.org/10.1001/jama.2014.2085

Hazle, J. D., Diederich, C. J., Kangasniemi, M., Price, R. E., Olsson, L. E., & Stafford, R. J. (2002). MRI-guided thermal therapy of transplanted tumors in the canine prostate using a directional transurethral ultrasound applicator. *J Magn Reson Imaging*, *15*(4), 409-417. https://doi.org/10.1002/jmri.10076

Hofman, M. S., Lawrentschuk, N., Francis, R. J., Tang, C., Vela, I., Thomas, P., Rutherford N., Martin J. M., Frydenberg M., Shakher R., Wong L. M., Taubman K., Ting Lee S., Hsiao E., Roach P., Nottage M., Kirkwood I., Hayne D., Link E., Marusic P., Matera A., Herschtal A., Iravani A., Hicks R. J., Williams S., & Murphy D. G. (2020). Prostate-specific membrane antigen PET-CT in patients with high-risk prostate cancer before curative-intent surgery or radiotherapy (proPSMA): a prospective, randomised, multicentre study. *Lancet*, *395*(10231), 1208-1216. https://doi.org/10.1016/S0140-6736(20)30314-7

Hopstaken, J. S., Bomers, J. G. R., Sedelaar, M. J. P., Valerio, M., Fütterer, J. J., & Rovers, M. M. (2022). An Updated Systematic Review on Focal Therapy in Localized Prostate Cancer: What Has Changed over the Past 5 Years? *Eur Urol*, *81*(1), 5-33. https://doi.org/10.1016/j.eururo.2021.08.005

Huber, P. M., Afzal, N., Arya, M., Boxler, S., Dudderidge, T., Emberton, M., Guillaumier S., Hindley R. G., Hosking-Jervis F., Leemann L., Lewi H., McCartan N., Moore C. M., Nigam R., Odgen C., Persad R., Virdi J., Winkler M., & Ahmed, H. U. (2021). Focal HIFU therapy for anterior compared to posterior prostate cancer lesions. *World J Urol*, *39*(4), 1115-1119. https://doi.org/10.1007/s00345-020-03297-7

Hötker, A. M., Meier, A., Mazaheri, Y., Zheng, J., Capanu, M., Chaim, J., Sosa R., Coleman J., Hricak H., & Akin, O. (2019). Temporal changes in MRI appearance of the prostate after focal ablation. *Abdom Radiol (NY)*, *44*(1), 272-278. https://doi.org/10.1007/s00261-018-1715-9

Hövels, A. M., Heesakkers, R. A., Adang, E. M., Jager, G. J., Strum, S., Hoogeveen, Y. L., Severens J. L., & Barentsz, J. O. (2008). The diagnostic accuracy of CT and MRI in the staging of pelvic

lymph nodes in patients with prostate cancer: a meta-analysis. *Clin Radiol*, *63*(4), 387-395. https://doi.org/10.1016/j.crad.2007.05.022

Iczkowski, K. A., Paner, G. P., & Van der Kwast, T. (2018). The New Realization About Cribriform Prostate Cancer. *Adv Anat Pathol*, *25*(1), 31-37. https://doi.org/10.1097/PAP.0000000000000168

Ilic, D., Djulbegovic, M., Jung, J. H., Hwang, E. C., Zhou, Q., Cleves, A., Agoritsas T., & Dahm, P. (2018). Prostate cancer screening with prostate-specific antigen (PSA) test: a systematic review and meta-analysis. *BMJ*, *362*, k3519. https://doi.org/10.1136/bmj.k3519

Ishihara, Y., Calderon, A., Watanabe, H., Okamoto, K., Suzuki, Y., & Kuroda, K. (1995). A precise and fast temperature mapping using water proton chemical shift. *Magn Reson Med*, *34*(6), 814-823. https://doi.org/10.1002/mrm.1910340606

Jambor, I., Verho, J., Ettala, O., Knaapila, J., Taimen, P., Syvänen, K. T., Kiviniemi A., Kähkönen E., Perez I. M., Seppänen M., Rannikko A., Oksanen O., Riikonen J., Vimpeli S. M., Kauko T., Merisaari H., Kallajoki M., Mirtti T., Lamminen T., Saunavaara J., Aronen H. J., & Boström, P. J. (2019). Validation of IMPROD biparametric MRI in men with clinically suspected prostate cancer: A prospective multi-institutional trial. *PLoS Med*, *16*(6), e1002813. https://doi.org/10.1371/journal.pmed.1002813

Johnson, D. C., Raman, S. S., Mirak, S. A., Kwan, L., Bajgiran, A. M., Hsu, W., Maehara C. K., Ahuja P., Faiena I., Pooli A., Salmasi A., Sisk A., Felker E. R., Lu D. S. K., & Reiter, R. E. (2019). Detection of Individual Prostate Cancer Foci via Multiparametric Magnetic Resonance Imaging. *Eur Urol*, *75*(5), 712-720. https://doi.org/10.1016/j.eururo.2018.11.031

Jones, C. U., Hunt, D., McGowan, D. G., Amin, M. B., Chetner, M. P., Bruner, D. W., Leibenhaut M. H., Husain S. M., Rotman M., Souhami L., Sandler H. M., & Shipley, W. U. (2011). Radiotherapy and short-term androgen deprivation for localized prostate cancer. *N Engl J Med*, *365*(2), 107-118. https://doi.org/10.1056/NEJMoa1012348

Jonsson, J. H., Garpebring, A., Karlsson, M. G., & Nyholm, T. (2012). Internal fiducial markers and susceptibility effects in MRI-simulation and measurement of spatial accuracy. *Int J Radiat Oncol Biol Phys*, *82*(5), 1612-1618. https://doi.org/10.1016/j.ijrobp.2011.01.046

Karavitakis, M., Winkler, M., Abel, P., Livni, N., Beckley, I., & Ahmed, H. U. (2011). Histological characteristics of the index lesion in whole-mount radical prostatectomy specimens: implications for focal therapy. *Prostate Cancer Prostatic Dis*, *14*(1), 46-52. https://doi.org/10.1038/pcan.2010.16

Kasivisvanathan, V., Rannikko, A. S., Borghi, M., Panebianco, V., Mynderse, L. A., Vaarala, M. H., Briganti, A., Budäus L., Hellawell, G., Hindley, R. G., Roobol, M. J., Eggener, S., Ghei, M., Villers, A., Bladou, F., Villeirs, G. M., Virdi, J., Boxler, S., Robert, G., Singh, P. B., Venderink, W., Hadaschik, B. A., Ruffion, A., Hu, J. C., Margolis, D., Crouzet, S., Klotz, L., Taneja, S. S., Pinto, P., Gill, I., Allen, C., Giganti, F., Freeman, A., Morris, S., Punwani, S., Williams, N. R., Brew-Graves, C., Deeks, J., Takwoingi, Y., Emberton, M., & Moore, C. M. (2018). MRI-Targeted or Standard Biopsy for Prostate-Cancer Diagnosis. *N Engl J Med*, *378*(19), 1767-1777. https://doi.org/10.1056/NEJMoa1801993

Kim, C. K., Park, B. K., Lee, H. M., Kim, S. S., & Kim, E. (2008). MRI techniques for prediction of local tumor progression after high-intensity focused ultrasonic ablation of prostate cancer. *AJR Am J Roentgenol*, *190*(5), 1180-1186. https://doi.org/10.2214/AJR.07.2924

Kirkham, A. P., Emberton, M., Hoh, I. M., Illing, R. O., Freeman, A. A., & Allen, C. (2008). MR imaging of prostate after treatment with high-intensity focused ultrasound. *Radiology*, *246*(3), 833-844. https://doi.org/10.1148/radiol.2463062080

Klotz, L. (2022). Overdiagnosis in urologic cancer : For World Journal of Urology Symposium on active surveillance in prostate and renal cancer. *World J Urol*, *40*(1), 1-8. https://doi.org/10.1007/s00345-020-03523-2

Klotz, L., Pavlovich, C. P., Chin, J., Hatiboglu, G., Koch, M., Penson, D., Raman S., Oto A., Fütterer J., Serrallach M., Relle J., Lotan Y., Heidenreich A., Bonekamp D., Haider M., Tirkes T., Arora S., Macura K. J., Costa D. N., Persigehl T., Pantuck A. J., Bomers J., Burtnyk M., Staruch R., &

Eggener S. (2021). Magnetic resonance imaging-guided transurethral ultrasound ablation of prostate cancer. *The Journal of urology*, *205*(3), 769-779.

Koh, D. M., & Collins, D. J. (2007). Diffusion-weighted MRI in the body: applications and challenges in oncology. *AJR Am J Roentgenol*, *188*(6), 1622-1635. https://doi.org/10.2214/AJR.06.1403

Kuriyama, M., Wang, M. C., Lee, C. I., Papsidero, L. D., Killian, C. S., Inaji, H., Slack N. H., Nishiura T., Murphy G. P., & Chu, T. M. (1981). Use of human prostate-specific antigen in monitoring prostate cancer. *Cancer Res*, *41*(10), 3874-3876.

Labbate, C. V., Klotz, L., Morrow, M., Cooperberg, M., Esserman, L., & Eggener, S. E. (2023). Focal Therapy for Prostate Cancer: Evolutionary Parallels to Breast Cancer Treatment. *J Urol*, *209*(1), 49-57. https://doi.org/10.1097/JU.0000000000002972

Lauterbur, P. C. (1973). Image formation by induced local interactions: examples employing nuclear magnetic resonance. *nature*, *242*(5394), 190-191.

Lee, J. Y., Chang, I. H., Moon, Y. T., Kim, K. D., Myung, S. C., Kim, T. H., & Lee, J. B. (2011). Effect of Prostate Biopsy Hemorrhage on MRDW and MRS Imaging. *Korean J Urol*, *52*(10), 674-680. https://doi.org/10.4111/kju.2011.52.10.674

Light, A., Mayor, N., Cullen, E., Kirkham, A., Padhani, A. R., Arya, M., Bomers J. G. R., Dudderidge T., Ehdaie B., Freeman A., Guillaumier S., Hindley R., Lakhani A., Pendse D., Punwani S., Rastinehad A. R., Rouvière O., Sanchez-Salas R., Schoots I. G., Sokhi H. K., Tam H., Tempany C. M., Valerio M., Verma S., Villeirs G., van der Meulen J., Ahmed H. U., & Shah, T. T. (2024). The Transatlantic Recommendations for Prostate Gland Evaluation with Magnetic Resonance Imaging After Focal Therapy (TARGET): A Systematic Review and International Consensus Recommendations. *Eur Urol*. https://doi.org/10.1016/j.eururo.2024.02.001

Lin, S. P., & Brown, J. J. (2007). MR contrast agents: physical and pharmacologic basics. *J Magn Reson Imaging*, *25*(5), 884-899. https://doi.org/10.1002/jmri.20955

Lindner, U., Lawrentschuk, N., & Trachtenberg, J. (2010). Focal laser ablation for localized prostate cancer. *J Endourol*, *24*(5), 791-797. https://doi.org/10.1089/end.2009.0440

Lindner, U., Lawrentschuk, N., Weersink, R. A., Davidson, S. R., Raz, O., Hlasny, E., Langer D. L., Gertner M. R., Van der Kwast T., Haider M. A., & Trachtenberg, J. (2010). Focal laser ablation for prostate cancer followed by radical prostatectomy: validation of focal therapy and imaging accuracy. *Eur Urol*, *57*(6), 1111-1114. https://doi.org/10.1016/j.eururo.2010.03.008

Lotte, R., Lafourcade, A., Mozer, P., Conort, P., Barret, E., Comperat, E., Ezziane M., de Guibert P. J., Tavolaro S., Belin L., Boudghene F., Lucidarme O., & Renard-Penna, R. (2018). Multiparametric MRI for Suspected Recurrent Prostate Cancer after HIFU:Is DCE still needed? *Eur Radiol*, *28*(9), 3760-3769. https://doi.org/10.1007/s00330-018-5352-z

Lovegrove, C. E., Peters, M., Guillaumier, S., Arya, M., Afzal, N., Dudderidge, T., Hosking-Jervis F., Hindley R. G., Lewi H., McCartan N., Moore C. M., Nigam R., Ogden C., Persad R., Virdi J., Winkler M., Emberton M., Ahmed H. U., Shah T. T., & Minhas, S. (2020). Evaluation of functional outcomes after a second focal high-intensity focused ultrasonography (HIFU) procedure in men with primary localized, non-metastatic prostate cancer: results from the HIFU Evaluation and Assessment of Treatment (HEAT) registry. *BJU Int*, *125*(6), 853-860. https://doi.org/10.1111/bju.15004

Lumiani, A., Samun, D., Sroka, R., & Muschter, R. (2021). Single center retrospective analysis of fifty-two prostate cancer patients with customized MR-guided transurethral ultrasound ablation (TULSA). *Urol Oncol*, *39*(12), 830.e839-830.e816. https://doi.org/10.1016/j.urolonc.2021.04.022

Madersbacher, S., & Marberger, M. (2003). High-energy shockwaves and extracorporeal high-intensity focused ultrasound. *J Endourol*, *17*(8), 667-672. https://doi.org/10.1089/089277903322518680

Marra, G., Valerio, M., Emberton, M., Heidenreich, A., Crook, J. M., Bossi, A., & Pisters, L. L. (2019). Salvage Local Treatments After Focal Therapy for Prostate Cancer. *Eur Urol Oncol*, *2*(5), 526-538. https://doi.org/10.1016/j.euo.2019.03.008

McDannold, N. J., King, R. L., Jolesz, F. A., & Hynynen, K. H. (2000). Usefulness of MR imaging-derived thermometry and dosimetry in determining the threshold for tissue damage induced by

thermal surgery in rabbits. *Radiology*, *216*(2), 517-523. https://doi.org/10.1148/radiology.216.2.r00au42517

McDougal, W. S., Wein, A. J., Kavoussi, L. R., Partin, A. W., & Peters, C. A. (2015). *Campbell-Walsh Urology 11th Edition Review E-Book*. Elsevier Health Sciences.

McNeal, J. E. (1978). Origin and evolution of benign prostatic enlargement. *Invest Urol*, *15*(4), 340-345.

McNeal, J. E. (1981). The zonal anatomy of the prostate. *Prostate*, *2*(1), 35-49. https://doi.org/10.1002/pros.2990020105

McNeal, J. E. (1988). Normal histology of the prostate. *Am J Surg Pathol*, *12*(8), 619-633. https://doi.org/10.1097/00000478-198808000-00003

McNeal, J. E., Redwine, E. A., Freiha, F. S., & Stamey, T. A. (1988). Zonal distribution of prostatic adenocarcinoma. Correlation with histologic pattern and direction of spread. *Am J Surg Pathol*, *12*(12), 897-906. https://doi.org/10.1097/00000478-198812000-00001

Mease, R. C., Foss, C. A., & Pomper, M. G. (2013). PET imaging in prostate cancer: focus on prostate-specific membrane antigen. *Curr Top Med Chem*, *13*(8), 951-962. https://doi.org/10.2174/1568026611313080008

Mendez, M. H., Passoni, N. M., Pow-Sang, J., Jones, J. S., & Polascik, T. J. (2015). Comparison of Outcomes Between Preoperatively Potent Men Treated with Focal Versus Whole Gland Cryotherapy in a Matched Population. *J Endourol*, *29*(10), 1193-1198. https://doi.org/10.1089/end.2014.0881

Morani, A. C., Elsayes, K. M., Liu, P. S., Weadock, W. J., Szklaruk, J., Dillman, J. R., Khan A., Chenevert T. L., & Hussain, H. K. (2013). Abdominal applications of diffusion-weighted magnetic resonance imaging: Where do we stand. *World J Radiol*, *5*(3), 68-80. https://doi.org/10.4329/wjr.v5.i3.68

Moris, L., Gandaglia, G., Vilaseca, A., Van den Broeck, T., Briers, E., De Santis, M., Gillessen S., Grivas N., O'Hanlon S., Henry A., Lam T. B., Lardas M., Mason M., Oprea-Lager D., Ploussard G., Rouviere O., Schoots I. G., van der Poel H., Wiegel T., Willemse P. P., Yuan C. Y., Grummet J. P., Tilki D., van den Bergh R. C. N., Cornford P., & Mottet, N. (2022). Evaluation of Oncological Outcomes and Data Quality in Studies Assessing Nerve-sparing Versus Non-Nerve-sparing Radical Prostatectomy in Nonmetastatic Prostate Cancer: A Systematic Review. *Eur Urol Focus*, *8*(3), 690-700. https://doi.org/10.1016/j.euf.2021.05.009

Mottet, N., Cornford, P., & Van Den Bergh, R. C. N. (2022). ESUR-ISUP-SIOG guidelines on prostate cancer. *EAU Guidelines Office*.

Mougenot, C., & Moonen, C. (2017). Magnetic Resonance-guided High Intensity Focused Ultrasound in the presence of biopsy markers. *J Ther Ultrasound*, *5*, 25. https://doi.org/10.1186/s40349-017-0103-1

Mueller-Lisse, U. G., Heuck, A. F., Schneede, P., Muschter, R., Scheidler, J., Hofstetter, A. G., & Reiser, M. F. (1996). Postoperative MRI in patients undergoing interstitial laser coagulation thermotherapy of benign prostatic hyperplasia. *J Comput Assist Tomogr*, *20*(2), 273-278. https://doi.org/10.1097/00004728-199603000-00019

Mukkala, A. N., Song, J. B., Lee, M., Boasie, A., Irish, J., Finelli, A., & Wei, A. C. (2021). A systematic review and meta-analysis of unplanned hospital visits and re-admissions following radical prostatectomy for prostate cancer. *Can Urol Assoc J*, *15*(10), E531-E544. https://doi.org/10.5489/cuaj.6931

Muller, B. G., van den Bos, W., Brausi, M., Fütterer, J. J., Ghai, S., Pinto, P. A., Popeneciu I. V., de Reijke T. M., Robertson C., de la Rosette J. J., Scionti S., Turkbey B., Wijkstra H., Ukimura O., & Polascik, T. J. (2015). Follow-up modalities in focal therapy for prostate cancer: results from a Delphi consensus project. *World J Urol*, *33*(10), 1503-1509. https://doi.org/10.1007/s00345-014-1475-2

Muller, N., & Reiter, R. C. (1965). Temperature dependence of chemical shifts of protons in hydrogen bonds. *The Journal of Chemical Physics*, *42*(9), 3265-3269.

Nikfarjam, M., Muralidharan, V., & Christophi, C. (2005). Mechanisms of focal heat destruction of liver tumors. *J Surg Res*, *127*(2), 208-223. https://doi.org/10.1016/j.jss.2005.02.009

O'Neill, A. G., Jain, S., Hounsell, A. R., & O'Sullivan, J. M. (2016). Fiducial marker guided prostate radiotherapy: a review. *Br J Radiol*, *89*(1068), 20160296. https://doi.org/10.1259/bjr.20160296

Onur, R., Littrup, P. J., Pontes, J. E., & Bianco, F. J. (2004). Contemporary impact of transrectal ultrasound lesions for prostate cancer detection. *J Urol*, *172*(2), 512-514. https://doi.org/10.1097/01.ju.0000131621.61732.6b

Osman, S. O. S., Russell, E., King, R. B., Crowther, K., Jain, S., McGrath, C., Hounsell A. R., Prise K. M., & McGarry, C. K. (2019). Fiducial markers visibility and artefacts in prostate cancer radiotherapy multi-modality imaging. *Radiat Oncol*, *14*(1), 237. https://doi.org/10.1186/s13014-019-1447-1

Panebianco, V., Barchetti, G., Simone, G., Del Monte, M., Ciardi, A., Grompone, M. D., Campa R., Indino E. L., Barchetti F., Sciarra A., Leonardo C., Gallucci M., & Catalano, C. (2018). Negative Multiparametric Magnetic Resonance Imaging for Prostate Cancer: What's Next? *Eur Urol*, *74*(1), 48-54. https://doi.org/10.1016/j.eururo.2018.03.007

Panebianco, V., Villeirs, G., Weinreb, J. C., Turkbey, B. I., Margolis, D. J., Richenberg, J., Schoots I. G., Moore C. M., Futterer J., Macura K. J., Oto A., Bittencourt L. K., Haider M. A., Salomon G., Tempany C. M., Padhani A. R., & Barentsz, J. O. (2021). Prostate Magnetic Resonance Imaging for Local Recurrence Reporting (PI-RR): International Consensus -based Guidelines on Multiparametric Magnetic Resonance Imaging for Prostate Cancer Recurrence after Radiation Therapy and Radical Prostatectomy. *Eur Urol Oncol*, *4*(6), 868-876. https://doi.org/10.1016/j.euo.2021.01.003

Parimi, V., Goyal, R., Poropatich, K., & Yang, X. J. (2014). Neuroendocrine differentiation of prostate cancer: a review. *Am J Clin Exp Urol*, *2*(4), 273-285.

Patel, P., Mathew, M. S., Trilisky, I., & Oto, A. (2018). Multiparametric MR Imaging of the Prostate after Treatment of Prostate Cancer. *Radiographics*, *38*(2), 437-449. https://doi.org/10.1148/rg.2018170147

Perera, M., Papa, N., Roberts, M., Williams, M., Udovicich, C., Vela, I., Christidis D., Bolton D., Hofman M. S., Lawrentschuk N., & Murphy, D. G. (2020). Gallium-68 Prostate-specific Membrane Antigen Positron Emission Tomography in Advanced Prostate Cancer-Updated Diagnostic Utility, Sensitivity, Specificity, and Distribution of Prostate-specific Membrane Antigen-avid Lesions: A Systematic Review and Meta-analysis. *Eur Urol*, *77*(4), 403-417. https://doi.org/10.1016/j.eururo.2019.01.049

Pirola, G. M., Castellani, D., Orecchia, L., Giulioni, C., Gubbiotti, M., Rubilotta, E., Maggi M., Teoh J. Y., Gauhar V., & Naselli, A. (2023). Transperineal US-MRI Fusion-Guided Biopsy for the Detection of Clinical Significant Prostate Cancer: A Systematic Review and Meta-Analysis Comparing Cognitive and Software-Assisted Technique. *Cancers (Basel)*, *15*(13). https://doi.org/10.3390/cancers15133443

Ploussard, G., Manceau, C., Beauval, J. B., Lesourd, M., Almeras, C., Gautier, J. R., Loison G., Salin A., Soulié M., Tollon C., Malavaud B., & Roumiguié, M. (2020). Decreased accuracy of the prostate cancer EAU risk group classification in the era of imaging-guided diagnostic pathway: proposal for a new classification based on MRI-targeted biopsies and early oncologic outcomes after surgery. *World J Urol*, *38*(10), 2493-2500. https://doi.org/10.1007/s00345-019-03053-6

Polascik, T. J., Mayes, J. M., Sun, L., Madden, J. F., Moul, J. W., & Mouraviev, V. (2008). Pathologic stage T2a and T2b prostate cancer in the recent prostate-specific antigen era: implications for unilateral ablative therapy. *Prostate*, *68*(13), 1380-1386. https://doi.org/10.1002/pros.20804

Pound, C. R., Partin, A. W., Eisenberger, M. A., Chan, D. W., Pearson, J. D., & Walsh, P. C. (1999). Natural history of progression after PSA elevation following radical prostatectomy. *JAMA*, *281*(17), 1591-1597. https://doi.org/10.1001/jama.281.17.1591

Purysko, A. S., Rosenkrantz, A. B., Barentsz, J. O., Weinreb, J. C., & Macura, K. J. (2016). PI-RADS Version 2: A Pictorial Update. *Radiographics*, *36*(5), 1354-1372. https://doi.org/10.1148/rg.2016150234

Quesson, B., de Zwart, J. A., & Moonen, C. T. (2000). Magnetic resonance temperature imaging for guidance of thermotherapy. J Magn Reson Imaging, 12(4), 525-533. https://doi.org/10.1002/1522-2586(200010)12:4<525::aid-jmri3>3.0.co;2-v

Rai, S., Srivastava, A., Sooriakumaran, P., & Tewari, A. (2012). Advances in imaging the neurovascular bundle. *Curr Opin Urol*, *22*(2), 88-96. https://doi.org/10.1097/MOU.0b013e3283501826

Ramsay, C. R., Adewuyi, T. E., Gray, J., Hislop, J., Shirley, M. D., Jayakody, S., MacLennan G., Fraser C., MacLennan S., Brazzelli M., N'Dow J., Pickard R., Robertson C., Rothnie K., Rushton S. P., Vale L., & Lam, T. B. (2015). Ablative therapy for people with localised prostate cancer: a systematic review and economic evaluation. *Health Technol Assess*, *19*(49), 1-490. https://doi.org/10.3310/hta19490

Rasing, M., van Son, M., Moerland, M., de Keizer, B., Wessels, F., Jonges, T., van de Pol S., Eppinga W., Noteboom J., Lagendijk J., van der Voort van Zijp J., & Peters, M. (2022). Value of Targeted Biopsies and Combined PSMA PET/CT and mp-MRI Imaging in Locally Recurrent Prostate Cancer after Primary Radiotherapy. *Cancers (Basel)*, *14*(3). https://doi.org/10.3390/cancers14030781

Resnick, M. J., Koyama, T., Fan, K. H., Albertsen, P. C., Goodman, M., Hamilton, A. S., Hoffman R. M., Potosky A. L., Stanford J. L., Stroup A. M., Van Horn R. L., & Penson, D. F. (2013). Long-term functional outcomes after treatment for localized prostate cancer. *N Engl J Med*, *368*(5), 436-445. https://doi.org/10.1056/NEJMoa1209978

Richie, J. P., Catalona, W. J., Ahmann, F. R., Hudson, M. A., Scardino, P. T., Flanigan, R. C., deKernion J. B., Ratliff T. L., Kavoussi L. R., Dalkin B. L., Waters W. B., MacFarlane M. T., & Southwick, P. C. (1993). Effect of patient age on early detection of prostate cancer with serum prostate-specific antigen and digital rectal examination. *Urology*, *42*(4), 365-374. https://doi.org/10.1016/0090-4295(93)90359-i

Rieke, V., & Butts Pauly, K. (2008). MR thermometry. *J Magn Reson Imaging*, *27*(2), 376-390. https://doi.org/10.1002/jmri.21265

Roach, M., Hanks, G., Thames, H., Schellhammer, P., Shipley, W. U., Sokol, G. H., & Sandler, H. (2006). Defining biochemical failure following radiotherapy with or without hormonal therapy in men with clinically localized prostate cancer: recommendations of the RTOG-ASTRO Phoenix Consensus Conference. *Int J Radiat Oncol Biol Phys*, *65*(4), 965-974. https://doi.org/10.1016/j.ijrobp.2006.04.029

Rosenkrantz, A. B., & Taneja, S. S. (2014). Radiologist, be aware: ten pitfalls that confound the interpretation of multiparametric prostate MRI. *AJR Am J Roentgenol*, *202*(1), 109-120. https://doi.org/10.2214/AJR.13.10699

Rouvière, O., Lyonnet, D., Raudrant, A., Colin-Pangaud, C., Chapelon, J. Y., Bouvier, R., Dubernard J. M., & Gelet, A. (2001). MRI appearance of prostate following transrectal HIFU ablation of localized cancer. *Eur Urol*, *40*(3), 265-274. https://doi.org/10.1159/000049786

Rouvière, O., Puech, P., Renard-Penna, R., Claudon, M., Roy, C., Mège-Lechevallier, F., Decaussin-Petrucci M., Dubreuil-Chambardel M., Magaud L., Remontet L., Ruffion A., Colombel M., Crouzet S., Schott A. M., Lemaitre L., Rabilloud M., & Grenier N. (2019). Use of prostate systematic and targeted biopsy on the basis of multiparametric MRI in biopsy-naive patients (MRI-FIRST): a prospective, multicentre, paired diagnostic study. *Lancet Oncol*, *20*(1), 100-109. https://doi.org/10.1016/S1470-2045(18)30569-2

Rouvière, O., Vitry, T., & Lyonnet, D. (2010). Imaging of prostate cancer local recurrences: why and how? *Eur Radiol*, *20*(5), 1254-1266. https://doi.org/10.1007/s00330-009-1647-4

Samei, E., & Peck, D. J. (2019). *Hendee's physics of medical imaging*. John Wiley & Sons.

Sapareto, S. A., & Dewey, W. C. (1984). Thermal dose determination in cancer therapy. *Int J Radiat Oncol Biol Phys*, *10*(6), 787-800. https://doi.org/10.1016/0360-3016(84)90379-1

Saylor, P. J., & Smith, M. R. (2013). Metabolic complications of androgen deprivation therapy for prostate cancer. *J Urol*, *189*(1 Suppl), S34-42; discussion S43-34. https://doi.org/10.1016/j.juro.2012.11.017

Scheltema, M. J., van den Bos, W., de Bruin, D. M., Wijkstra, H., Laguna, M. P., de Reijke, T. M., & de la Rosette, J. J. (2016). Focal vs extended ablation in localized prostate cancer with irreversible electroporation; a multi-center randomized controlled trial. *BMC Cancer*, *16*, 299. https://doi.org/10.1186/s12885-016-2332-z

Schenck, J. F. (1996). The role of magnetic susceptibility in magnetic resonance imaging: MRI magnetic compatibility of the first and second kinds. *Med Phys*, *23*(6), 815-850. https://doi.org/10.1118/1.597854

Sciacqua, L. V., Vanzulli, A., Di Meo, R., Pellegrino, G., Lavorato, R., Vitale, G., & Carrafiello, G. (2023). Minimally Invasive Treatment in Benign Prostatic Hyperplasia (BPH). *Technol Cancer Res Treat*, *22*, 15330338231155000. https://doi.org/10.1177/15330338231155000

Semple, J. E. (1963). Surgical capsule of the benign enlargement of the prostate. Its development and action. *Br Med J*, *1*(5346), 1640-1643. https://doi.org/10.1136/bmj.1.5346.1640

Shariat, S. F., Raptidis, G., Masatoschi, M., Bergamaschi, F., & Slawin, K. M. (2005). Pilot study of radiofrequency interstitial tumor ablation (RITA) for the treatment of radio-recurrent prostate cancer. *Prostate*, *65*(3), 260-267. https://doi.org/10.1002/pros.20242

Sheikhbahaei, S., Werner, R. A., Solnes, L. B., Pienta, K. J., Pomper, M. G., Gorin, M. A., & Rowe, S. P. (2019). Prostate-Specific Membrane Antigen (PSMA)-Targeted PET Imaging of Prostate Cancer: An Update on Important Pitfalls. *Semin Nucl Med*, *49*(4), 255-270. https://doi.org/10.1053/j.semnuclmed.2019.02.006

Shen, G., Deng, H., Hu, S., & Jia, Z. (2014). Comparison of choline-PET/CT, MRI, SPECT, and bone scintigraphy in the diagnosis of bone metastases in patients with prostate cancer: a meta-analysis. *Skeletal Radiol*, *43*(11), 1503-1513. https://doi.org/10.1007/s00256-014-1903-9

Siddiqui, K., Chopra, R., Vedula, S., Sugar, L., Haider, M., Boyes, A., Musquera M., Bronskill M., & Klotz, L. (2010). MRI-guided transurethral ultrasound therapy of the prostate gland using real-time thermal mapping: initial studies. *Urology*, *76*(6), 1506-1511. https://doi.org/10.1016/j.urology.2010.04.046

Siddiqui, K. M., Billia, M., Al-Zahrani, A., Williams, A., Goodman, C., Arifin, A., Violette P., Bauman G., & Chin, J. L. (2016). Long-Term Oncologic Outcomes of Salvage Cryoablation for Radio-Recurrent Prostate Cancer. *J Urol*, *196*(4), 1105-1111. https://doi.org/10.1016/j.juro.2016.04.080

Silver, D. A., Pellicer, I., Fair, W. R., Heston, W. D., & Cordon-Cardo, C. (1997). Prostate-specific membrane antigen expression in normal and malignant human tissues. *Clin Cancer Res*, *3*(1), 81-85.

Silvera, S., Oppenheim, C., Touzé, E., Ducreux, D., Page, P., Domigo, V., Mas J. L., Roux F. X., Frédy D., & Meder, J. F. (2005). Spontaneous intracerebral hematoma on diffusion-weighted images: influence of T2-shine-through and T2-blackout effects. *AJNR Am J Neuroradiol*, *26*(2), 236-241.

Stafford, R. J., Price, R. E., Diederich, C. J., Kangasniemi, M., Olsson, L. E., & Hazle, J. D. (2004). Interleaved echo-planar imaging for fast multiplanar magnetic resonance temperature imaging of ultrasound thermal ablation therapy. *J Magn Reson Imaging*, *20*(4), 706-714. https://doi.org/10.1002/jmri.20157

Stamey, T. A., Yang, N., Hay, A. R., McNeal, J. E., Freiha, F. S., & Redwine, E. (1987). Prostate-specific antigen as a serum marker for adenocarcinoma of the prostate. *N Engl J Med*, *317*(15), 909-916. https://doi.org/10.1056/NEJM198710083171501

Staruch, R. M., Nofiele, J., Walker, J., Bing, C., Madhuranthakam, A. J., Bailey, A., Kim Y. S., Chhabra A., Burns D., & Chopra, R. (2017). Assessment of acute thermal damage volumes in muscle using magnetization-prepared 3D T. *J Magn Reson Imaging*, *46*(2), 354-364. https://doi.org/10.1002/jmri.25605

Stone, H. B., Coleman, C. N., Anscher, M. S., & McBride, W. H. (2003). Effects of radiation on normal tissue: consequences and mechanisms. *Lancet Oncol*, *4*(9), 529-536. https://doi.org/10.1016/s1470-2045(03)01191-4

Su, S. L., Huang, I. P., Fair, W. R., Powell, C. T., & Heston, W. D. (1995). Alternatively spliced variants of prostate-specific membrane antigen RNA: ratio of expression as a potential measurement of progression. *Cancer Res*, *55*(7), 1441-1443.

Sundaram, K. M., Chang, S. S., Penson, D. F., & Arora, S. (2017). Therapeutic Ultrasound and Prostate Cancer. *Semin Intervent Radiol*, *34*(2), 187-200. https://doi.org/10.1055/s-0037-1602710

Sung, H., Ferlay, J., Siegel, R. L., Laversanne, M., Soerjomataram, I., Jemal, A., & Bray, F. (2021). Global Cancer Statistics 2020: GLOBOCAN Estimates of Incidence and Mortality Worldwide for 36 Cancers in 185 Countries. *CA Cancer J Clin*, *71*(3), 209-249. https://doi.org/10.3322/caac.21660

Suomi, V., Treeby, B., Jaros, J., Makela, P., Anttinen, M., Saunavaara, J., Sainio T., Kiviniemi A., & Blanco, R. (2018). Transurethral ultrasound therapy of the prostate in the presence of calcifications: A simulation study. *Med Phys*, *45*(11), 4793-4805. https://doi.org/10.1002/mp.13183

Swanson, G. P., & Hubbard, J. K. (2013). A better understanding of lymphatic drainage of the prostate with modern imaging and surgical techniques. *Clin Genitourin Cancer*, *11*(4), 431-440. https://doi.org/10.1016/j.clgc.2013.04.031

Sweat, S. D., Pacelli, A., Murphy, G. P., & Bostwick, D. G. (1998). Prostate-specific membrane antigen expression is greatest in prostate adenocarcinoma and lymph node metastases. *Urology*, *52*(4), 637-640. https://doi.org/10.1016/s0090-4295(98)00278-7

Taber, K. H., Herrick, R. C., Weathers, S. W., Kumar, A. J., Schomer, D. F., & Hayman, L. A. (1998). Pitfalls and artifacts encountered in clinical MR imaging of the spine. *Radiographics*, *18*(6), 1499-1521. https://doi.org/10.1148/radiographics.18.6.9821197

Tatebe, K., Ramsay, E., Mougenot, C., Kazem, M., Peikari, H., Bronskill, M., & Chopra, R. (2016). Influence of geometric and material properties on artifacts generated by interventional MRI devices: Relevance to PRF-shift thermometry. *Med Phys*, *43*(1), 241. https://doi.org/10.1118/1.4938099

Tay, K. J., Amin, M. B., Ghai, S., Jimenez, R. E., Kench, J. G., Klotz, L., Montironi R., Muto S., Rastinehad A. R., Turkbey B., Villers A., & Polascik, T. J. (2019). Surveillance after prostate focal therapy. *World J Urol*, *37*(3), 397-407. https://doi.org/10.1007/s00345-018-2363-y

Thomsen, F. B., Brasso, K., Klotz, L. H., Røder, M. A., Berg, K. D., & Iversen, P. (2014). Active surveillance for clinically localized prostate cancer--a systematic review. *J Surg Oncol*, *109*(8), 830-835. https://doi.org/10.1002/jso.23584

Tisseverasinghe, S. A., & Crook, J. M. (2018). The role of salvage brachytherapy for local relapse after external beam radiotherapy for prostate cancer. *Transl Androl Urol*, *7*(3), 414-435. https://doi.org/10.21037/tau.2018.05.09

Tosoian, J. J., Mamawala, M., Epstein, J. I., Landis, P., Wolf, S., Trock, B. J., & Carter, H. B. (2015). Intermediate and Longer-Term Outcomes From a Prospective Active-Surveillance Program for Favorable-Risk Prostate Cancer. *J Clin Oncol*, *33*(30), 3379-3385. https://doi.org/10.1200/JCO.2015.62.5764

Toussi, A., Stewart-Merrill, S. B., Boorjian, S. A., Psutka, S. P., Thompson, R. H., Frank, I., Tollefson M. K., Gettman M. T., Carlson R. E., Rangel L. J., & Karnes, R. J. (2016). Standardizing the Definition of Biochemical Recurrence after Radical Prostatectomy-What Prostate Specific Antigen Cut Point Best Predicts a Durable Increase and Subsequent Systemic Progression? *J Urol*, *195*(6), 1754-1759. https://doi.org/10.1016/j.juro.2015.12.075

Tran, H., Kwok, J., Pickles, T., Tyldesley, S., & Black, P. C. (2014). Underutilization of local salvage therapy after radiation therapy for prostate cancer. *Urol Oncol*, *32*(5), 701-706. https://doi.org/10.1016/j.urolonc.2013.12.014

Tsuzuki, T. (2015). Intraductal carcinoma of the prostate: a comprehensive and updated review. *Int J Urol*, *22*(2), 140-145. https://doi.org/10.1111/iju.12657

Turkbey, B., Rosenkrantz, A. B., Haider, M. A., Padhani, A. R., Villeirs, G., Macura, K. J., Tempany C. M., Choyke P. L., Cornud F., Margolis D. J., Thoeny H. C., Verma S., Barentsz J., & Weinreb, J. C. (2019). Prostate Imaging Reporting and Data System Version 2.1: 2019 Update of Prostate Imaging Reporting and Data System Version 2. *Eur Urol*, *76*(3), 340-351. https://doi.org/10.1016/j.eururo.2019.02.033

Uprimny, C., Kroiss, A. S., Decristoforo, C., Fritz, J., von Guggenberg, E., Kendler, D., Scarpa L., di Santo G., Roig L. G., Maffey-Steffan J., Horninger W., & Virgolini, I. J. (2017). Ga-PSMA-11 PET/CT in primary staging of prostate cancer: PSA and Gleason score predict the intensity of tracer accumulation in the primary tumour. *Eur J Nucl Med Mol Imaging*, *44*(6), 941-949. https://doi.org/10.1007/s00259-017-3631-6

Valerio, M., Cerantola, Y., Eggener, S. E., Lepor, H., Polascik, T. J., Villers, A., & Emberton, M. (2017). New and Established Technology in Focal Ablation of the Prostate: A Systematic Review. *Eur Urol*, *71*(1), 17-34. https://doi.org/10.1016/j.eururo.2016.08.044

Valle, L. F., Lehrer, E. J., Markovic, D., Elashoff, D., Levin-Epstein, R., Karnes, R. J., Reiter R. E., Rettig M., Calais J., Nickols N. G., Dess R. T., Spratt D. E., Steinberg M. L., Nguyen P. L., Davis B. J., Zaorsky N. G., & Kishan, A. U. (2021). A Systematic Review and Meta-analysis of Local Salvage Therapies After Radiotherapy for Prostate Cancer (MASTER). *Eur Urol*, *80*(3), 280-292. https://doi.org/10.1016/j.eururo.2020.11.010

Van den Broeck, T., van den Bergh, R. C. N., Arfi, N., Gross, T., Moris, L., Briers, E., Cumberbatch M., De Santis M., Tilki D., Fanti S., Fossati N., Gillessen S., Grummet J. P., Henry A. M., Lardas M., Liew M., Rouvière O., Pecanka J., Mason M. D., Schoots I. G., van Der Kwast T. H., van Der Poel H. G., Wiegel T., Willemse P. M., Yuan Y., Lam T. B., Cornford P., & Mottet, N. (2019). Prognostic Value of Biochemical Recurrence Following Treatment with Curative Intent for Prostate Cancer: A Systematic Review. *Eur Urol*, *75*(6), 967-987. https://doi.org/10.1016/j.eururo.2018.10.011

van der Leest, M., Cornel, E., Israël, B., Hendriks, R., Padhani, A. R., Hoogenboom, M., Zamecnik P., Bakker D., Setiasti A. Y., Veltman J., van den Hout H., van der Lelij H., van Oort I., Klaver S., Debruyne F., Sedelaar M., Hannink G., Rovers M., Hulsbergen-van de Kaa C., & Barentsz, J. O. (2019). Head-to-head Comparison of Transrectal Ultrasound-guided Prostate Biopsy Versus Multiparametric Prostate Resonance Imaging with Subsequent Magnetic Resonance-guided Biopsy in Biopsy-naïve Men with Elevated Prostate-specific Antigen: A Large Prospective Multicenter Clinical Study. *Eur Urol*, *75*(4), 570-578. https://doi.org/10.1016/j.eururo.2018.11.023

van Leenders, G. J. L. H., van der Kwast, T. H., Grignon, D. J., Evans, A. J., Kristiansen, G., Kweldam, C. F., Litjens G., McKenney J. K., Melamed J., Mottet N., Paner G. P., Samaratunga H., Schoots I. G., Simko J. P., Tsuzuki T., Varma M., Warren A. Y., Wheeler T. M., Williamson S. R., & Iczkowski K. A. (2020). The 2019 International Society of Urological Pathology (ISUP) Consensus Conference on Grading of Prostatic Carcinoma. *Am J Surg Pathol*, *44*(8), e87-e99. https://doi.org/10.1097/PAS.0000000000001497

Van Nieuwenhove, S., Van Damme, J., Padhani, A. R., Vandecaveye, V., Tombal, B., Wuts, J., Pasoglou V., & Lecouvet, F. E. (2022). Whole-body magnetic resonance imaging for prostate cancer assessment: Current status and future directions. *J Magn Reson Imaging*, *55*(3), 653-680. https://doi.org/10.1002/jmri.27485

Venkatesan, A. M., Partanen, A., Pulanic, T. K., Dreher, M. R., Fischer, J., Zurawin, R. K., Muthupillai R., Sokka S., Nieminen H. J., Sinaii N., Merino M., Wood B. J., & Stratton, P. (2012). Magnetic resonance imaging-guided volumetric ablation of symptomatic leiomyomata: correlation of imaging with histology. *J Vasc Interv Radiol*, *23*(6), 786-794.e784. https://doi.org/10.1016/j.jvir.2012.02.015

Viitala, A., Anttinen, M., Wright, C., Virtanen, I., Mäkelä, P., Hovinen, T., Sainio T., Saunavaara J., Taimen P., Blanco Sequeiros R., & Boström, P. J. (2022). Magnetic resonance imaging-guided transurethral ultrasound ablation for benign prostatic hyperplasia: 12-month clinical outcomes of a phase I study. *BJU Int*, *129*(2), 208-216. https://doi.org/10.1111/bju.15523

Walsh, P. C., & Mostwin, J. L. (1984). Radical prostatectomy and cystoprostatectomy with preservation of potency. Results using a new nerve-sparing technique. *Br J Urol*, *56*(6), 694-697. https://doi.org/10.1111/j.1464-410x.1984.tb06149.x

Watts, K. L., Frechette, L., Muller, B., Ilinksy, D., Kovac, E., Sankin, A., & Aboumohamed, A. (2020). Systematic review and meta-analysis comparing cognitive vs. image-guided fusion prostate biopsy for the detection of prostate cancer. *Urol Oncol*, *38*(9), 734.e719-734.e725. https://doi.org/10.1016/j.urolonc.2020.03.020

Weidensteiner, C., Quesson, B., Caire-Gana, B., Kerioui, N., Rullier, A., Trillaud, H., & Moonen, C. T. (2003). Real-time MR temperature mapping of rabbit liver in vivo during thermal ablation. *Magn Reson Med*, *50*(2), 322-330. https://doi.org/10.1002/mrm.10521

Weishaupt, D., Köchli, V. D., Marincek, B., Froehlich, J. M., Nanz, D., & Pruessmann, K. P. (2006). *How does MRI work?: an introduction to the physics and function of magnetic resonance imaging* (Vol. 2). Springer.

White, S., Hricak, H., Forstner, R., Kurhanewicz, J., Vigneron, D. B., Zaloudek, C. J., Weiss J. M., Narayan P., & Carroll, P. R. (1995). Prostate cancer: effect of postbiopsy hemorrhage on interpretation of MR images. *Radiology*, *195*(2), 385-390. https://doi.org/10.1148/radiology.195.2.7724756

Wilt, T. J., Vo, T. N., Langsetmo, L., Dahm, P., Wheeler, T., Aronson, W. J., Cooperberg M. R., Taylor B. C., & Brawer, M. K. (2020). Radical Prostatectomy or Observation for Clinically Localized Prostate Cancer: Extended Follow-up of the Prostate Cancer Intervention Versus Observation Trial (PIVOT). *Eur Urol*, *77*(6), 713-724. https://doi.org/10.1016/j.eururo.2020.02.009

Wise, A. M., Stamey, T. A., McNeal, J. E., & Clayton, J. L. (2002). Morphologic and clinical significance of multifocal prostate cancers in radical prostatectomy specimens. *Urology*, *60*(2), 264-269. https://doi.org/10.1016/s0090-4295(02)01728-4

Wright, C., Mäkelä, P., Anttinen, M., Sainio, T., Boström, P. J., & Blanco Sequeiros, R. (2021). Fiducial markers and their impact on ablation outcome for patients treated with MR-guided transurethral ablation (TULSA): a retrospective technical analysis. *Int J Hyperthermia*, *38*(1), 1677-1684. https://doi.org/10.1080/02656736.2021.2008519

Zhou, Y. F. (2011). High intensity focused ultrasound in clinical tumor ablation. *World J Clin Oncol*, *2*(1), 8-27. https://doi.org/10.5306/wjco.v2.i1.8

TURUN
YLIOPISTO
UNIVERSITY
OF TURKU

Painosalama, Turku, Finland 2024

ISBN 978-951-29-9861-6 (PRINT)
ISBN 978-951-29-9862-3 (PDF)
ISSN 0355-9483 (Print)
ISSN 2343-3213 (Online)